Transient Photophysics of Bismuth Halide Semiconductors for Optoelectronic Applications

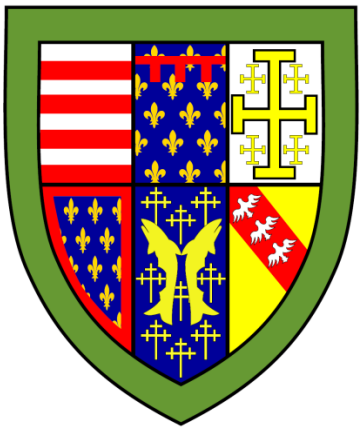

Lissa F. L. Eyre

Department of Engineering

University of Cambridge

A dissertation submitted for the degree of

Doctor of Philosophy

Queens' College

July 2020

To Vania, John, Daniel and Fuchsia

Declaration

I hereby declare that except where specific reference is made to the work of others, the contents of this dissertation are original and have not been submitted in whole or in part for consideration for any other degree or qualification in this, or any other university. This dissertation is my own work and contains nothing which is the outcome of work done in collaboration with others, except as specified in the text and Acknowledgements. This dissertation contains fewer than 65,000 words including appendices, bibliography, footnotes, tables and equations and has fewer than 150 figures.

Lissa Eyre

July 2020

Transient Photophysics of Bismuth Halide Semiconductors for Optoelectronic Applications

Lissa Eyre

This thesis describes a series of spectroscopic studies of three different semiconductors based on bismuth halides in order to discover their fundamental photophysical properties. The materials investigated — the double perovskite $Cs_2AgBiBr_6$, bismuth iodide, and bismuth oxyiodide — have all been demonstrated in thin film photovoltaic devices fabricated at low temperatures. Propelled by the success of lead halide perovskites, this work forms part of the search for defect tolerant, non-toxic and stable materials for next-generation solar cells.

I use transient absorption spectroscopy to show that the charge carrier lifetime in $Cs_2AgBiBr_6$ thin films is 1.4 μs. This is significantly longer than previous estimates based on time-resolved photoluminescence measurements, which measure the radiatively decaying carriers, but is a less sensitive probe of the high proportion of carriers which recombine non-radiatively. I propose a radiative recombination mechanism *via* defects, based on the detection of mid-gap electronic states in the transient absorption spectra. Coherent phonon transients are also measured on ultrafast timescales showing strong electron-phonon coupling in the material, which may contribute to the slow recombination in this material.

The recombination dynamics of excitons in the layered material bismuth iodide, BiI_3, are investigated using temperature dependent photoluminescence and transient absorption. I show that coupling to interlayer and intralayer phonon modes strongly affects the direct exciton decay pathway through scattering and modulation of the band gap energy. In a single crystal of BiI_3, the room temperature exciton lifetime is 72 ns, which indicates this material's potential for photovoltaics if the defects in thin films can be passivated.

I show that the excited states of thin films of layered bismuth oxyiodide, BiOI, have a great degree of energetic disorder, most likely due to the presence of self-trapped excitons and defect states. Transient absorption measurements give an excited state lifetime of 47 ps, which would make efficient photovoltaic performance of BiOI thin film absorbers very unlikely.

On the basis of my findings, all three materials show strong coupling between phonons and electronic states, but have excited state lifetimes varying over many orders of magnitude. This should guide the direction of future research towards different applications: the most promising candidate for photovoltaic applications is therefore $Cs_2AgBiBr_6$, whereas BiI_3 and BiOI have more potential for use in nanostructured devices, such as ultrathin photodetectors, which can exploit their anisotropic nature.

Acknowledgements

I am grateful and humbled to have received the help and support of so many people during the years building up to this body of work. I have had two excellent supervisors who have guided, encouraged and supported me in all aspects of my PhD — Dr Hannah Joyce and Dr Felix Deschler. I thank them for the opportunity to undertake this exciting research and to be part of both groups which they lead thoughtfully and enthusiastically. Many thanks are also due to Dr Robert Hoye for his generous input of ideas, materials and many discussions, without which this work would not be possible. I am also grateful to my collaborators Dr Tomeu Montserrat and Professor Richard Phillips and the work of their students, attributed throughout the text, for many helpful measurements and calculations.

The Optoelectronics group has at times been like an extended family – they don't always get along but someone is always there when you need help. From the beginning I received invaluable support and training from Greg, Sarwat, Johannes, Jasmine and Alex G. I am lucky to have had a great cohort in Heather, Hope, Raj, Pete and many others who helped to bridge the gaps between lofty PIs and various corners of the Cavendish. The death of the fastlab meeting was truly a tragic loss.

I was fortunate enough to undertake a research visit in the former group of Professor Jim Schuck at the Lawrence Berkeley National Laboratory and, under the supervision of Dr Nick Boris, learned a great wealth of lab skills. This was possible thanks to funding from the Winton-Kavli Exchange scheme.

In the newer members of the Deschler group, I have found a worthy bunch of lab companions, idea debaters and travel mates. So thank you all for making it an absolute blast, Prosecco Princess, DJ Timmy Trumpet, LCP Doggo Sean, OG Unicorn, Mr Tartallini, Cherub Timo and Cap'n Thomas. Never stop writing poetry, working out and drinking away taxpayers' money.

Another Cavendish VIP I would like to thank is Claire Malone: a keen high energy physicist, friend and supporter, all through having me on as a scribe. Working with you has been an honour and I enjoyed all the top (quark) banter.

I must thank the NanoDTC, not only for my funding and a very enriching Masters year, but also for a group of firm friends. Thank you to all my cohort, especially Ewan and Josh, who spared me their tables and sofas for writing, and most of all Lauren, without whose sisterhood and constant support, this just would not have got done.

While writing far from home in the midst of the COVID-19 pandemic, I was incredibly blessed that Philipp, Doreen and Hendrik Köhler gave me a safe refuge in their home. I thank them for showing me the very definition of generous hospitality.

Thanks also to my smart, funny, gorgeous STAGS girls for keeping me sane and making me feel loved no matter the time or place. To Georgia and Michael, my best friends, I owe so many thanks for bearing the brunt of my insecurities, giving me innumerable hugs, making sure I was fed, watered and walked (danced), and also for making life fun for five years.

My family have always been my firm foundation, enabling and encouraging me to give my very best, while showing me by their quiet example how to live with integrity, compassion and determination.

I am most grateful, though, to my God and eternal Teacher, who has concealed a matter and allowed me a chance to search it out.

"It is the glory of God to conceal a matter; to search out a matter is the glory of kings."
Proverbs 25:2

Contents

List of Figures

Acronyms, Symbols and Abbreviations

BiI_3	bismuth (III) iodide
BiOI	bismuth oxyiodide
c	speed of light in a vacuum
CBM	conduction band maximum
CCD	charge coupled device
$Cs_2AgBiBr_6$	caesium silver bismuth bromide
CW	continuous wave
DFT	density functional theory
DOS	density of states
EQE	external quantum efficiency
FFT	fast Fourier transform
FT	Fourier transform
FWHM	full width half maximum
GaAs	gallium arsenide
GSB	ground state bleach
iCCD	intensified charge coupled device
InGaAs	indium gallium arsenide
JDOS	joint density of states
λ	wavelength
ν	frequency
PCE	power conversion efficiency
PDS	photothermal deflection spectroscopy
PIA	photoinduced absorption
PL	photoluminesence
PLQE	photoluminescence quantum efficiency
Ref	reference
SEM	scanning electron microscopy
Si	silicon

TA	transient absorption
TR	transient reflection
TCSPC	time correlated single photon counting
UV	ultra-violet
VBM	valence band minimum

Relevant Publications

Robert L. Z. Hoye, **Lissa Eyre**, Fengxia Wei, Federico Brivio, Aditya Sadhanala, Shijing Sun, Weiwei Li, Kelvin H. L. Zhang, Judith L. MacManus-Driscoll, Paul D. Bristowe, Richard H. Friend, Anthony K. Cheetham, Felix Deschler, "Fundamental Carrier Lifetime Exceeding 1 µs in $Cs_2AgBiBr_6$ Double Perovskite," *Adv. Mater. Interfaces*, vol. 5, no. 15, 2018, doi: 10.1002/admi.201800464.

Tahmida N. Huq, Lana C. Lee, **Lissa Eyre**, Weiwei Li, Robert A. Jagt, Chaewon Kim, Sarah Fearn, Vincenzo Pecunia, Felix Deschler, Judith L. MacManus-Driscoll, Robert L. Z. Hoye, "Electronic Structure and Optoelectronic Properties of Bismuth Oxyiodide Robust against Percent-Level Iodine-, Oxygen-, and Bismuth-Related Surface Defects," *Adv. Funct. Mater.*, vol. 30, no. 13, p. 1909983, Mar. 2020, doi: 10.1002/adfm.201909983.

Chapter 1: Introduction

Modern society depends on electricity. In the last ten years alone the proportion of people worldwide with access to electricity has risen from 79.9% to 88.7% [1]. Meanwhile, the human population continues to grow and is projected to reach 9.7 billion in 2050 [2]. Most of this energy has been generated by using up limited stores of fossil fuels, and in the process rapidly increasing the carbon dioxide content of the atmosphere. If we are to meet future energy demand without heating the planet to more than 1.5°C above pre-industrial temperatures, we will need to generate large amounts of energy without emitting carbon dioxide in the process – by switching away from fossil fuels to renewable sources of energy [3].

Fortunately for us, the sun's rays contain a vast amount of energy, which we can convert into electricity using photovoltaic cells. In the years from 2014 to 2018, solar photovoltaics contributed to nearly a third of growth in global renewable electricity generation [1]. This has largely been driven by the falling cost of polycrystalline silicon solar cells as well as technological advances increasing their efficiency [4].

Despite the advantages of using silicon for solar cells – it is abundant, durable, and now also cheap – its indirect bandgap and weak optical absorption make a thick layer necessary for the device to be efficient. This weight and inflexibility of thick crystalline silicon increases the installation cost of a module and make it less practical for portable applications [5]. Silicon also requires high processing temperatures (about 1100°C), which adds to the energy cost associated with manufacturing each module [6]. Alternative materials which enable thinner, lighter solar cells and which can be processed at low temperatures may help to broaden the uptake of solar energy and lower its costs.

Such materials so far investigated come under the categories of semiconductor nanocrystals, organic semiconductors, and solution-processable inorganic semiconductors. The latter have come to the forefront in the last decade due to the unprecedented rise in power conversion efficiency of lead halide perovskite solar cells. Lead halide perovskite thin films can be

fabricated by printing or spin coating and prototype devices have now surpassed polycrystalline silicon in efficiency [7]; however, they degrade on contact with moisture and oxygen and contain lead in a soluble form, which increases its toxicity [8]. A search has begun for effective and cheap inorganic light absorbers, without the lead.

Theoretical and experimental studies have shown that bismuth halide-based semiconductors may share some of the advantages of lead halide perovskites, such as strong optical absorption and tolerance to defects produced during their 'messy' fabrication [9]. However, initial device efficiencies have been low. With many different compositions and structures to study, it can be difficult to know which to further optimise. This is where an understanding of the fundamental photophysics of these materials is important. Measuring the behaviour of photoexcited states, i.e. how they interact with each other, the surrounding material and light, allows us to judge whether the material can be efficient in the future, and what currently limits its performance.

In this thesis I describe my investigation of the photophysical properties of three different bismuth halide based semiconductors, which each have been demonstrated in experimental solar cells, using transient spectroscopy to evaluate their potential to be efficient.

Chapter 2 introduces the theoretical concepts needed to understand the work and assesses previous work in the field of lead-free perovskite research, which directed my study. In Chapter 3, the methods I used to perform my experiments are presented. This is followed by chapters containing the results of my experiments, organised by material. Chapter 4 focuses on the silver-bismuth double perovskite, $Cs_2AgBiBr_6$. Using transient absorption I show that photoexcited charge carriers in polycrystalline films persist almost an order of magnitude longer than has been measured previously by transient photoluminescence. At 1.4 μs, it is the longest charge carrier lifetime of all the materials I present in this thesis, which makes it the most promising to support efficient charge extraction in solar cells. I also provide evidence for defect-mediated radiative recombination and strong electron–phonon coupling which underlie the slow rate of recombination. In Chapter 5, I explore the photophysical properties of bismuth iodide, BiI_3. Here I establish the effect of different phonon modes on the radiative recombination of excitons in a single crystal. I show that their overall lifetime is 72 ns which sets a fundamental limit on the efficiency of BiI_3 absorber layers. Chapter 6 presents work on a related compound, bismuth oxyiodide, BiOI, in which I find a large degree of energetic disorder in polycrystalline thin films. The lifetime of charge carriers is 47 ps, the least

promising value. I also explore the electron-phonon coupling in more depth as well as presenting a comparison of this feature in all the materials at the end of the chapter. It was universally found that the phonon modes associated with a bismuth–halide bond stretch have the biggest influence on electronic states. Finally, I summarise all the conclusions and suggest avenues for further research in Chapter 7.

Before attempting to direct the path of future research in the field of lead-free semiconductors for photovoltaics, it is important to review the road already travelled, therefore I will now summarise the work that guided me to mine.

Chapter 2: Theoretical background

This chapter starts with the theoretical basis of my work - the physics of semiconductors, their optoelectronic properties, and their function in photovoltaic devices. I analyse previous research in the field of lead-free, solution-processed semiconductors for solar cells and present the motivation for my research.

2.1 Semiconductor photophysics

There are various useful features of semiconductors which have led to their widespread application in electronics and optoelectronics. Here, I focus on optoelectronic applications and therefore the interaction of semiconductors with light.

2.1.1 Electronic structure

2.1.1.1 Band theory

Quantum mechanics is required to understand the behaviour of electrons and nuclei in all crystalline solids, including semiconductors. The Schrödinger equation must be solved for a periodic arrangement of atoms in an inorganic semiconductor. In order to simplify this many-body problem, we make the assumptions that: core electrons are inseparable from the nuclei, so that only valence electrons and ions may be considered; and that ions move much slower than electrons, due to their larger masses (the Born-Oppenheimer approximation). The Hamiltonian used to describe the energies and interactions of the ions and valence electrons is as follows [10],

$$H = H_{\text{ions}}(\boldsymbol{R}_j) + H_{\text{e}}(\boldsymbol{r}_i, \boldsymbol{R}_{j0}) + H_{\text{e-ion}}(\boldsymbol{r}_i, \delta\boldsymbol{R}_j)\,. \qquad (1)$$

$H_{\text{ions}}(\boldsymbol{R}_j)$ is the Hamiltonian for the ionic kinetic and potential energy, which includes the potential due to time-averaged electronic positions and depends on the spatial coodinates, $\boldsymbol{R}_j$, of each ion, j. $H_{\text{e}}(\boldsymbol{r}_i, \boldsymbol{R}_{j0})$ is the Hamiltonian of the electronic kinetic energy with the ions

fixed at their equilibrium positions, $\boldsymbol{R}_{j0}$, and the electrons, i, at coordinates $\boldsymbol{r}_i$. $H_{\text{e-ion}}(\boldsymbol{r}_i, \delta\boldsymbol{R}_j)$ is the Hamiltonian for the change of energy of the electrons due to ionic displacements of $\delta\boldsymbol{R}_j$ from rest at $\boldsymbol{R}_{j0}$, i.e. the electron–phonon interaction.

The electronic Hamiltonian, $H_{\text{e}}(\boldsymbol{r}_i, \boldsymbol{R}_{j0})$, can be expressed in terms of a periodic potential, $V(\boldsymbol{r})$, which all the electrons experience identically in a mean-field approximation. The energies for a single electron can now be found by solving the equation,

$$\left(\frac{\boldsymbol{p}^2}{2m} + V(\boldsymbol{r})\right)\phi_n(\boldsymbol{r}) = E_n\phi_n(\boldsymbol{r})\,, \tag{2}$$

where $\boldsymbol{p}$ is the momentum operator, m is the mass of an electron, $\phi_n(\boldsymbol{r})$ is the electronic wavefunction and E_n is the energy of an electron in eigenstate n. As $V(\boldsymbol{r})$ is periodic, Bloch's theorem states that the electronic wavefunctions must be plane waves with the form [11],

$$\phi_k(\boldsymbol{r}) = u_k(\boldsymbol{r})e^{i\boldsymbol{k}\cdot\boldsymbol{r}}\,, \tag{3}$$

where $u_k(\boldsymbol{r})$ is a function with the periodicity of the lattice. The wavevector, $\boldsymbol{k}$, of the plane waves then defines the energy of an electron in that state, E_k. In the electronic band structure, E_k is plotted against the magnitude of the wavevector, k. As both k and $k + (2n\pi/a)$ can be represented by a single $\phi_k(\boldsymbol{r})$, where n is any integer and a is the periodicity of the lattice, the plot is usually restricted to the range between $k = \pm\pi/a$, known as the first Brillouin zone.

The origin of a band gap may be intuitively explained by the different energies of wavefunctions at the Brillouin zone boundary, which are effectively standing waves. This produces alternating regions of high and low electron density. When the high electron density coincides with the positive ion cores, the Coulomb energy will be lowered, and when the electron density lies between ions, the Coulomb energy is maximised. Therefore, these two states with the same wavevector have different potential energies. Due to the quantisation of k-states, there is no intermediate state, therefore a gap devoid of states exists between these two energies — a band gap.

The band structure of a material can be calculated using the symmetry properties of its crystal structure to determine the form of $V(\boldsymbol{r})$ and solve for the energy levels [10]. For inorganic materials, the most common approaches are density functional theory (DFT), or pseudopotential methods. In a semiconductor, at absolute zero temperature, the valence

electrons completely fill the valence band, which is separated from the higher energy conduction band by the band gap energy. Thermal and electromagnetic energy can excite electrons from the top of the valence band into the conduction band. The resulting absence of an electron in the valence band can be thought of as a positively charged quasiparticle, referred to as a 'hole'. It is the flow of electrons and holes which produce current, and therefore they are both labelled as charge carriers.

2.1.1.2 Parabolic band approximation

For semiconductors used in photovoltaics, the electrons and holes near the bandgap dominate the optoelectronic properties of the material, so we can take a Taylor expansion of the dispersion relation, $E(\boldsymbol{k})$, around the conduction band minimum (CBM) or valence band maximum (VBM), occurring at $\boldsymbol{k}_0$. To first order,

$$E(\boldsymbol{k}) = E(\boldsymbol{k}_0) \pm \frac{\hbar^2 |\boldsymbol{k} - \boldsymbol{k}_0|^2}{2m^*}, \tag{4}$$

where the positively curved band is the conduction band and the negatively curved, the valence band. The effective mass, m^*, is defined as,

$$\frac{1}{m^*} = \pm \frac{1}{\hbar} \frac{\partial^2 E}{\partial k^2}. \tag{5}$$

This is then the (always positive) effective mass of electrons near the CBM and holes near the VBM. It describes how they respond to forces applied externally or when interacting with other charge carriers. The effective mass affects charge carrier mobility, optical absorption cross section and carrier recombination rate. Depending on the symmetry of the crystal, the dispersion may be different along different directions, in which case, the effective mass is a tensor.

2.1.1.3 Defect and impurity states

So far we have only considered the ideal case of a perfect crystal without surfaces, defects or impurities. Real semiconductors will have all of these, in varying amounts, dependent on material processing. In some cases, impurities are added deliberately to dope the semiconductor. For example, a phosphorus (group V) impurity in silicon (group IV) has one more valence electron than the surrounding atoms, so once the bonding to nearest neighbours has been fulfilled, one electron remains free [10]. This can either occupy the conduction

band, leaving behind a positively charged phosphorus ion, or it can orbit the ion in a bound state similar to a hydrogen atom but modified by the permittivity of the medium and the effective mass [12]. The binding energy of this state dictates whether the impurity will be ionised at room temperature. Phosphorus in silicon is an example of n-type doping because this leads to a majority of free electrons, whereas group III impurities such as boron and aluminium provide p-type doping, leading to an excess of holes. Undoped semiconductors with an equal number of electrons and holes are labelled 'intrinsic'.

In the absence of impurities, the material is still terminated by surfaces and may contain point defects. Surfaces can create states in the middle of the band by their nature as 'dangling bonds' or through interaction with external species such as through adsorption of gases. Point defects can be either a vacancy, an interstitial, or an antisite defect. These are denoted V_A for a vacant site of species A, I_A for an interstitial atom of species A, or A_B for an instance of species B occupying a lattice site of species A.

The formation enthalpy of a certain defect determines its concentration in a sample, depending on the fabrication temperature. Formation enthalpies can be theoretically predicted using DFT supercell calculations [13],[14]. Considering the different possible charge states of a defect allows the thermal ionisation energy and the energy of optical transitions involving the defect state to be calculated [13].

The consequences of the band gap and defect states for optical properties and devices will be discussed further in Section 2.1.2.

2.1.1.4 Density of states

The density of states (DOS) available at each energy can be straightforwardly predicted using the band structure calculated by DFT. Under the parabolic band approximation, the DOS, $\rho(E)$, near the band edge can be estimated as follows [15]:

$$\rho(E) = \frac{2\rho(k)}{dE/dk}\ , \tag{6}$$

where $\rho(k)$ is the density of states in reciprocal space, and each state may hold two electrons of opposite spins due to the Pauli exclusion principle. The density of states in reciprocal space is found by applying periodic boundary conditions to a cubic volume of the material to

find the spacing between k-states and considering surfaces of equal k in three dimensional k-space. Using dE/dk from the parabolic band approximation, the DOS becomes,

$$\rho(E) = \frac{1}{2\pi^2}\left(\frac{2m^*}{\hbar^2}\right)^{\frac{3}{2}} E^{\frac{1}{2}} \ . \tag{7}$$

2.1.1.5 Band occupation

In order to understand how photogenerated carriers behave when excited into the bands, it is important to understand the equilibrium conditions of band occupation. Electrons are fermions and therefore obey Fermi-Dirac statistics in thermal equilibrium. This means the likelihood of an electron occupying a state with energy, E, is [16],

$$f(E) = \frac{1}{e^{(E-E_f)/k_BT} + 1} \ . \tag{8}$$

where E_f is the Fermi energy, defined as the statistical potential energy of the electrons. For an intrinsic semiconductor, the Fermi energy lies in the middle of the band gap. If the band gap is wide compared to the thermal energy, the occupation of electrons in the conduction band can be approximated with a Boltzmann distribution,

$$f(E) \approx e^{(E_f-E)/k_BT} \ . \tag{9}$$

This distribution also applies for holes in the valance band. Combining this with the density of states for parabolic bands gives an intrinsic carrier density, n_i, where,

$$n_i^2 = np = N_c N_v e^{-E_g/k_BT} \ , \tag{10}$$

with,

$$N_{c,v} = 2\left(\frac{m_{c,v}^* k_B T}{2\pi\hbar^2}\right)^{3/2} \ . \tag{11}$$

When a higher number of charge carriers populate the bands than in thermal equilibrium, either through photoexcitation or injection from an external circuit, they will populate states according to a quasi-equilibrium Fermi-Dirac distribution, with a modified value of E_f for the electrons and holes, called ‘quasi-Fermi levels’ [16]. In transient absorption spectroscopy, the photoexcited electron and hole populations can be detected due to a reduction in optical absorption near the band edge.

In highly non-equilibrium situations, the Burstein-Moss effect may occur, for example, when the material is 'degenerately doped' or has a high injected charge carrier density, such that the one or both quasi-Fermi levels lies inside the bands. The Pauli exclusion principle forces any additional carriers to occupy higher lying states, giving the appearance of an increased band gap energy [17]. This can be observed in spectroscopic experiments involving high photoexcitation densities [18].

2.1.2 Interband transitions

The interaction of light with semiconductors can be modelled as a classical oscillating electric field acting on many bound dipoles, known as the Lorentz model [15]. While this can describe most observations of the effect of light on semiconducting solids, quantum mechanics provides a fuller picture on the energy scale close to the band gap. Using time-dependent perturbation theory, Fermi's golden rule states that the transition from an initial state $|\psi_i\rangle$ to a final state $|\psi_f\rangle$ under a perturbing interaction Hamiltonian H' occurs at a rate,

$$\Gamma_{i\to f} = \frac{2\pi}{\hbar}\left|\langle\psi_f|H'|\psi_i\rangle\right|^2 \rho_f(E)\,, \tag{12}$$

where $\rho_f(E)$ is the density of final states and $\langle\psi_f|H'|\psi_i\rangle = M_{i\to f}$ is the matrix element of the perturbing Hamiltonian. For a Hamiltonian which is oscillating at angular frequency, ω, and which interacts adiabatically with a simple two-level system, the transition rate can be described as,

$$\Gamma_{i\to f} \propto \left|M_{i\to f}\right|^2\left[\delta\left(E_f - E_i + \hbar\omega\right) + \delta\left(E_f - E_i - \hbar\omega\right)\right]\,. \tag{13}$$

Neglecting rapidly oscillating terms due to the adiabatic constraint, this means that only transitions between levels with an energy gap equal to the energy of the photon ($\hbar\omega$) are allowed. A transition from a lower to a higher energy state is absorption of the photon ($+\hbar\omega$) and from the higher to the lower energy state is stimulated emission ($-\hbar\omega$). Spontaneous emission will be discussed later.

The matrix element contains information about the spatial overlap and symmetry properties of the initial and final wavefunctions. Similar to the classical case, the perturbation is described as an electric dipole interaction, using a Hamiltonian of the form,

$$H' = -\boldsymbol{p}_e \cdot \boldsymbol{\epsilon}_{\text{photon}}\,, \tag{14}$$

where $\boldsymbol{p}_e$ is the electron dipole moment operator and $\boldsymbol{\epsilon}_{\text{photon}}$ is the oscillating electric field of the photon. The electric dipole moment between band edge states is a property of the system, which varies between different materials.

In addition, the transition must conserve momentum [10]. As photons carry very little momentum, compared to the typical range of momenta of electrons in the Brillouin zone, any purely optical transitions between the valence band and the conduction band will be represented as vertical on a dispersion curve ($\Delta k = \omega/c << \pi/a$). Any transition between states having different momenta must therefore involve the absorption or emission of at least one phonon (quantised lattice vibration) as well as a photon. Phonons have large momenta compared to their energies and are represented as shallow lines on the electronic band structure ($\Delta k/\omega = 1/v_{\text{sound}} \gg 1/c$). This will be treated formally in the next section.

When considering optical absorption transitions in different semiconductors, one must also include the density of states. Due to the different combinations of states in the valence, $E_V(\boldsymbol{k})$, and conduction band, $E_C(\boldsymbol{k})$, which may be involved in momentum-conserving optical transitions, the joint density of states (JDOS) is more useful than the DOS, defined as,

$$\rho_{CV}(E) = \frac{2}{(2\pi)^3}\int_{S:E_{CV}=\hbar\omega} \frac{dS}{\left|\nabla_k\left(E_C(\boldsymbol{k}) - E_V(\boldsymbol{k})\right)\right|} \ . \tag{15}$$

This dominates the energy dependence of optical absorption in the material, which is enhanced at energies where the valence and conduction band are parallel to each other, i.e. when $\nabla_k E_C = \nabla_k E_V$. In a direct semiconductor the bands are parallel at the band edge, therefore the JDOS is high at the bandgap energy. Under the parabolic band approximation, it can be shown that the absorption, α, of photons with energies above the bandgap, E_g, has the following dependence,

$$\alpha(E) \propto \left(E - E_g\right)^{\frac{1}{2}} \ . \tag{16}$$

This will not be true for indirect bandgaps, higher energies where the bands are not parabolic, or if there are impurity states close to the band edges.

2.1.2.1 Indirect band edge transitions

In direct bandgap semiconductors, the CBM and VBM occur at the same value of k, however, in indirect semiconductors they lie at different values of k. An example of a direct

bandgap semiconductor is gallium arsenide, GaAs. A common indirect semiconductor is silicon. The absorption of a photon by an indirect bandgap semiconductor from the VBM to the CBM, via emission or absorption of a phonon, is therefore a higher order process than the direct transition, and is typically much weaker.

When the absorption or emission of phonons is required for optical absorption at the band edge, Fermi's golden rule can be extended to include transitions via a virtual state, using second order perturbation theory [10]. The more phonons involved, the lower the probability of the transition. Considering a transition involving one photon of energy $\hbar\omega$ and one phonon of energy E_p, the rate of transition is,

$$\Gamma_{ind} = \frac{2\pi}{\hbar} \sum_{k_C,k_V} \left| \sum_i \frac{\langle f|H_{ep}|i\rangle\langle i|H_{eR}|0\rangle}{E_{i0} - \hbar\omega} \right|^2 \delta\left(E_C(\boldsymbol{k}_C) - E_V(\boldsymbol{k}_V) - \hbar\omega \pm E_p\right), \quad (17)$$

where $|0\rangle$ is the ground state of the system (full valence band and empty conduction band), $|i\rangle$ is the intermediate state and $|f\rangle$ is the final excited state with an electron in the conduction band and a hole in the valence band. H_{ep} is the electron–phonon interaction Hamiltonian and H_{eR} is the electron–photon interaction Hamiltonian. Assuming constant matrix elements close to the band extrema and that the bands are parabolic and three dimensional, the densities of states of the valence and conduction band dominate the energy dependence of the transition rate. Integrating over all the possible energy-conserving combinations, the energy dependence of the absorption becomes,

$$\alpha(E) \propto \left(E - \left(E_g \pm E_p\right)\right)^2, \quad (18)$$

for photon energies above $E_g - E_p$. Two absorption edges may therefore be detected for each phonon that can contribute to indirect absorption.

The population of these phonons present in the material influences the matrix element $\left|\langle f|H_{ep}|i\rangle\right|^2$ for both absorption and emission of a phonon. The absorption of a phonon requires a population of the phonon to be present in the material ($\alpha \propto N_p$), so the $E_g - E_p$ absorption edge only appears at high temperatures, when the phonons are thermally excited. On the other hand, the process involving the emission of a phonon can happen at any temperature ($\alpha \propto (1 + N_p)$).

At room temperature, indirect transitions are usually orders of magnitude weaker than direct ones [15], which, in photovoltaics, translates to the use of thicker absorbing layers of indirect semiconductors compared to direct ones [16].

2.1.2.2 Urbach edge transitions

Disorder in the crystal typically leads to electronic states within the band gap. Optical absorption via these states is empirically described with an exponential dependence below the band gap,

$$\alpha(E) \propto \exp\left(\frac{E - E_1}{E_0}\right) , \tag{19}$$

where E_1 is an energy near the bandgap and E_0 is known as the Urbach energy, which is used as a measure of the energetic disorder in the electronic states near the band gap. This relationship has been used to describe absorption close to the band edge for a variety of materials, both with indirect and direct bandgaps, but has been variously assigned to phonon-assisted absorption (crystalline Si [19], GaAs [20]), or static disorder (amorphous Si [19]). These can be distinguished by the temperature dependence of E_0. Sub-bandgap states may also arise, even in an ideal crystal, through electron–electron interactions, which will be discussed in the following section.

2.1.3 Electron–electron interactions

2.1.3.1 Excitons

Excitons are a bound state of an electron–hole pair [21]. Due to their opposite charges, an electron and a hole will attract one another via Coulomb interactions but, depending on the surrounding medium, this attraction is screened to different extents. For very strongly bound excitons, named Frenkel excitons, the separation between electron and hole is one or two unit cells. These typically occur in organic semiconductors and ionic crystals. For weakly bound, "Wannier-Mott" excitons, the charges are screened more effectively by the medium (in semiconductors with large dielectric constants, for example, GaAs) and the radius of the exciton encompasses several unit cells. The binding energy and radius of a Wannier-Mott exciton can be calculated by considering a hydrogen atom, modified by the relative permittivity of the medium and using a reduced mass composed of the electron and hole

effective masses. Therefore, the excitonic energy levels, E_n, can be expressed in terms of the hydrogenic Rydberg energy, R_H, as follows [10],

$$E_n = -\frac{\mu}{m_0}\frac{1}{\epsilon_r^2}\frac{R_H}{n^2} \quad , \tag{20}$$

where μ is the reduced mass ($1/\mu = 1/m_e^* + 1/m_h^*$), m_0 is the electronic rest mass, ϵ_r is the relative permittivity of the medium and n is the principal quantum number of the orbital. So the binding energy is defined by the $n = 1$ state. In addition, the radii of the exciton energy levels become,

$$r_n = \frac{m_0}{\mu}\epsilon_r a_0 n^2 \quad , \tag{21}$$

where a_0 is the hydrogenic Bohr radius. The excitonic Bohr radius is then the case where $n = 1$. The Wannier-Mott exciton centre of mass is free to move through the crystal with a wavevector of $\boldsymbol{K} = \boldsymbol{k}_e + \boldsymbol{k}_h$ and kinetic energy of $E = \hbar^2 K^2/2(m_e^* + m_h^*)$.

In some instances, excitons cannot move freely but are trapped at an interface, defect site or by deformation of the lattice. The latter will be discussed further in Section 2.1.4.4.

2.1.3.2 Band gap renormalisation

Band gap renormalisation is a shift of the energies of states near the band edge which can occur when a high density of charges are excited or induced through dopants and interact with each other in a many-body sense [22],[23]. The Coulomb interactions and mutual exchange interactions between the free electrons in the conduction band and electron-impurity scattering effects effectively give rise to a reduction in the CBM and an increase in the VBM energies. The band gap therefore reduces in a way that is dependent on the excited carrier density, albeit weakly ($\Delta E \propto N^q$, where $q < 0.5$).

2.1.4 Electron-phonon interactions

The interactions between electronic states and vibrations of the lattice are important for many processes in both direct and indirect semiconductors. Phonon-assisted absorption at the band edge was already discussed in Section 2.1.2.1 but carriers may also scatter with phonons and make intraband transitions between k-states. This allows charge carriers excited high in the

band to relax to band edge states [24] and in many semiconductors, phonon scattering reduces conductivity at high temperatures [10].

2.1.4.1 Phonons

Phonons derive from the $H_{\text{ions}}(\boldsymbol{R}_j)$ part of Equation 1, which can be Taylor expanded around the equilibrium positions of the ions, $\boldsymbol{R}_{j0}$, to second order, to yield a harmonic oscillator approximation for small displacements of the ions. The normal modes of this system of harmonic oscillators, with quantised energy levels, are referred to as phonons [10]. As for electrons, the periodicity of the crystal means that phonons have a dispersion relation, $E(\boldsymbol{q})$, where $\boldsymbol{q}$ is the wavevector or spatial frequency of the phonon. Acoustic phonons can be thought of as density waves travelling through the material. They have the lowest energies, and at the limit of low wavevector, their dispersion is linear, with $dE/dq = v_{ac}$ giving the speed of sound in the material. Optical phonons are modes which involve neighbouring ions moving in opposite directions. They have higher energies than acoustic phonons for the same wavevector, which leads to upper branches in the phonon dispersion curve.

Phonons are bosonic quasiparticles and are thermally excited according to Bose-Einstein statistics. The probability of finding a phonon of energy E_{ph} in the material at temperature T is [11],

$$f(E) = \frac{1}{e^{(E_{ph})/k_B T} - 1} \ . \tag{22}$$

The phonon occupation is important for determining the temperature dependence of any processes involving absorption of phonons, such as indirect bandgap absorption and phonon-assisted recombination.

2.1.4.2 Types of electron-phonon interaction

Electron-phonon interactions are represented by the Hamiltonian $H_{\text{e-ion}}(\boldsymbol{r}_i, \delta\boldsymbol{R}_{j0})$ in Equation 1. They can be described as polar interactions, deformation potential interactions or piezoelectric interactions [10].

The polar interaction between electrons and small wavevector (long wavelength), longitudinal optical (LO) phonons is normally dominant in polar or ionic crystals. This is where the LO phonon induces a macroscopic polarisation of the material, which gives rise to

an electric field. This electric field scatters with charge carriers in a way described as the Fröhlich interaction.

The deformation potential interaction between electrons and acoustic phonons arises due to a change in the electronic energy levels in response to distorted bond lengths or angles. The deformation potential interaction with transverse optical (TO) and LO phonons occurs only in crystals with at least two atoms in a unit cell, whereby the phonon changes the bond lengths or bond angles between them, which again changes the electronic energies.

The piezoelectric interaction occurs in non-centrosymmetric crystals, where an acoustic phonon produces a strain field which causes the material to become electrically polarised.

2.1.4.3 Polarons

Due to the polar interaction, the electric field surrounding a free charge carrier polarises the material around it in a way that partially screens the charge. The moving charge carrier and accompanying lattice polarisation can be represented as a single quasiparticle — a polaron [25]. This has a different E-k dispersion to the purely electronic states and therefore the effective mass, mobility and optical absorption will all be altered relative to carriers in the band. There are two categories of polarons arising based on the spatial extent of the polarisation: a large (or Fröhlich) polaron extends over many unit cells, whereas a small (or Holstein) polaron is approximately the size of a unit cell. The size is determined by the strength of the electron-phonon interaction, which is different for every material, and the radius of a large polaron can be calculated from the LO phonon mode frequency.

Large polarons occur in polar semiconductors with weak electron-phonon coupling, for example, GaAs and CdTe [12]. For large polarons, the Fröhlich coupling constant, α, relates the binding energy of the polaron, U_{pol}, to the LO phonon energy, $\hbar\omega_{LO}$,

$$\alpha = -\frac{U_{pol}}{\hbar\omega_{LO}} = \frac{e^2}{\bar{\epsilon}}\sqrt{\frac{m^*}{2\hbar^3\omega_{LO}}}\ , \tag{23}$$

where $1/\bar{\epsilon} = 1/\epsilon_\infty - 1/\epsilon_0$ and m^* is the effective mass of the carrier. The effective mass of a polaron is larger than a purely electronic band-like state because the lattice polarisation also has inertia. Fröhlich showed that the new effective mass is [12],

$$m_p^* = \frac{1+\alpha/12}{1-\alpha/12}m^*\ . \tag{24}$$

Small polarons form when the electron-phonon interaction is strong, for example in organic semiconductors and ionic crystals [25]. They are localised within a unit cell and may only travel by hopping from one site to the next. This re-organisation of the lattice has an energy barrier which means that the hopping is thermally activated and the mobility of small polarons increases with temperature. This is contrary to the behaviour of large polarons, where increased electron-phonon scattering reduces the mobility at higher temperatures.

2.1.4.4 Self-trapped excitons

Self-trapped excitons (STEs) have been observed in alkali halide ionic crystals [26], 2D layered lead halide perovskites [27], and bismuth halide-based 'defect halide perovskites' [28]. They can be thought of as a small polaron which has a charge carrier of the opposite sign in a bound state orbiting it. In the case of alkali halides, a self-trapped hole usually forms as a new chemical bond between neighbouring halide ions, producing an $(X_2)^-$ ion [26]. In silver chloride, AgCl, there are also self-trapped holes but they usually localise on the silver ion, producing Ag^{3+}. The difference may be explained by the character of the valance band edge states, which have mostly halide *p*-orbital contributions in alkali halides, but a combination of halide *p*- and silver *d*-orbital contributions in AgCl. Much like small polarons, STEs can move by thermally-activated hopping from site to site.

STEs characteristically emit one or more broad PL bands which can be Stokes shifted by more than 1 eV from the band edge. The emission remains broad at low temperatures, and increases in intensity due to the suppression of thermally activated quenching routes [26].

2.1.4.5 Impulsive excitation of coherent phonons

As with electrons, certain phonons may be excited optically. Direct absorption of a photon can excite IR-active phonons which, in centrosymmetric crystals, are optical phonons at the Γ-point with odd parity [10]. Phonons near the Γ-point ($q = 0$) with even parity are Raman-active (in centrosymmetric crystals), meaning that they can be excited by Stokes Raman scattering. Raman scattering is an inelastic process where the incident photon, the scattered photon and a phonon interact *via* a virtual state and the energy difference between the two photons is the energy of the phonon. If the energy of the incident photon is below the

electronic transition energy, then vibrational modes of the ground state can be probed and if the photon is resonant with an electronic transition, vibrational modes of the excited state can also be observed.

Time-resolved spectroscopic studies of phonons in solid semiconductors, semimetals, superconductors and insulators have previously been performed using ultrafast transient absorption [29][30][31]. Phonons may be excited by impulsive stimulated Raman scattering (ISRS), using a non-resonant (sub-bandgap), short (lasting less than half of the phonon time period) pulse of light, with a spectral linewidth broader than the phonon energy. This is represented in Figure 2.1 by photons with energies $\hbar\omega_1$ and $\hbar\omega_2$, which are both incident in the same short pulse, and which excite a phonon wavepacket of energy $\hbar\omega_{ph} = \hbar\omega_1 - \hbar\omega_2$. These phonons can be detected by the short probe pulse as long as they remain coherent – either by shifting the frequency of the probe itself or by modulating the transmission through the material.

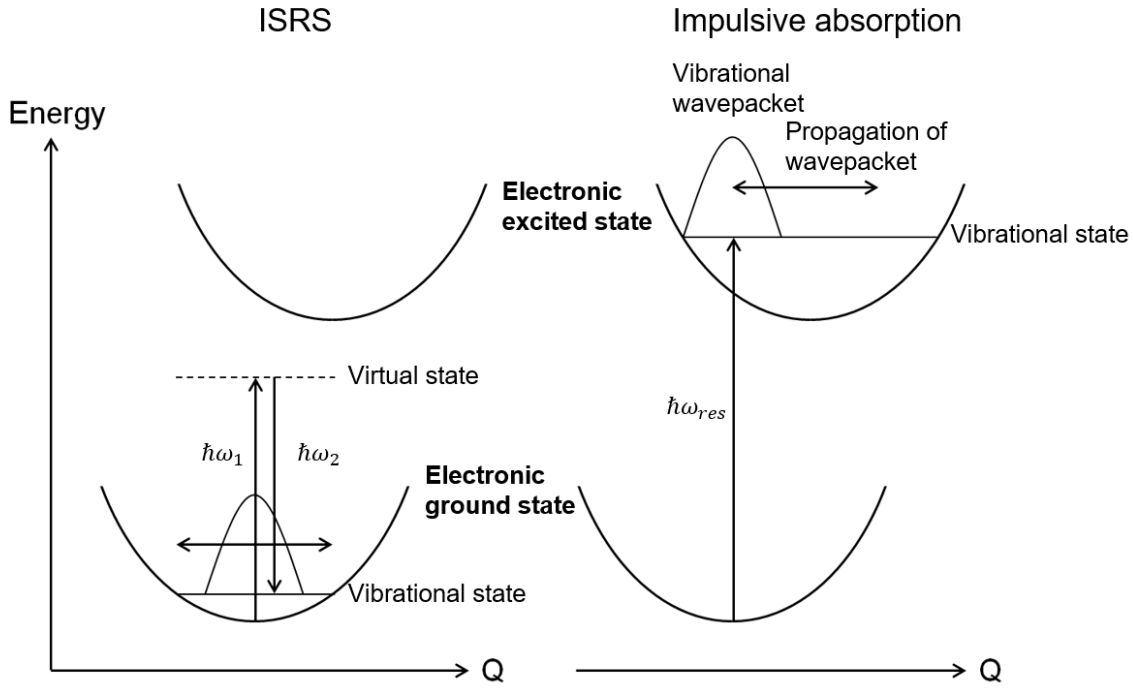

Figure 2.1 Impulsive excitation of coherent phonons by a short pulse of light. Q represents the nuclear displacement of the ions, peaks represent the vibrational wavepackets excited. (Left) ISRS mechanism with a sub-bandgap photon energy. The bandwidth of the excitation must be broad enough to include the phonon energy in order to perform stimulated Raman scattering. (Right) Impulsive absorption mechanism with an above-bandgap photon energy. The excited state of the system has shifted equilibrium positions of the nuclei so the system oscillates transiently after photoexcitation before achieving quasi-equilibrium.

Time-domain techniques, such as sub-bandgap transient absorption, in principle provide much the same information as frequency-domain, steady-state Raman spectroscopy, such as phonon energies and lifetimes [10], but with the added benefit of resolving the time evolution of the transiently excited phonons [30]. However, time-domain techniques are limited by the time resolution that can be achieved which depends on the minimum duration of the laser pulses which can be realised [24].

When a resonant or above-bandgap excitation pulse is used, coherent phonons may be produced either by ISRS or 'impulsive absorption' (Figure 2.1). The impulsive absorption mechanism is invoked to explain the observation of coherent A_1 symmetry phonons in inorganic crystals such as elemental bismuth and antimony [32][33]. Coherent phonons are excited when the free carriers excited into the bands reduce the screening of the positive ions from each other and thereby shift the equilibrium positions of the ions. During a short photoexcitation, the ions do not have time to respond to the new energy landscape, so coherent phonons are initiated for modes which are vibronically coupled to the excited state. Therefore, a resonant transient absorption measurement with oscillations corresponding to some of the Raman-active phonons is an indicator of which modes couple strongly to the excitations.

These coherent oscillations may be detected as a change in the transition energy between the ground state and the excited state population [30], or as a modulation of the amplitude of the excited state transient absorption signals [29].

2.1.5 Broadening mechanisms

Optical absorption and emission spectra can differ from the ideal, predicted spectra due to different sources of broadening. This can be related to the lifetime of the transition, 'homogeneous' broadening, or the distribution of available states in the material, 'inhomogeneous' broadening [10].

Homogeneous broadening is visible when the transition energies of all the absorption or emission events are the same. It arises due to the quantum mechanical uncertainty relation between time and energy, $\Delta E\, \Delta t \leq \hbar/2$ [34]. Therefore, shorter-lived states will have a broader spectral shape, described by a Lorentzian profile. Collisions between carriers and

scattering with phonons can also give rise to this shape of spectrum. The broadening caused by interactions with phonons can also be spectrally asymmetric, as processes involving emission of a phonon are more probable than those requiring absorption of a phonon.

Inhomogeneous broadening is mostly due to disorder in the crystal, which causes the energy of transitions to vary in different environments, for example, at surfaces, grain boundaries or defects. Due to the statistical nature of these variations, the spectral shape at room temperature is usually Gaussian. However at low temperatures, the energies of specific defect states may be distinguished.

2.1.6 Recombination

After absorption of photons, electrons and holes populate the bands in higher quantities than the thermal equilibrium state of the semiconductor. While in the bands, they dissipate energy in order to achieve quasi-thermal equilibrium with the lattice. There are then a number of processes by which they can recombine and restore full equilibrium in the material. The recombination pathway which dominates depends on the band gap, defect concentration, and also the conditions under which the material was excited.

2.1.6.1 Shockley-Read-Hall recombination

The Shockley-Read-Hall (SRH) recombination mechanism is the trapping of carriers at defects and impurities leading to eventual recombination of an electron and hole [35]. In order to trap an electron or hole, a defect must create a bound state with an energy level within the band gap. Each recombination event has two steps: initially one carrier is trapped into the bound state with the defect, and subsequently the oppositely charged carrier is captured and recombines either non-radiatively or radiatively. There is another possibility, which is that the initially trapped carrier is thermally re-excited into the band, and this becomes increasingly likely the closer in energy the mid gap state lies to one of the bands.

The rate of SRH recombination to a certain trap has the following dependence on carrier density [16],

$$\Gamma_{SRH} = \frac{np - n_i^2}{\tau_e\left(n + n_{\text{trap}}\right) + \tau_h\left(p + p_{\text{trap}}\right)}\ , \tag{25}$$

where n_i is the intrinsic carrier density, τ_x are the lifetimes of the electron or hole in the trap state, n_{trap} and p_{trap} are the electron and hole densities for the case where their quasi Fermi

levels are at the trap state energy. This simplifies to a linear relationship in the case of highly doped semiconductors or when the trapping lifetime of one carrier is significantly longer than the other.

2.1.6.2 Radiative recombination mechanisms

When an electron and hole recombine from states in the band, they may do so by emitting a photon. This process is governed by the physics of spontaneous emission. The rate of spontaneous emission for a two level system is described in terms of the absorption and stimulated emission rates by Einstein's A and B coefficients [36].

If there are N_b species in the excited state and N_a species in the lower energy state, and the rate of spontaneous emission is A, the number of spontaneous transitions to the lower state is $N_b A$, per unit time. Labelling the probability of absorption of a photon, B_{ab}, and stimulated emission B_{ba}, which are calculated using Fermi's golden rule (Section 2.1.2), we can write the rate equation for the number of excited species as,

$$\frac{dN_b}{dt} = -N_b A - N_b B_{ba} \rho(\omega_0) + N_a B_{ab} \rho(\omega_0) \,, \tag{26}$$

where ω_0 is the angular frequency of the transition between a and b, and $\rho(\omega_0)$ is the photon density at this frequency. Assuming the levels are non-degenerate for simplicity and considering detailed balance, it must be true that $B_{ba} = B_{ab}$. When the condition of thermal equilibrium is met, the overall rate of change is zero, so A may be expressed in terms of the known quantities. The ratio N_a/N_b is calculated using the Boltzmann occupation densities.

In the absence of an externally applied electromagnetic field, the absorption and stimulated emission processes may only occur using the photons present in equilibrium due to black body radiation. According to Planck's law of black body radiation, the radiation density in free space is,

$$\rho(\omega) = \frac{\hbar}{\pi^2 c^3} \frac{\omega^3}{e^{\hbar\omega/k_B T} - 1} \,, \tag{27}$$

where ω is the angular frequency of the photon and c is the speed of light, which must be replaced with c/n in a medium. All together, this gives,

$$A = \frac{\hbar \omega_0^3}{\pi^2 c^3} B_{ba} \ . \tag{28}$$

Generalising from a two-level system to a semiconductor, the radiative recombination of an electron and hole should therefore depend on the square of the transition dipole moment, $|\boldsymbol{p}|^2$. This is a property of the band edge states, as discussed in Section 2.1.2 in relation to absorption.

Furthermore, for free electrons and holes, the rate of spontaneous emission is proportional to both population densities [16]; $\Gamma_{\text{bimol}} \propto np$. This can be rationalised as the probability of an electron and hole being spatially close enough to recombine which leads to the name bimolecular recombination. In an intrinsic system with intrinsic electron and hole densities, n_i and p_i, which has been photoexcited to produce an excess number of electrons and holes, n_{ex} and p_{ex}, respectively,

$$\frac{dn}{dt} = -b(n_i p_i + n_i p_{ex} + p_i n_{ex} + n_{ex} p_{ex}) \,. \tag{29}$$

where b is a constant of proportionality. For wide band gap semiconductors under illumination, the photoexcited carrier population is usually much greater than the intrinsic carrier density. The rate of radiative recombination is then dominated by the final term, which is quadratic in excitation density, i.e. $dn/dt \propto n_{ex}^2$.

The quadratic dependence does not apply for doped semiconductors, because the density of majority carriers is usually much greater than the photoexcited carrier density, therefore the radiative rate only depends on the minority carrier population, which is linear in excitation density.

The rate is also linear for bound excitonic systems, in which the electron and hole wavefunctions already overlap for a significant amount of time before emission. Here the rate only depends on the density of excitons, i.e. $dn/dt \propto n_{ex}$. This is called geminate recombination [37].

2.1.6.3 Auger recombination

Auger recombination is a three-body process where an electron-hole pair may recombine by promoting a third carrier to an energy high above the band gap [38][16]. This high-energy carrier then thermalizes to the band edge by emitting phonons, so the energy of the original electron-hole pair is dissipated as heat. This process requires all three carriers to be coincident, so $dn/dt \propto n_{ex}^3$. Auger recombination is therefore especially prominent at high

excitation densities or in nanostructures where the carrier wavefunctions are spatially confined.

2.1.6.4 Total recombination rate

In experimental studies of charge carrier recombination in various materials, the charge carrier population is excited with a short pulse of light and the charge carrier population is observed as a function of time afterwards. Considering that all the processes discussed thus far may all contribute simultaneously to the rate of carrier recombination, the total rate of recombination in a material can be expressed as [39],

$$-\frac{dn}{dt} = an + bn^2 + cn^3 \,, \tag{30}$$

where n is the photoexcited carrier density, and a, b and c are the individual rates for monomolecular, bimolecular and trimolecular processes, respectively. To simplify the differential equation, for low excitation density experiments, bimolecular and Auger recombination can be neglected, leaving only the linear term. This gives rise to a monoexponential decay of carriers after photoexcitation,

$$n(t) = n_0 e^{-at} \,, \tag{31}$$

for an initial carrier density of n_0. The characteristic lifetime of the carriers is then $\tau = 1/a$.

For experiments at higher carrier densities, the bimolecular term must also be included. The analytical solution to the remaining differential equation is,

$$n(t) = -\frac{a}{b - Ae^{-at}} \,, \tag{32}$$

where $A = b + a/n_0$. Therefore, when the excitation density is increased the decay should deviate from the monoexponential regime once band-to-band radiative recombination becomes significant. For doped semiconductors, this threshold is an indication of the dopant density.

Understanding the recombination timescale and mechanism of charge carriers is important for improving solar cell performance as the charge carriers only produce electrical power when extracted from the material. The timescale for extraction therefore sets the minimum desired lifetime of the carriers. In the following sections, I will discuss further the context in which semiconductors are used in photovoltaic devices and the limits to their efficiency.

2.2 Photovoltaic devices

Solar photovoltaics are devices which convert light energy from the sun into useful electrical energy [16]. The application of these devices ranges from remotely powering satellites and other off-grid locations, to feeding into the grid as a renewable alternative to fossil fuels. Different materials and device architectures are deployed in each scenario, therefore an understanding of the overarching principles of solar cell operation and efficiency is important for making materials choices. In this section we explore how the previously discussed physics of semiconductors is exploited in photovoltaic devices.

The most standard solar cell device is formed by an *n*-doped region adjacent to *p*-doped region of semiconductor. This arrangement, called a *p*–*n* junction, made from silicon was developed by researchers at Bell Labs in 1953 [40] and is now the main contributor to global photovoltaic capacity [4]. 67 years of research on this type of device increased its power conversion efficiency (PCE) from 6% to 25% and research into improvements of the crystalline silicon solar cell is ongoing [41]. Since silicon is an indirect semiconductor, higher efficiencies were achieved in GaAs devices but due to existing infrastructure for high purity silicon processing, economic factors led silicon to continue to dominate the market. I will now summarise the large volume of research on the silicon *p*-*n* junction and the theory of solar cell operation in order to inform our search for the next generation of materials for photovoltaics.

2.2.1 Device structure

In general, a solar cell produces a voltage by absorbing light, creating charge carriers, and separating the electrons from the holes. An asymmetric structure is required to achieve the last step, for example the *p*–*n* junction described or by using layers of different materials.

2.2.1.1 Homojunctions

If a *p*–*n* junction is formed using the same semiconductor for both regions, it is labelled a ‘homojunction’. The Fermi energy of the intrinsic semiconductor would therefore be the same on both sides, but the doping has caused the Fermi level to become pinned to the

acceptor and donor levels of the *p*- and *n*-doped sides respectively [10]. When the two sides are in contact, this would lead to an imbalance of the chemical potential. In equilibrium, electrons from the n-type region occupy states in the p-type region, depleting both types of charge carrier at the interface which creates a 'depletion region' or 'space charge region' [42] (Figure 2.2). The charged, ionised dopants set up an electric field across the depletion region which realigns the Fermi levels. The voltage across the junction, called the built-in voltage, can be found by considering the dopant densities of the *n*-type and *p*-type region, N_n and N_p, respectively, and the intrinsic carrier density, n_i :

$$V_{bi} = \frac{k_B T}{q} \ln\left(\frac{N_n N_p}{n_i^2}\right), \tag{33}$$

where q is the electronic charge. Charges moving through the depletion region create a drift current, driven by the built-in potential, which, in equilibrium, is balanced by a diffusion current in the quasi-neutral regions on either side of it [43].

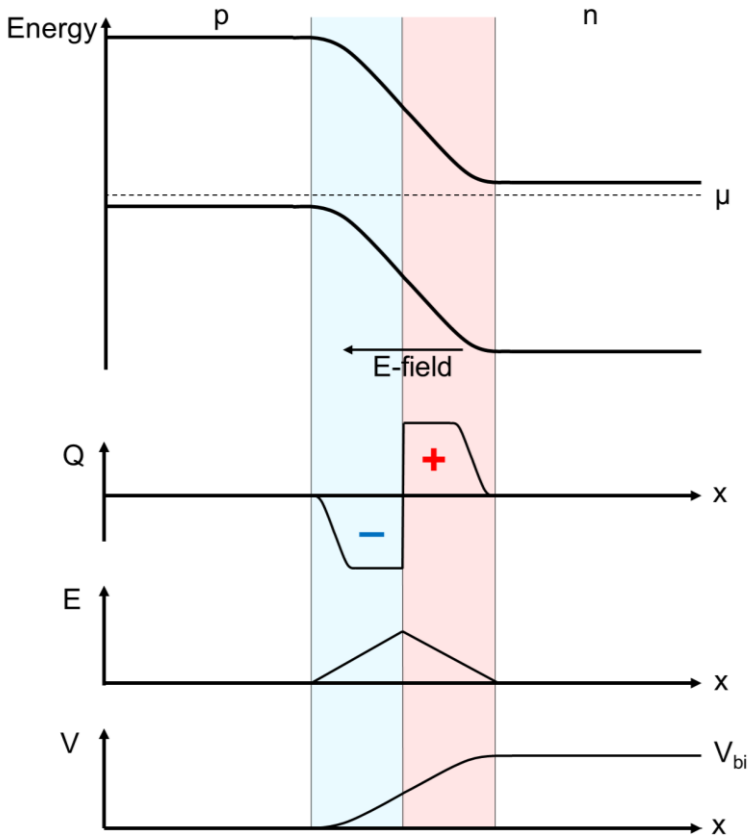

Figure 2.2 Schematic of the conduction and valence band energy levels, charge density, Q, electric field magnitude, E, and built-in voltage, V, in a *p-n* junction in equilibrium. The shaded region is the space charge region, and either side are the quasi-neutral regions. The bands bend such that the chemical potential is constant across the junction. Based on a figure in [42].

Due to recombination, diffusing carriers can travel an average distance, l_D, which is limited by the charge carrier lifetime, τ, and the diffusivity, D, where,

$$l_D = \sqrt{D\tau} \ . \tag{34}$$

The diffusivity is related to the carrier mobility, μ, by the Einstein relation , $D = \mu k_B T/q$.

The *p*-*n* junction is also the basis of a diode as a voltage applied in only one direction can lead to the flow of charge carriers — a 'forward bias' which acts against the built-in potential to allow electrons from the *n*-type region to overcome the barrier and flow through the *p*-type region as 'minority carriers', and holes to flow the opposite way. In other words, the diffusion current must overcompensate the drift across the depletion region.

Additionally, in a solar cell, absorbed photons from the solar spectrum generate electron-hole pairs in the device which, on reaching the depletion region, significantly increase the number of minority carriers contributing to the drift current. This leads to a non-zero current even when no bias is applied called the 'short circuit current' or, when under open circuit conditions, a charge imbalance giving rise to the open circuit voltage.

2.2.1.2 Heterojunctions

Heterojunctions use layers of different materials to achieve charge carrier separation across the device. A typical *p*-*i*-*n* heterojunction device consists of an intrinsic absorber layer with a hole transport layer (HTL) on one side and an electron transport layer (ETL) on the other [44] (Figure 2.3). The materials studied in this thesis have been, to date, exclusively used in *p*-*i*-*n* heterojunction solar cells, as an intrinsic absorber layer. This eliminates the need for doping but the carrier-selective contacts must be carefully chosen such that the band gaps are larger than the absorber layer and their valence (HTL) or conduction (ETL) band edge aligns as closely as possible with the absorber layer's band edges. If the Fermi levels are not aligned, the same considerations as above must be applied, as this causes band bending which may impede or enhance charge extraction from the absorber layer.

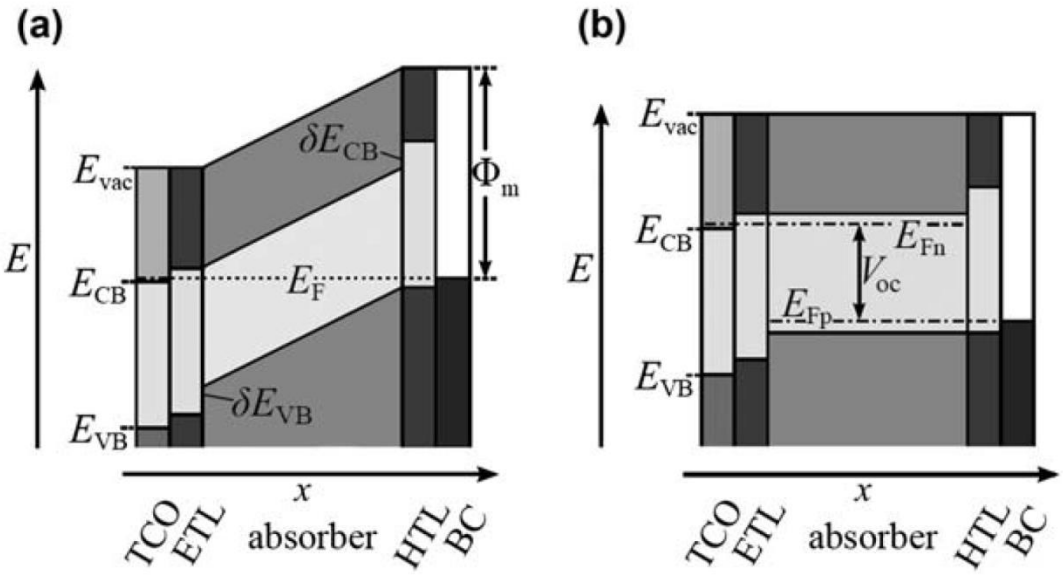

Figure 2.3 Schematics of an ideal p-i-n junction under (a) short circuit and (b) open cicuit conditions. The device consists of a metallic back contact (BC), hole transport layer (HTL), intrinsic absorber, electron transpot layer (ETL), and a transparent conducting oxide (TCO) top electrode. The efficiency is maximised when the conduction band of the top electrode aligns with the quasi-Fermi level of electrons (E_{Fn}) in the absorber layer and the BC work function (Φ_m) aligns with the hole quasi-Fermi level (E_{Fp}). Figure from ref [44].

2.2.2 Solar cell operation and efficiency limits

The standard measure of the efficiency of research solar cells is the power conversion efficiency (PCE) which is the total electrical power obtained per unit of solar radiation power used to illuminate it [16]. A standard solar spectrum of air mass (AM) 1.5 is used to enable comparison between different cells, chosen in order to simulate the solar spectrum at the Earth's surface at a zenith angle of 48.2°. This represents an approximate yearly average for mid-latitudes. The electrical power is measured by sweeping the bias across the cell and measuring the current, known as a J-V curve (Figure 2.4).

In the dark, an ideal *p-n* junction solar cell has a J-V curve of the form of a diode [43],

$$J_{\text{dark}} = J_0\left(e^{qV/k_B T} - 1\right) . \tag{35}$$

Under illumination, a photocurrent flows in the opposite direction, leading to a current density of,

$$J_{\text{light}} = J_0(e^{qV/k_B T} - 1) - J_{SC} , \tag{36}$$

where J_{SC} is the short circuit current. At some position along the J-V curve, there is a point where the power output (the area J × V) is maximised, P_{max}. This is what is used for the PCE calculation.

Another important indication of device performance is the open circuit voltage, V_{OC}. For the ideal case, it is related to the short circuit current, J_{SC}, by setting $J_{\text{light}} = 0$,

$$V_{OC} = \frac{k_B T}{q} \ln\left(\frac{J_{SC}}{J_0} + 1\right). \tag{37}$$

In addition, the fill factor, FF, is the ratio of the maximum power to the product, $J_{SC} \times V_{OC}$, and can be used as a measure of losses which cause the finite gradients at J_{SC} and V_{OC}. These resistances are called the series resistance and shunt resistance, respectively.

$$FF = \frac{P_{\text{max}}}{J_{SC} V_{OC}}. \tag{38}$$

The PCE can therefore be expressed as,

$$\eta = \frac{FF\, J_{SC}\, V_{OC}}{P_{AM1.5}}. \tag{39}$$

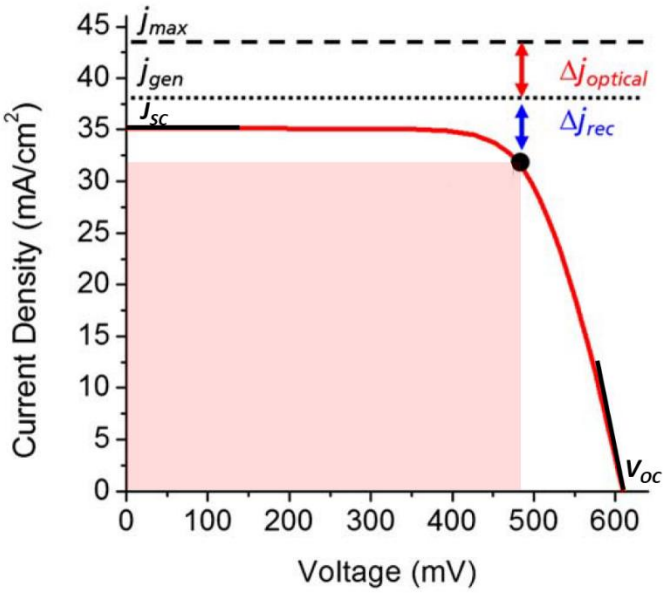

Figure 2.4 J-V curve for a crystalline silicon solar cell. The maximum power point is indicated with a black dot, with the maximum power, P_{max}, represened by the pink area. The effect of various loss mechanisms is also shown: $\Delta j_{\text{optical}}$ are current losses due to reflection, escaped light and parasitic absorption and Δj_{rec} is recombination of the generated charge carriers. The solid black lines indicate the series resistance at J_{SC} and the shunt resistance at V_{OC}. Figure modified from ref [44].

The external quantum efficiency (EQE) of a device is the number of charge carriers extracted for every photon incident on the sample. This is dependent on the energy of the incident

photons, and integrating over the solar spectrum returns the value of J_{SC}. EQE measurements can be used to identify losses occurring for different regions of the solar spectrum.

The theoretical efficiency limit of a solar cell made from a single absorber is set by its band gap. The Shockley-Queisser limit stems from the fact that no photons below the band gap energy can be absorbed, and that carriers excited higher than the band gap energy dissipate their excess energy as heat [45]. It is derived using the principle of detailed balance, which requires that the recombination of carriers under open circuit conditions is purely radiative, and assuming that: the sun and the solar cell are black bodies at temperatures of 6000 K and 300 K, respectively; carriers occupy band edge states by the time they are extracted, and no photons with energies below the band gap may be absorbed. For this ideal case, the maximum PCE of a single junction solar cell is 33%, corresponding to band gap energies in the range 1.1–1.3 eV.

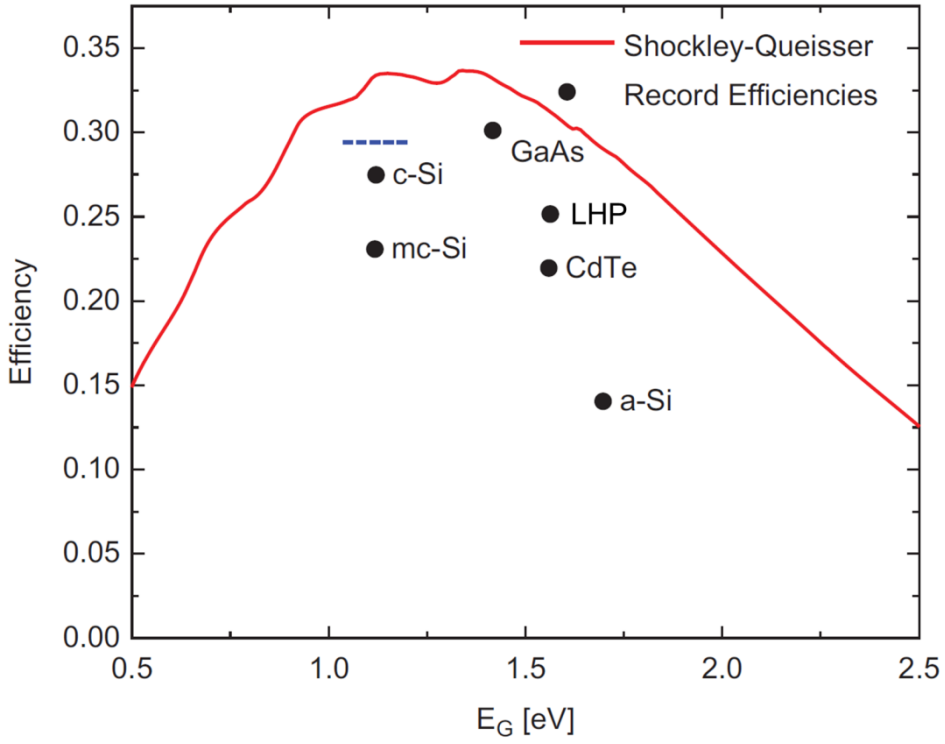

Figure 2.5 Schockley-Queisser limit as a function of the band gap of a single junction solar cell. Record efficiencies as of 2019. The dashed blue line represents the theoretical efficiency limit for crystalline slicon if Auger recombination is considered as a loss mechanism. Figure modified from ref [44].

The assumption that recombination is purely radiative is rarely valid in real semiconductors. In Section 2.1.6.4 it became clear that if defect states are present in the middle of the gap, the rate of non-radiative SRH recombination is significant, especially at low carrier densities. Furthermore, for indirect bandgaps, the low transition rate for radiative recombination increases the probability that carriers will diffuse to a recombination centre before emitting [16].

The effect of non-radiative recombination is to lower the open circuit voltage. When charges are being extracted before they recombine, for example, under short circuit or operating conditions, the current density is not affected. However, the open circuit voltage requires charges to remain in the material and is therefore related to the external PLQE, η_{ext}, (defined as the number of photons emitted per photon incident on the cell) where,

$$qV_{OC} = qV_{OC,\,\text{ideal}} - \frac{k_B T}{q}\ln(\eta_{ext})\,. \tag{40}$$

This has led external PLQE or even electroluminescence EQE to be used as a measure for photovoltaic performance, despite the operating conditions being different from those at open circuit.

Overcoming the Schockley Queisser limit can be achieved by combining junctions with different band gaps in a 'tandem' solar cell device. In a tandem solar cell, multiple cells are stacked so that the highest band gap material is on the top, which absorbs the high energy photons but allows the lower energy photons to pass through to the lower band gap materials (Figure 2.6) [46]. Theoretically, the optimum band gaps for a double junction tandem solar cell are 1.0 eV and 1.9 eV, giving a limiting PCE of 42.3% [47]. Therefore, research into materials with significantly higher bandgaps than 1.3 eV is relevant for use as top cells in conjunction with a crystalline silicon bottom cell.

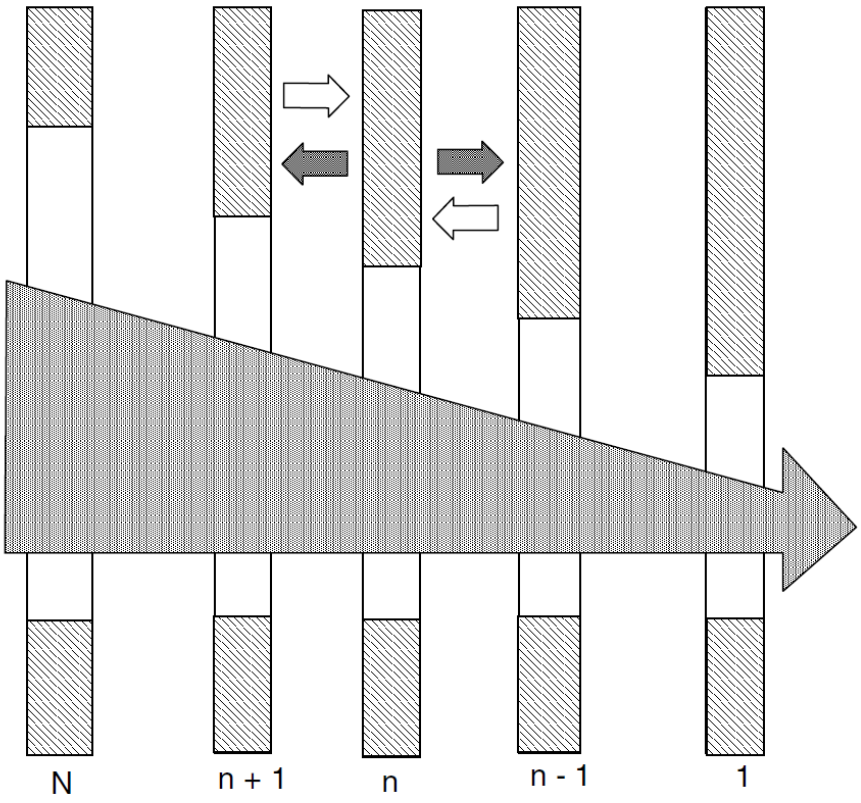

Figure 2.6 Schematic representation of a multi-junction tandem solar cell with decreasing band gap energies from left to right. Incident photons of higher energies are absorbed by the top cells and the lower energy photons pass through and are absorbed by the lower band gap materials. The smaller arrows represent light emmitted from cell *n*, which may be recycled within the device. Figure from ref [46].

2.3 Solution-processed inorganic semiconductors for next-generation solar cells

Research on thin film technology for solar cells has historically focused on amorphous Si:H, $Cu(In,Ga)Se_2$ (CIGS) and cadmium telluride (CdTe) [44]. However, the low abundance of some of the constituent elements and cost of manfacturing the high purities needed propelled research into a new generation of solar cells which can be produced cheaply and which may be more robust against defects. Organic semiconductors are solution processable and offer the widest parameter space to explore [37]. They have made impressive strides in efficiency, especially since the discovery of effective non-fullerene acceptors in 2018 [48]. However, organic semiconductors are characterised by low dielectric constants leading to strongly bound excitons and small polaronic charge carriers with hopping transport. This represents a fundamental loss of efficiency due to the energy barriers for charge separation and extraction

in devices. Device stability is also a major challenge due to the strong dependence of performance on a nanostructured bulk heterojunction.

For low-cost, high-efficiency solar cells, we wish to combine the solution processability of organic semiconductors with the advantageous charge screening and transport properties of inorganic semiconductors. To date, the most successful material system which combines these properties is the family of hybrid organic lead halide perovskite materials. I shall now provide some context about lead halide perovskites and the search for other materials relevant for this application.

2.3.1 Lead halide perovskites

The lead halide perovskites are solution processable crystalline semiconductors with an analogous crystal structure to calcium titanate, $CaTiO_3$. They have the chemical formula ABX_3 where A is a large monovalent ion, for example, caesium or methyl ammonium, B is a lead ion and X is a halide ion [49]. Their electronic properties derive from the network of corner sharing lead halide octahedra, whereas the A-site cation is mainly used to fill space and for fine-tuning the structure and stability.

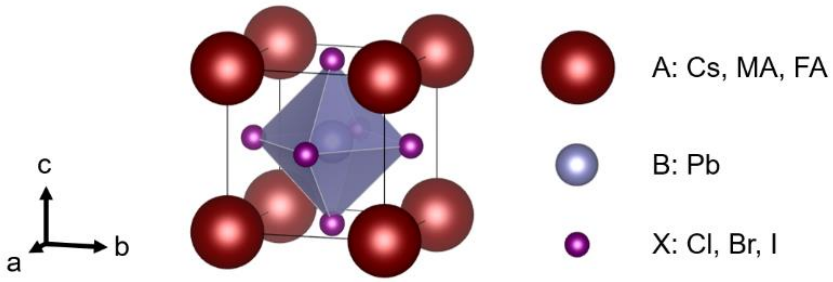

Figure 2.7 Unit cell of the lead halide perovskite crystal structure with cubic symmetry [50].

While the hybrid organic-inorganic methylammonium lead iodide ($CH_3NH_3PbI_3$) was first synthesised in 1978 [51], it was only investigated for photovoltaics as a sensitiser in a dye sensitised solar cell in 2009 [52]. The first solid state solar cell involving lead halide perovskite was made in 2012 and since then, a flurry of improvements has ensued from mixing bromide and iodide ions [53], introducing many different mixtures of cations into the A-site, and interface management [54]. Given their bandgap of 1.6 eV, their current record

efficiency of 25.2% is approaching their theoretical limit of efficiency [55]. They have also been successfully demonstrated in tandem solar cells with crystalline silicon, with efficiency now exceeding the single junction records for either material at 29.1% [7].

However, there are still barriers to widescale application of lead halide perovskites in solar cells, namely, the instability of devices when exposed to oxygen and moisture [8] and the toxicity of the lead [56].

Fundamental research on lead halide perovskite photophysics provides valuable lessons for future materials discovery. The remarkable success of such a structurally disordered material suggests that a broader view of semiconductor physics is required to understand which materials have the potential to perform well in solar cells. Some unexpected discoveries in polycrystalline perovskite films included photon recycling [57] and slow hot carrier cooling due to a hot phonon bottleneck [18] — phenomena previously observed in single crystal, epitaxially grown GaAs. Explanations for this lack of energetic disorder include the lack of mid-gap defect states because of the antibonding character of the valence band edge and bonding character of the conduction band edge states [58]. Also, the flexibility of the lattice (corresponding to small LO phonon energies), and strong electron-phonon coupling hinders the trapping of carriers and SRH recombination via shallow defect states [59]. There is an emerging consensus that charge carriers occupy an intermediate regime between small and large polarons [60]. The electrons and holes can be ‘protected’ by their partial screening and survive for longer in the material. The principles of band edge state bonding character and strong electron-phonon coupling have guided the search for lead-free alternatives presented in this thesis.

An interesting variant on the cubic lattice involves incorporating longer-chain organic cations in a ratio which enables layers of lead halide octahedra to self-assemble, separated by layers of organic ligands. As the electronic states near the band gap are dominated by the lead halide octahedra, this produces a 2D quantum well structure [61]. Quantum confinement of the charge carriers within the layers and reduced screening of the electron and hole charge encourage exciton formation. Using different organic ligands tunes the flexibility of the structure, giving rise to varying levels of electron-phonon coupling, which can strongly alter the emissive species — from free Wannier excitons with a narrow linewidth to self-trapped excitons (STEs) with broad white light emission [27].

2.3.2 Lead-free materials

One approach to reproduce the success of lead halide perovskites is to chemically substitute the lead ions for another group IV element, such as tin [62]. An advantage of this approach is the opportunity to lower the bandgap to 1.3 eV for methylammonium tin iodide ($CH_3NH_3SnI_3$), which is closer to the ideal for a single junction solar cell. Even lower bandgaps may be achieved by mixed tin-lead compositions due to band bowing. The record PCE for a pure tin halide perovskite stands at 8.71% [63]. On the other hand, tin halide perovskites are less stable than lead halides because of tin's tendency to oxidise from oxidation state (II) to (IV). There is also some toxicity associated with tin halide perovskites, although less than lead halides, prompting a further search for materials which are more benign.

Another approach is to explore bismuth halide based materials. Lead and bismuth are in the same period of the periodic table, so the Bi^{3+} ion has the same electronic configuration as the Pb^{2+} ion. To maintain charge neutrality, the structure of methylammonium bismuth iodide ($(CH_3NH_3)_3Bi_2I_9$) is not a perovskite crystal. However, this material is a solution-processable semiconductor with a band gap of 2.9 eV, which has been demonstrated as an absorber layer in solar cells with a PCE of 1.64% [64]. The charge carrier lifetimes of thin films of this material are longer than 1 ns, and they exhibit greater air stability than films of methylammonium lead iodide perovskite [65]. However, the crystal structure consists of pairs of face-sharing bismuth halide octahedra separated by organic ligands, which renders the electronic properties quasi zero-dimensional [66]. To aid charge transport, greater connectivity of the bismuth halide octahedra is required, which is present in materials such as BiI_3, $Rb_3Bi_2I_9$ (quasi-2D), and the double perovskite $Cs_2AgBiBr_6$ (3D).

Furthermore, computational studies have predicted that many bismuth halide based semiconductors share the same bonding character at the band edges as lead halide perovskites, which means they are unlikely to form mid-gap defect states [9]. Indirect band gaps in BiI_3 and $Cs_2AgBiBr_6$ [9] and parity forbidden band edge transitions in other double perovskites [67] may allow for slower recombination and greater diffusion lengths. However, device efficiencies have so far lagged behind their theoretical limits. As some of these materials have only recently been investigated for use in solar cells, this may be due to either a lack of optimisation of thin film thickness, microstructure, and carrier-selective contact choice, or there may be fundamental properties of the material which impede its efficiency.

2.3.2 Lead-free materials

The work in this thesis aims to study the fundamental photophysics of three of the most promising bismuth halide compounds demonstrated in photovoltaics so far: the double perovskite, $Cs_2AgBiBr_6$, and the layered compounds bismuth iodide, BiI_3, and bismuth oxyiodide, BiOI.

Halide double perovskites have the general formula, $A_2BB'X_6$, where A^+ and B^+ are monovalent cations, B'^{3+} is a trivalent cation and X^- is a halide ion. This allows the Pb^{2+} in lead-halide perovskites to be substituted for less toxic monovalent (e.g., Ag^+) and trivalent cations (e.g., Bi^{3+})[68][67]. The material $Cs_2AgBiBr_6$ was first synthesised and shown to have an indirect bandgap of 1.95 eV in 2016 (Figure 2.8(a) and (b)) [69]. Meanwhile, DFT calculations of the band structure by McClure et al. also predicted an indirect band gap (Figure 2.8(c)) [70]. In 2017, Greul *et al*. reported the first $Cs_2AgBiBr_6$ solar cell, with external quantum efficiencies up to 60% and PCEs of up to 2.43% [71].

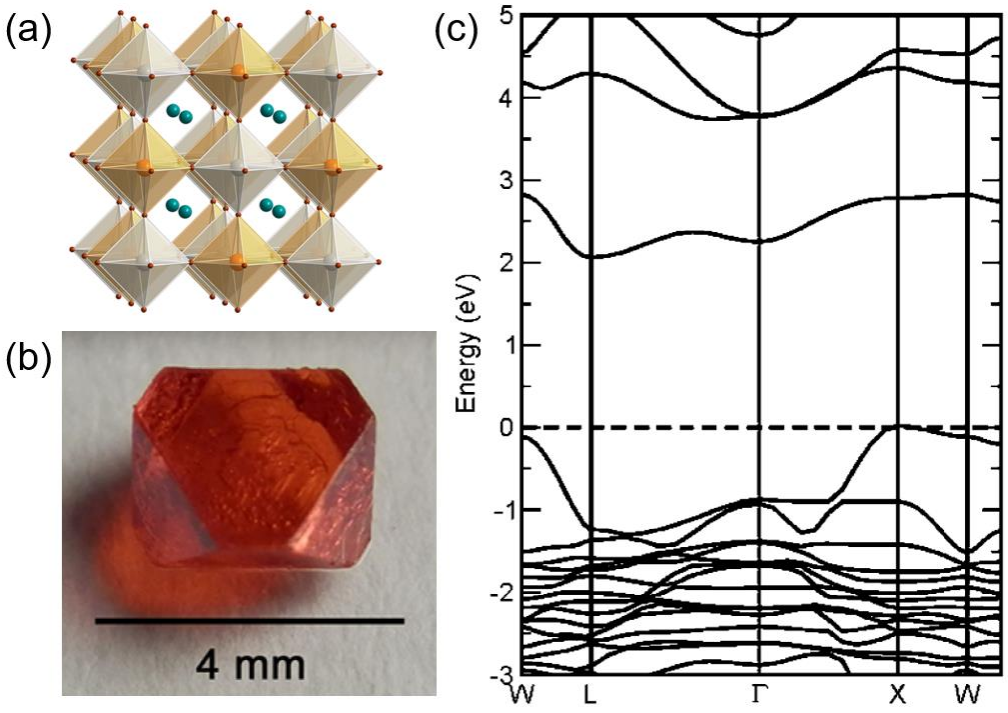

Figure 2.8 (a) Crystal structure of $Cs_2AgBiBr_6$ with green, grey, orange, and red spheres representing nuclear positions of Cs, Ag, Bi, and Br respectively. Figure from Ref. [69]. (b) Single crystal of $Cs_2AgBiBr_6$ as synthesised by Slavney *et al*. [69]. (c) Band structure calculated using DFT showing the CBM and VBM at the X and L high symmetry points, respectively. Figure from Ref. [70].

Bismuth triiodide has an indirect bandgap of 1.7 eV and strong optical absorption coefficients above 2 eV (Figure 2.9) [72][73]. The material was only recently applied in thin film

photovoltaics due to a new solution processing method [73][74], despite being studied as a single crystal for use in radiation detectors since the 1990s [75]. So far, PCEs of 1.0% have been achieved with solution processed BiI_3 [74].

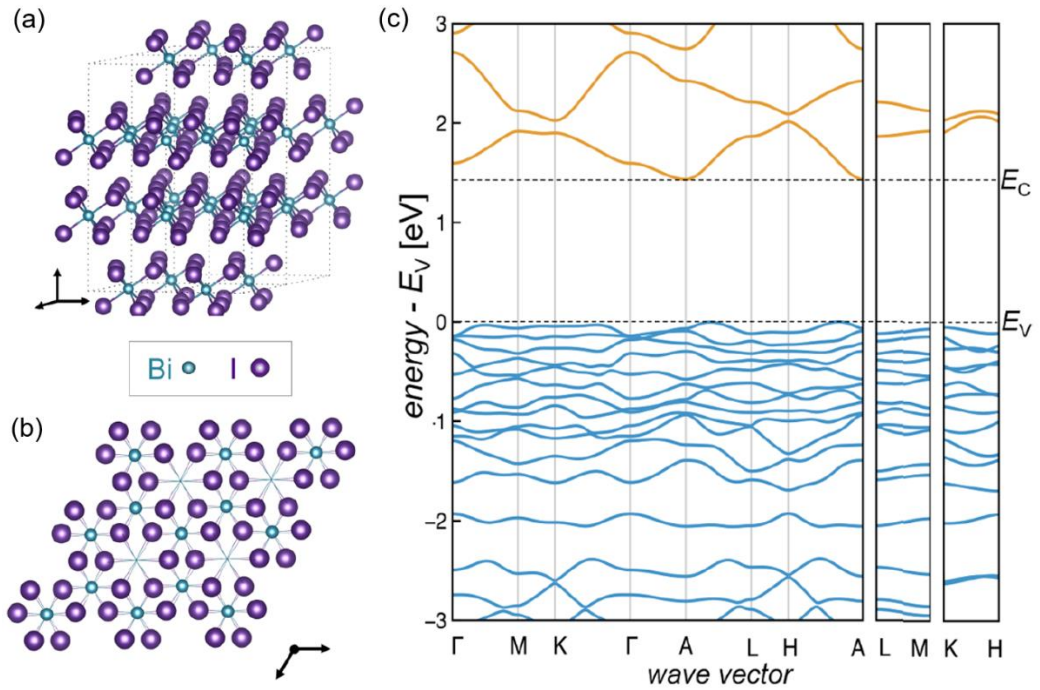

Figure 2.9 (a) 4x1 unit cells of the crystal structure of BiI_3 ($R\bar{3}$ symmetry) showing the stacking of the I-Bi-I layers. (b) Single I-Bi-I layer of BiI_3 viewed along the (0001) axis. (c) Band structure calculated using DFT showing the CBM at the A high symmetry point and the VBM along A to L and H to A. All figures from Ref.[73].

Bismuth oxyiodide is another indirect gap semiconductor, with a band gap of 1.9 eV (Figure 2.10) [76], which has also been proposed as a non-toxic alternative to perovskites for photovoltaic absorbers [77]. Polycrystalline thin films of the material grown using chemical vapour transport have been used as the absorber layer in solar cell devices with PCEs of up to 1.8% [78].

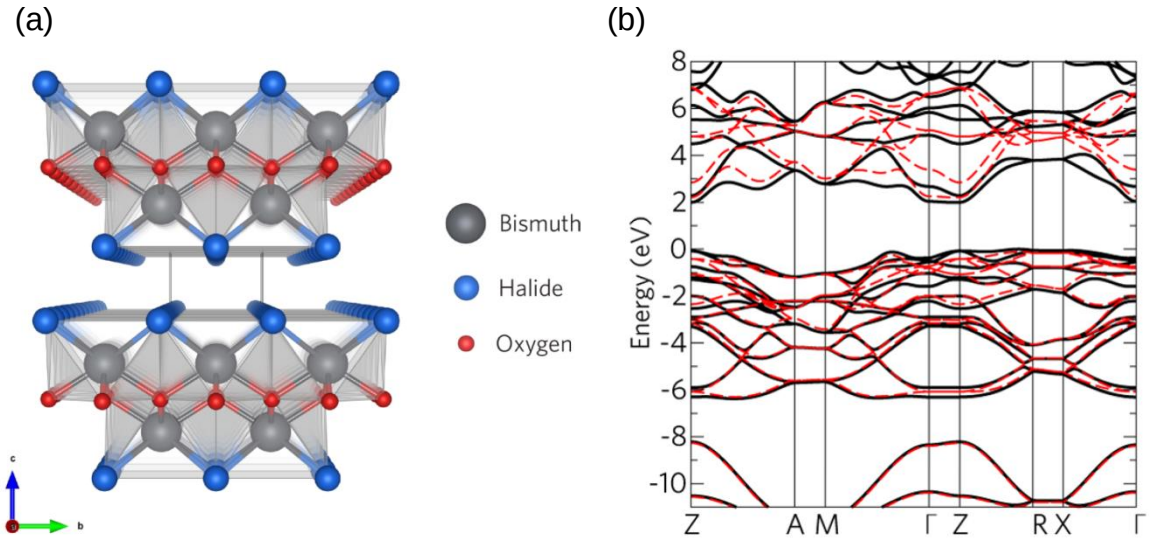

Figure 2.10 (a) Tetragonal matlockite crystal structure of bismuth oxyhalides, BiOX. (b) DFT calculated band structure of BiOI, accounting for relativistic and orbital effects. Both figures from Ref. [76].

While simple, steady-state spectroscopy including band edge absorption and photoluminescence measurements are useful to verify that each of these materials has a suitable band gap and low level of energetic disorder, time-resolved spectroscopy methods can also reveal which recombination processes are dominant. This knowledge allows us to identify loss mechanisms in devices and direct optimisation efforts or future materials discovery. In the next chapter, I detail the methods I used for such experiments.

Chapter 3: Experimental methods

Optical spectroscopy has proved a critical tool for studying light-matter interactions for many hundreds of years. When laser technology was developed, this vastly increased the scope of spectroscopy as higher powers of highly coherent, monochromatic light can be achieved – which is useful for detecting weak or nonlinear responses. Femtosecond pulsed lasers enable us to probe time-dependent effects with high temporal resolution. The main techniques employed in this work are described below.

3.1 Sample fabrication

3.1.1 $Cs_2AgBiBr_6$ double perovskite thin films

The thin films of $Cs_2AgBiBr_6$ used for my measurements were synthesised by Dr Robert Hoye (Faculty of Engineering, Department of Materials, Imperial College London) following a previously reported spin-coating method [71]. Briefly, $BiBr_3$, AgBr and CsBr precursor powders were dissolved in dimethylsulfoxide (DMSO) in stoichiometric proportions and preheated to 75 °C. A glass substrate was also preheated to 75 °C and the solution was spin coated at 2000 rpm for 30 s. The films were then annealed at 250 °C for 5 min inside a nitrogen-filled glovebox.

3.1.2 BiI_3 single crystals

BiI_3 single crystals were grown by physical vapour transport (PVT) by Robert Jagt (Department of Materials Science and Metallurgy, University of Cambridge). A low pressure two-zone tube furnace was used, with a total length of 50 cm. One gram of bismuth (III) iodide powder (Sigma Aldrich, ≥99.998% pure, trace metal basis) was placed inside a crucible. The quartz tube was pumped down to <0.1 mbar and flushed with argon to prevent oxidation of the BiI_3. The left and right side of the furnace were set to 350 °C and 200 °C, respectively. The crucible was placed inside the left zone, 15 cm from the tube furnace entrance. Argon was continuously flowing at 40 ml/min and the pressure in the tube was 13

mbar. The BiI_3 evaporated, was transported to the colder side of the furnace and condensed as single crystals on the inner wall of the tube. After 20 minutes, flakes of BiI_3 were formed with lateral sizes approaching 1 cm. The furnace was switched off and opened to let the crystals cool down. After the crystals had cooled down to room temperature, the tube was opened to the air and they were transferred from the inside of the tube into a nitrogen-filled glovebox for storage.

3.1.3 BiOI thin films

BiOI thin films were grown onto glass substrates with a 10 nm deposited layer of NiO_x by Dr Lana Lee and Tahmida Huq (Department of Materials Science and Metallurgy, University of Cambridge) using a chemical vapour transport method [78]. For this, a two-zone furnace was used with a quartz tube under atmospheric pressure. Both zones were preheated to 350 °C while substrates were attached to a glass slide with silver paste (Electrolube) and loaded into the quartz tube. 500 mg BiI_3 powder was placed in a crucible, at least 3 cm away from the substrates, and positioned at the edge of the heating rod of zone 1 of the furnace. The substrates were inside zone 2. An $Ar:O_2$ gas mixture was introduced to the closed tube (25 mL min^{-1} Ar, 0.3 mL min^{-1} O_2). After a 60 min growth time, the films were removed and measured to be approximately 700 nm thick by Dektak profilometry.

3.2 Low temperature X-ray diffraction

Low temperature powder X-ray diffraction (XRD) was collected using a Bruker D8 Discover diffractometer with an Oxford Cryosystems PheniX stage and with Cu Kα1,2 radiation (λ = 1.541 Å). Samples were mounted on a chromium coated copper puck using Dow Corning vacuum grease. The samples were first cooled to 12 K at a rate of 360 K/h under a pressure of $< 10^{-4}$ mbar. Measurements were taken after warming at the same rate to each temperature, scanning from 2θ = 10° to 2θ = 80°, with a resolution of 0.02° and 1 s integration time per step, such that each measurement took one hour. Rietveld refinement of collected powder diffraction data was performed using the open-source GSAS-II software package in Python. The background was modelled using a seven-component Chebyshev function. Crystallographic information files for refinement were obtained from the Inorganic Crystal Structure Database (ICSD: https://icsd.psds.ac.uk/). Background peaks originating from the

sample holder were fitted using copper and chromium phases. For the BiOI film, preferential orientation was modelled using a 10-component spherical harmonics function. Temperature dependent lattice parameters were obtained using a sequential refinement in GSAS-II. The XRD measurements and fitting were done by Tim van de Goor (Optoelectronics Group, Department of Physics, University of Cambridge (OE)).

3.3 Steady state optical absorption

3.3.1 Transmission and reflection spectroscopy

Optical absorption spectra of the thin film semiconductors in this work were measured using a UV-visible-infrared spectrophotometer (Shimadzu UV-3600 Plus) with an integrating sphere attachment (ISR-603). Monochromatic light illuminated the sample at normal incidence and, by changing the position of the sample on the integrating sphere (see Figure 3.1), the transmitted, T, and diffusely reflected, R, fractions of the incident intensity were recorded. For most samples, the absorption coefficient, α, was calculated using the relation,

$$\alpha = \frac{1}{d}\frac{(1-R)}{T} \ , \tag{41}$$

where d is the thickness of the film. The illumination wavelength was scanned to produce a spectrum.

Alternatively, if the sample is thick and highly scattering, Kubelka-Munk theory [79] can be used to estimate the form of the absorption spectrum using only the diffuse reflectance. Developed for paint coatings which both absorb and scatter light, the model assumes that the film is thick enough such that increasing the thickness would not change the amount of light scattered back out [80]. In this case, the ratio of absorption coefficient, K, to scatter per unit length, S, is related to the diffuse reflectance, R_∞, as follows,

$$\frac{K}{S} = \frac{(1-R_\infty)^2}{2R_\infty} \ . \tag{42}$$

Assuming the scatter does not depend strongly on the wavelength, this function can be used to show the features of the absorption.

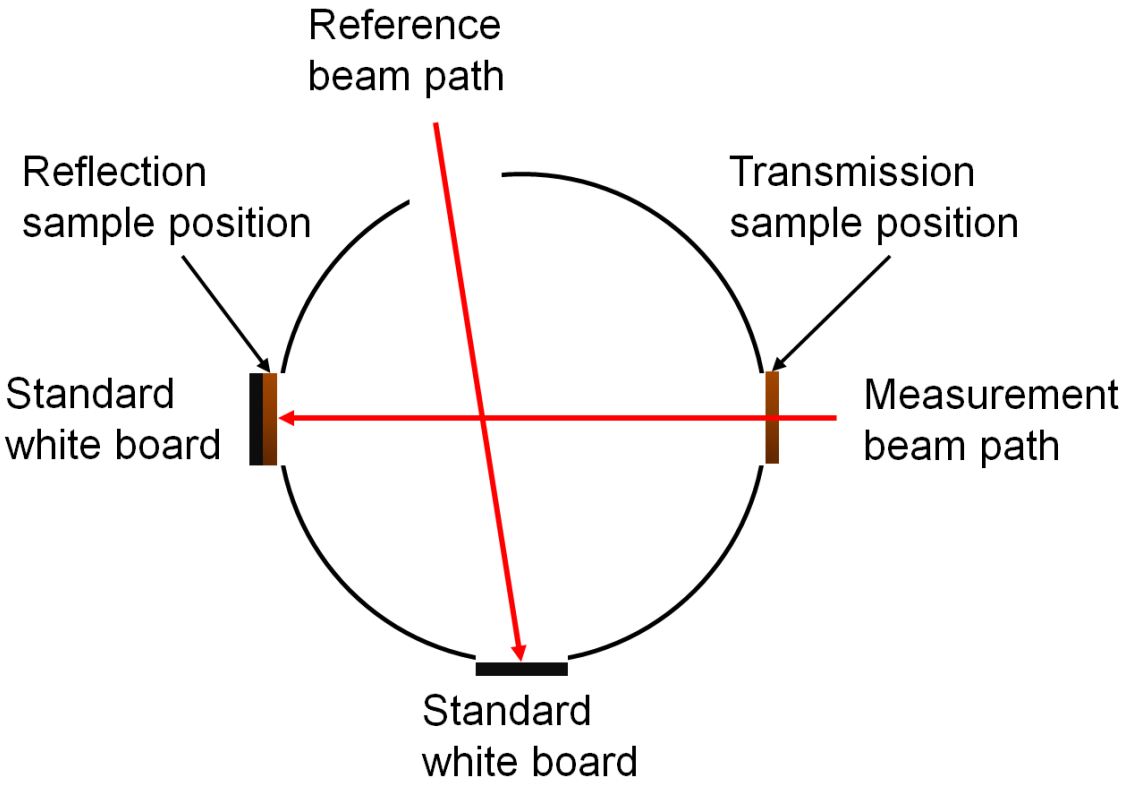

Figure 3.1 Schematic of the integrating sphere set-up, showing the sample positions for transmission and reflection measurements.

3.3.2 Photothermal deflection spectroscopy

Photothermal deflection spectroscopy (PDS) is a technique relying on the generation of heat in the sample upon absorption of light. The absorption spectrum close to the band edge was measured to high sensitivity by immersing the sample in FC-72 Fluorinert ® (3M Company), which is a liquid with a temperature-dependent refractive index. The sample was illuminated with a narrowband beam from a Light Support MKII 100 W Xenon arc lamp passed through a CVI DK240 monochromator. The heat generated by generation, energy loss and non-radiative recombination of charge carriers was detected via the induced temperature gradient and refractive index gradient in the liquid. A Qioptiq 670 nm fibre coupled diode laser with a temperature stabiliser was transmitted through the liquid parallel to the sample (in equilibrium). The refractive index gradient causes the laser to be deflected by an amount proportional to the absorbed intensity. The deflection was measured on a differentially amplified quadrant photodiode and Stanford Research SR830 lock-in amplifier. In order to

build up a spectrum, the incident wavelength is scanned using the monochromator. The PDS measurements involved in this thesis were taken by Dr Aditya Sadhanala (OE).

3.4 Steady state photoluminescence spectroscopy

Photoluminescence (PL) spectra were obtained by exciting the sample using pulsed laser light, the output of a Ti:Sapphire (Spectra Physics Solstice Ace), frequency doubled in a β-barium borate (BBO) crystal and filtered to give a 3.1 eV beam at 10° to normal incidence. The emission was collected in a reflection geometry with a 150 mm focal length, 2 inch diameter lens, filtered to remove the excitation and passed through a spectrograph (Andor Shamrock 303i) to disperse the wavelengths. This was detected with an intensified charge coupled device (iCCD) (Andor iStar DH740 with a Gen 3 intensifier). The quantum efficiency of the Gen 3 intensifier (18x-74) remains flat between 11.0–11.3 % across the spectral region 500 nm–850 nm (1.46–2.47 eV) [81], therefore, no calibration was needed. The wavelength-dependent spectrum was converted into an energy-dependent spectrum using the Jacobian transformation ($I(E) = I(\lambda)d\lambda/dE$). For low temperature measurements, the sample was placed inside an Oxford Instruments cold finger cryostat.

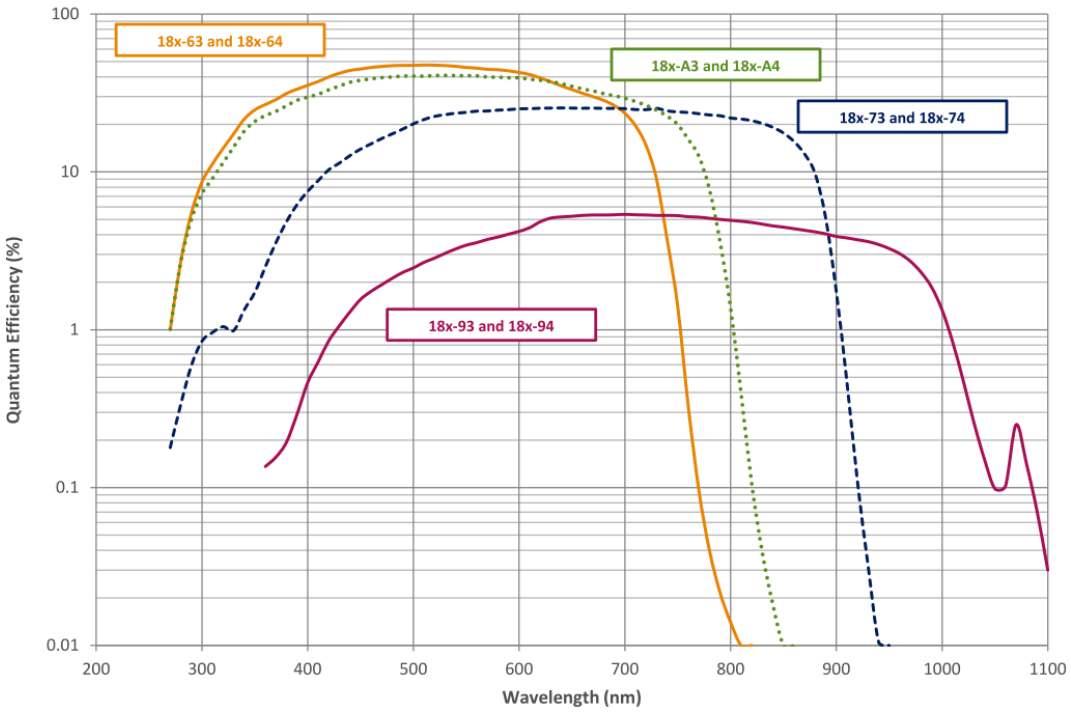

Figure 3.2 Quantum efficiency curves for Andor iStar Gen 3 image intensifiers. The blue curve for 18x-74 is relevant for our system. From Ref. [81].

The PL quantum efficiency (PLQE, ϕ) is defined as the fraction of the photons absorbed which are emitted as PL.

$$\phi = \frac{\#\ \text{photons emitted}}{\#\ \text{photons absorbed}}$$

For PLQE measurements, the sample was mounted inside an integrating sphere (labSphere, 6 inch internal diameter) and excited with a continuous wave 405 nm diode laser (Coherent CUBE). The excitation and PL intensity was averaged over the inner surface of the integrating sphere and collected through a multimode optical fibre, coupled into a spectrometer (Andor Shamrock). The spectrum was detected with a charge coupled device (CCD) camera (Andor iDus). The wavelength response of the whole setup (integrating sphere, fibre, spectrometer and camera) had been previously calibrated using the spectrum of a Xenon arc lamp.

The PLQE was calculated using the method proposed by de Mello *et al*. [82] to account for absorption of the transmitted and scattered excitation light. This method requires three measurements: one with the excitation directed onto the sample in the integrating sphere; another with the excitation laser directed onto the inner wall of the integrating sphere with the sample still inside; and one with the sample removed and the laser again illuminating the inner wall. The measurement with the sample indirectly illuminated provides the fraction of the laser intensity that was transmitted through the sample under direct illumination, which was absorbed after being scattered around the integrating sphere.

3.5 Time-resolved photoluminescence

The time dependence of the PL was with the same setup as described in the previous section, exciting with the frequency-doubled Ti:Sapphire laser at 3.1 eV and detecting with the iCCD. The iCCD functions because incident photons generate electrons at a photocathode detector, a voltage accelerates the electrons through a microchannel plate, which amplifies the electronic signal while maintaining spatial resolution perpendicular to the direction of travel. The electrons are converted back into photons at a phosphor and finally detected with a CCD. The time resolution is achieved by electrically gating the applied accelerating voltage: a digital delay generator allows a voltage pulse to be triggered to coincide with the arrival of

the PL pulse, or after a certain delay, and persist for a controllable time window. The time resolution is determined by the shortest electronic pulse achievable across the channel which is dependent on the amplification or gain applied. In my case, high gains were required so the time resolution was 4 ns.

The technique of time-correlated single-photon counting (TCSPC) provides better time resolution but our setup was limited in excitation fluence and not sensitive enough to detect the emission from my samples due to their low PLQEs.

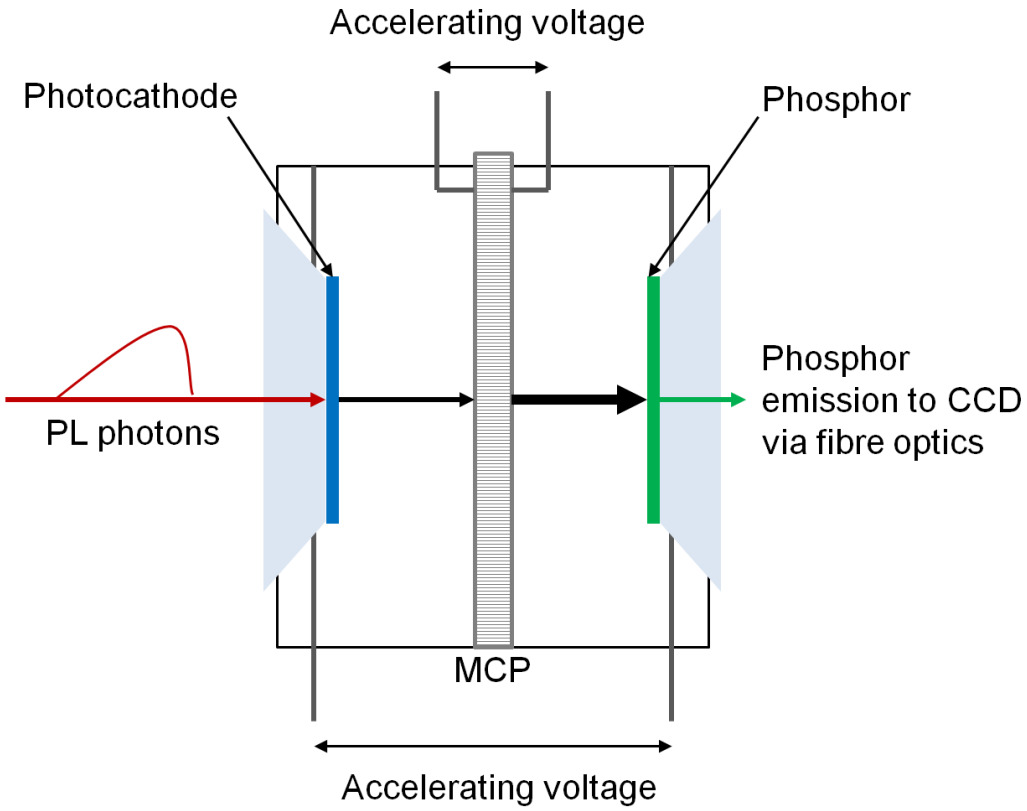

Figure 3.3 Schematic of the internal function of an iCCD. MCP is a microchannel plate. Applying a voltage pulse triggered from the laser and digitally delayed by increasing time increments allows time-resolved PL spectra to be measured.

3.6 Transient absorption

3.6.1 Transient absorption operating principles

Transient absorption is a pump-probe technique, employing two pulses with a variable time delay between them. The first pulse is designed to excite the sample (the 'pump') and the second pulse measures the absorption of the sample (the 'probe'), as shown in Figure 3.4. In this work, a broadband probe is always used, therefore, a transmission spectrum is obtained at each time delay. In order to minimise error due to drift in the probe spectrum over time, the pump is chopped at half the repetition rate to cut out alternate pulses, so that a 'pump-off' measurement may be taken after every 'pump-on'. A 'reference' beam is also used, which is identical to the probe and passes through the sample but does not spatially overlap with the pump pulse, to further reduce any noise due to fluctuations in the probe beam intensity. The transient absorption, or in this case, differential transmission, ΔT/T, is then calculated as:

$$\frac{\Delta T}{T} = \frac{T_{\text{on}}/T_{\text{ref}} - T_{\text{off}}/T_{\text{ref}}}{T_{\text{off}}/T_{\text{ref}}} \ ,$$

where T_{on} is the transmission intensity of the probe with the pump on, T_{off} is the signal with the pump blocked and T_{ref} is the intensity of the reference beam.

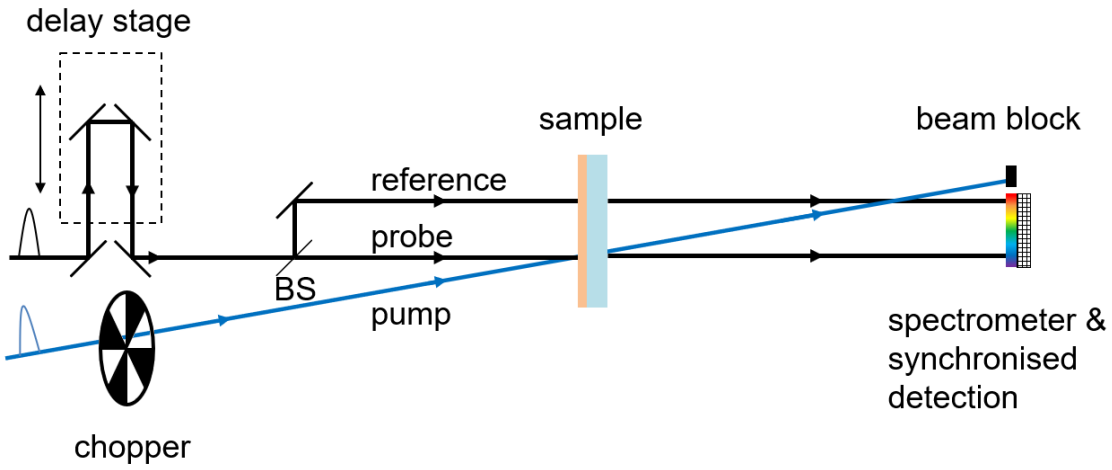

Figure 3.4 Schematic of a typical transient absorption set-up, in transmission. BS is a 50:50 beamsplitter, to produce identical probe and reference beams, which are simultaneously detected on the CCD array at two different heights.

The values of $\Delta T/T$ are typically plotted for all wavelengths and delay times in a 2D map or as spectra at different time slices. The main signal is usually the ground state bleach (GSB) – when the population of the ground state is depleted by the pump, therefore absorption of photons at the band gap energy decreases. This gives rise to a positive $\Delta T/T$. Commonly, there is also a photoinduced absorption (PIA) – whereby new transitions become available due to the increased population in the excited state or shifts in the energy levels of the system. This causes $\Delta T/T$ to be negative. In some cases, it is also possible to stimulate emission from the excited state, which is observed as a positive $\Delta T/T$. Transient absorption is a powerful technique because it can provide information about dark processes and changes in the excited state of the system, regardless of whether it decays radiatively or not.

3.6.2 Experimental details

For my experiments, I used various pump and probe sources depending on the timescales of the processes measured and the wavelength ranges needed. For ultrafast measurements (100 fs – 2 ns) the Ti:Sapphire output (800 nm, 1 kHz repetition rate, 100 fs pulse length) was split to produce both pump and probe beams. The pump was produced either by frequency doubling the fundamental in a BBO crystal or using a home built noncollinear optical parametric amplifier (NOPA) to tune the wavelength through the visible. The required probe was broadband in the visible or UV, so another NOPA was used for the visible region or the supercontinuum from a CaF_2 crystal was used for the UV.

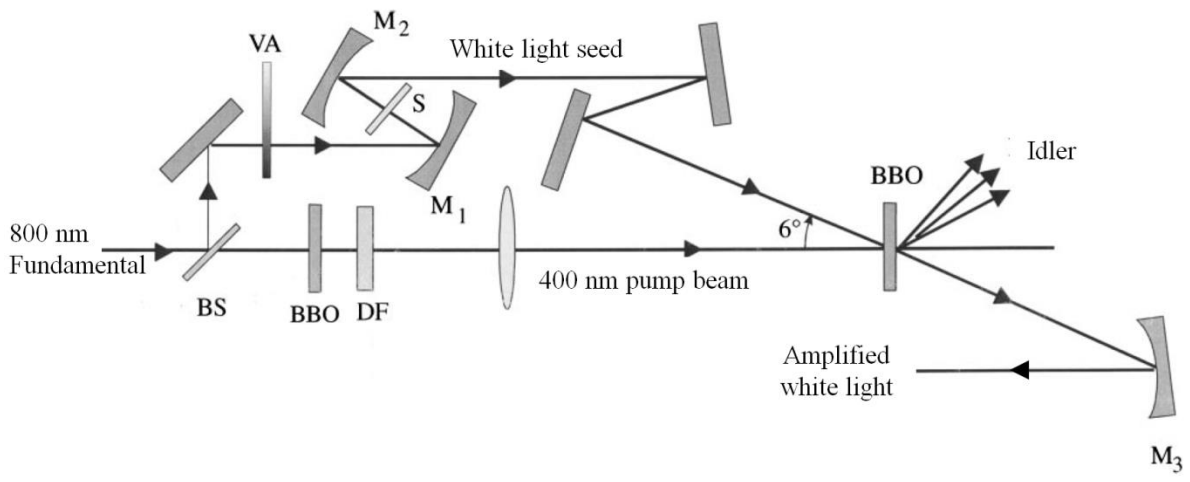

Figure 3.5 Path diagram of a NOPA. BS is a beam splitter, VA is a variable attenuator, S is a 1 mm thick sapphire crystal, DF is a dichroic filter, and M1, M2 and M3 are spherical mirrors. Modified from ref [83].

The purpose of a NOPA is to amplify a broad range of wavelengths from a weak, broadband 'seed' pulse by transferring intensity from a powerful 'pump' pulse in a nonlinear optical process. I will refer to this pump as the 'NOPA pump' to distinguish it from the pump used to excite the sample. Details of the design principles of a NOPA are described by Manzoni *et al*. [84] and the beam path is shown in Figure 3.5. In brief, the 800 nm fundamental beam was split into a small fraction, which was focussed through a sapphire crystal to generate a supercontinuum seed pulse, and a large fraction of the intensity, which was frequency doubled in a BBO to produce a 400 nm pulse for the NOPA pump. Due to the longer pulse duration of the white light seed, the NOPA pump was passed through a 10 cm long quartz rod to stretch the pulse in time. The two pulses were then focused and overlapped in space and time onto a second BBO, with an angle close to 3.7° between them. When the phase matching conditions are met, intensity from the NOPA pump is transferred into a broad range of wavelengths in the seed, allowing these amplified wavelengths to be used as a probe. For the generation of a narrowband pulse for pumping the sample, the NOPA pump pulse was not stretched in quartz and the existing dispersion of the white light seed was exploited, so the amplified wavelengths could be tuned by delaying the NOPA pump relative to the chirped seed pulse.

For ultrafast TA (100 fs – 2 ns delay time), the sample was excited with a pump beam that was modulated with a mechanical chopper at 500 Hz to provide alternate on and off shots, and the pump-probe delay was controlled using a motorised delay stage (Newport).

TA measurements at delays longer than 2 ns were performed using a different pump source: the sample was instead excited with a Q-switched pulsed laser (Advanced Optical Technologies AOT-YVO-25QSPX). The fundamental wavelength is 1064 nm but the second or third harmonic was used by changing an internal module. The pulse duration was specified as 600 ps but in practice only 1 ns temporal resolution could be achieved due to electronic jitter.

For all measurements using a NOPA to generate the broadband probe, the beam was split with a 50:50 beamsplitter to produce the probe beam and an identical reference beam, which were each focused onto the sample at different positions. The pump was overlapped with the probe spot, polarised at 54.7° relative to the probe in order to keep the intensity of the signal independent of dipole orientation [85]. The transmitted probe and reference beams were

collected and detected using an imaging spectrometer (PI acton Spectrapro 2150i) on two vertically-offset InGaAs diode arrays (Hamamatsu S3901256Q). The arrays were driven and read out by a custom made circuit board from Stresing Entwicklungsbüro. The exposure time was 1 s at each pump–probe delay, corresponding to 1000 shots. At least five sweeps of the pump–probe delay were performed sequentially in order to check for changes to the sample over the measurement time, which was at least 15 minutes.

Transient reflection (TR) measurements were set up in the same way except that the reflected probe and reference beams were directed into the spectrometer instead of the transmitted beams.

The pump fluence, F, was determined by measuring the power, P, and diameter, d, of the pump beam at the point of overlap with a CCD beam profilometer (ThorLabs), using the following relation,

$$F = \frac{P}{f\pi(d/2)^2} \ .$$

The average excitation density, n, was then calculated using the absorption of the sample, A at the pump wavelength, λ, and the thickness of the film, t. For samples where the film was not covering the whole area, I included the measured area fraction, $x < 1$ as follows,

$$n = \frac{AF}{xt}\frac{\lambda}{hc}.$$

Considering the Lambert-Beer law absorption profile, the absorbed fraction of the intensity was determined from the absorption coefficient of the material, α, as,

$$A = \frac{1}{\alpha t}(e^{-\alpha t} - 1) + 1 \ .$$

3.7 Raman spectroscopy

Raman spectroscopy probes vibrational modes of a material by measuring the inelastic scattering of photons. When monochromatic light is backscattered from a sample, most of the resulting photons are of the same energy as the incident ones – this is elastic or ‘Rayleigh’ scattering. However, if a phonon is created in the process, the backscattered photon will have

less energy than the incident light (Stokes Raman scattering), or conversely if a phonon is absorbed in the process, the photon will have more (anti-Stokes Raman scattering).

The Raman spectra in this thesis were taken using continuous wave (CW) laser sources at 532 nm (solid state diode laser), 633 nm (Helium Neon line), 785 nm (diode laser) backscattered from the sample through a 100× objective lens and dispersed through a subtractive triple-stage grating (Horiba T64000). Spectra were recorded between 30 cm^{-1} and 400 cm^{-1} using a CCD detector (Horiba Synapse OpenElectrode) which has a monotonically increasing quantum efficiency of between 0.43 and 0.50. The samples were measured at room temperature, in air. These Raman measurements were performed together with Dr Tudor Thomas (OE) or Remington Carey (OE).

3.8 X-ray photoemission spectroscopy

X-ray photoemission spectroscopy was performed on $Cs_2AgBiBr_6$ thin films deposited on indium tin oxide (ITO) coated glass by Dr Robert Hoye. A monochromatic Al $K_{\alpha 1}$ X-ray source ($h\nu$ = 1486.6 eV) was used, with a SPECS PHOIBOS 150 electron energy analyser. The total energy resolution was 0.50 eV. The binding energy was calibrated using a polycrystalline Ag foil placed in electrical contact with the samples, which was also used to avoid charging effects during the measurement. To determine the position of the Fermi level, relative to the valence band maximum, the spectra were then fitted to a calculated density of states using the method reported by Hoye *et al*. [86].

Chapter 4: Origin of long charge carrier lifetimes in silver-bismuth double perovskite

Silver-bismuth double perovskites have recently been investigated as non-toxic alternatives to lead-halide perovskites as absorbers for photovoltaics. However, their indirect band gaps and associated low photoluminescence quantum efficiencies have made evaluating their charge carrier lifetime and recombination mechanisms from photoluminescence measurements challenging. In this work, I use transient absorption spectroscopy to track the dynamics of the whole photoexcited charge carrier population in $Cs_2AgBiBr_6$. I resolve a small initial drop in the ground state bleach on a picosecond timescale, after which the remaining charge carriers decay mono-exponentially with a lifetime of 1.4 μs. The picosecond decay is attributed to carrier thermalisation from the direct transition to the indirect bandgap, and the 1.4 μs lifetime represents the recombination of most photocarriers. I propose that silver-bismuth antisite defects play an important role in the system and suggest that charge transport and extraction can be efficient in $Cs_2AgBiBr_6$ solar cells. In addition, our measurements suggest high levels of carrier-phonon coupling in these materials, which may strongly affect recombination and transport and will therefore need to be taken into account when designing optimised devices.

4.1 Background and motivation

Lead-halide perovskites display remarkable optoelectronic properties, with long charge carrier diffusion lengths >1 μm [1][2], strong optical absorption on the order of 10^5 cm^{-1} [89], and high photoluminescence quantum efficiencies >80% [90]. These properties have led to rapid increases in the efficiency of perovskite solar cells (up to a certified power conversion efficiency of 25.2%) [7] and light emitting diodes (>20% external quantum efficiency) [91] over the last decade. However, the solubility and toxicity of the lead content, and limited air-

stability of many compositions have motivated researchers to find lead-free alternatives [78][86]. A wide range of materials classes have recently been explored computationally and experimentally [86][77]. In evaluating the potential of these new materials for photovoltaics, much of the focus has been on the bandgap, stability, absorption coefficient and phase [86][92][66][93]. However, even in materials which would be suitable under these criteria, the minority-carrier lifetime has been found to limit their potential for use in photovoltaics [94][95]. Those carrier lifetimes that have been measured of bismuth-based alternatives to the perovskites have typically ranged from <0.1 ns to ~10 ns [95][65][73].

However, silver-bismuth halide double perovskites ($Cs_2AgBiBr_6$ and $Cs_2AgBiCl_6$) were found to have exceptionally long lifetimes [69] (Figure 4.1). Time-resolved photoluminescence measurements of single crystals of these materials show a sharp drop (by 0.5 to 2 orders of magnitude) in photoluminescence (PL) intensity within the first few nanoseconds, followed by a long tail in PL decay, out to 200 to 600 ns. Given the improved stability of devices made from these materials over methylammonium lead iodide [69][71], a variety of compositions of double perovskite compounds are now being explored. The large parameter space offered by this family of materials promises wide tunability and potentially new combinations of advantageous properties [96].

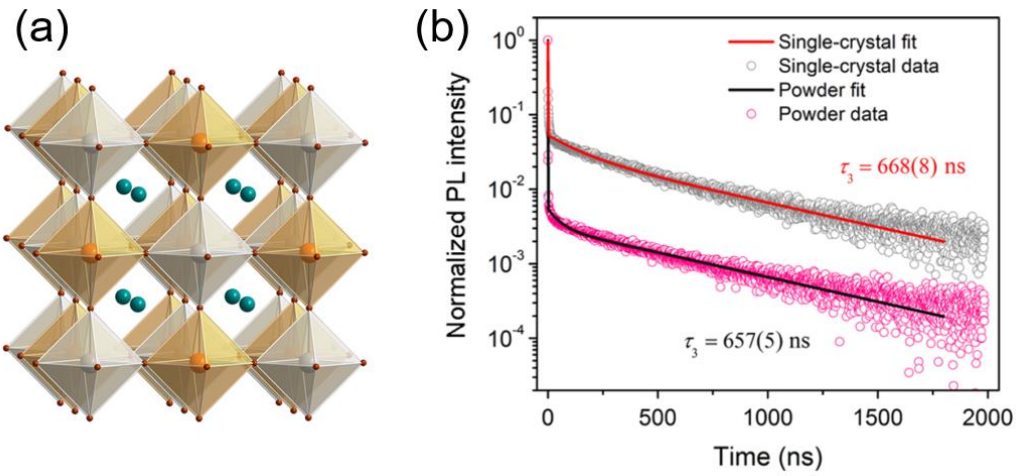

Figure 4.1 (a) Crystal structure of $Cs_2AgBiBr_6$ with green, grey, orange, and red spheres representing nuclear positions of Cs, Ag, Bi, and Br respectively. (b) Time resolved PL decays with triexponential fits showing long lived tail of emission. Both adapted from Ref. [69].

The double perovskite structure allows the Pb^{2+} in lead-halide perovskites to be substituted for less toxic monovalent (e.g., Ag^{+}) and trivalent cations (e.g., Bi^{3+}), while maintaining a

perovskite-type crystallographic structure with 3D connectivity of the bismuth halide octahedra [68][67]. Although the first $Cs_2AgBiBr_6$ solar cells had external quantum efficiencies up to 60% and PCEs of up to 2.43% [71], it remains to be seen whether the steady-state excess carrier density under one sun illumination could support efficient transport to the electrodes in the thicker absorber layers necessary for devices. While mobilities of 1 $cm^2\ V^{-1}\ s^{-1}$ (thin films) and 3 to 12 $cm^2\ V^{-1}\ s^{-1}$ (single crystals) have been reported [97][98], which are comparable to solution processed lead halide perovskite thin films at ~2 $cm^2\ V^{-1}\ s^{-1}$ [99], the photoexcited charge carrier lifetime may limit the achievable steady-state carrier densities and therefore reduce the efficiency of charge extraction. However, the reported PL emission energy for $Cs_2AgBiBr_6$ is often significantly Stokes-shifted below the measured optical bandgap and weak. This calls into question whether the PL lifetimes reported accurately represent the recombination of most photogenerated carriers. The PL measurements have been supported by time-resolved microwave conductance measurements which have also shown a large initial drop in signal, particularly in thin films, which was attributed to surface recombination [98].

In this work, I perform steady state and ultrafast time-resolved spectroscopy on $Cs_2AgBiBr_6$ thin films, with comparison to single crystals. Through an understanding of the mechanism of PL decay as well as the non-radiative recombination of charge carriers, I can determine whether this material has the potential to make more efficient devices.

4.2 Nature and lifetime of $Cs_2AgBiBr_6$ excited state

4.2.1 Thin film $Cs_2AgBiBr_6$ electronic states characterised by steady state absorption and photoluminescence spectroscopy

Thin films of $Cs_2AgBiBr_6$ were synthesised by Dr Robert Hoye (Faculty of Engineering, Department of Materials, Imperial College London) following a previously reported spin-coating method [71], with 5 min annealing at 250 °C inside a nitrogen-filled glovebox and powder XRD measurements showed that they had a phase-purity of 99.75%. The thickness of the film studied here was 520 nm, as measured by Dektak profilometry. The absorption properties of the film were characterised by photothermal deflection spectroscopy (PDS) (Figure 4.2) and UV–visible spectrophotometry (Figure 4.3).

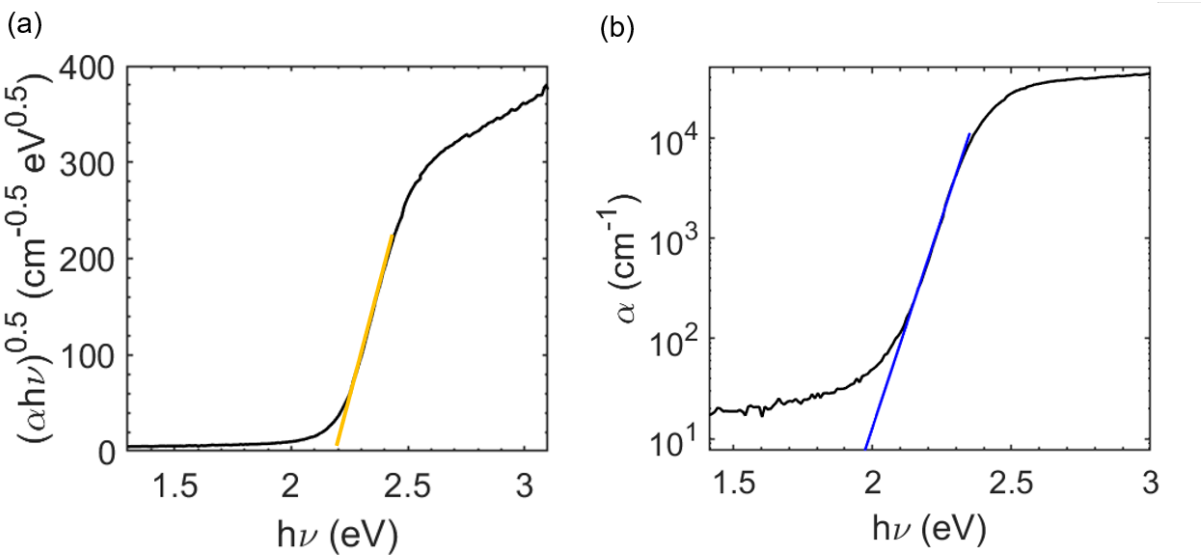

Figure 4.2 (a) Tauc plot for a thin film of $Cs_2AgBiBr_6$ with linear fit for the indirect bandgap, which occurs at 2.2 eV. (b) Semilogarithmic plot of absorption coefficient of the same film with a fit to extract the Urbach energy of 52 meV. Both data sets are the steady state absorption measured using PDS by Dr Aditya Sadhanala.

In order to determine the band gap energy for this indirect material, a Tauc analysis of the absorption edge measured by PDS was performed [100]. By plotting $(\alpha h\nu)^{0.5}$ against energy, as appropriate for an indirect semiconductor, the band gap could be found by using a linear fit to the rising edge, and extrapolating to the point at $\alpha = 0$ (Figure 4.2(a)). This yielded an indirect band gap of 2.2 eV. By fitting the exponential function given in Equation 19 to the same PDS data (plotted logarithmically in Figure 4.2(b)), an Urbach energy of 52 meV was extracted.

PL measurements were taken by exciting the sample with a 3.1 eV pulsed laser source and detecting with an iCCD. The PL spectrum is centred at 1.9 eV and significantly inhomogeneously broadened (Figure 4.3). The iCCD has a constant quantum efficiency between 1.46–2.47 eV so no calibration was performed, other than careful characterisation and subtraction of the background light. Integrating sphere experiments were performed by Robert Hoye, giving a PLQE of 0.01% at an excitation intensity of 500 mW cm^{-2}, and 0.02% at 1500 mW cm^{-2}. These low efficiencies indicate a high proportion of Shockley-Read-Hall recombination, which, if faster than carrier extraction, will be detrimental to device performance. The large Stokes shift and broadening of the PL peak could be caused by phonons, self-trapped excitons or radiative recombination to defects.

4.2.1 Thin film Cs2AgBiBr6 electronic states characterised by steady state absorption and photoluminescence spectroscopy

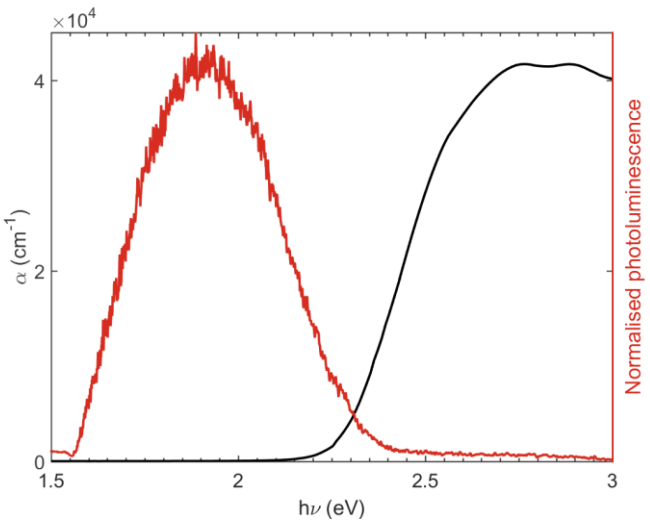

Figure 4.3 Thin film $Cs_2AgBiBr_6$ absorption coefficient – below 2.4 e V from PDS and above 2.4 eV from UV-visible transmission and reflectivity measurements performed by Dr Robert Hoye. PL spectrum using 3.1 eV excitation at room temperature.

The most likely explanation for all of these observations would be the presence of sub-bandgap defect states that are involved in emissive recombination. The low absorption edge slope in the PDS spectrum implies some energetic disorder which may be due to Ag_{Bi} anti-site defects, or Ag or Cs vacancies [101]. This hypothesis is supported by previous observations that annealing $Cs_2AgBiBr_6$ single crystals to reduce the trap density leads to a blue-shift in the PL, closer to the optical gap [97]. If we consider that sub-bandgap absorption in $Cs_2AgBiBr_6$ films could also be due to phonon absorption and emission, the phonon energies that would account for this are much larger than the typical optical phonon energies in this material (~10 meV), in agreement with observations of sub-gap PL peaks by Filip *et al.*[102].

The PL broadening mechanism was further investigated using the temperature dependence of the PL spectra (Figure 4.4). At low temperatures, the PL emission is more intense and the peaks decrease in width. The increase in intensity shows that this emission cannot be due to phonon-assisted recombination across the indirect band gap. The linewidths extracted by fitting a Gaussian peak to each spectrum as well as those obtained from the raw data are presented in Table 1. The fitted values may be less sensitive to noise in the spectra however, they may not capture the asymmetry of the peaks which causes them to deviate from a purely Gaussian shape. The apparent broadening on the low energy side of the peak could be due to radiative recombination *via* an increased number of phonon emission processes at higher

temperatures. However, when the absolute PL intensities are compared, a more likely scenario would be that at high temperatures, the emission from higher energy states are more strongly quenched due to a thermally activated, non-radiative recombination route. As the peak is still significantly inhomogeneously broadened at 50 K, this would support radiative recombination to sub-gap states caused by defects in the film.

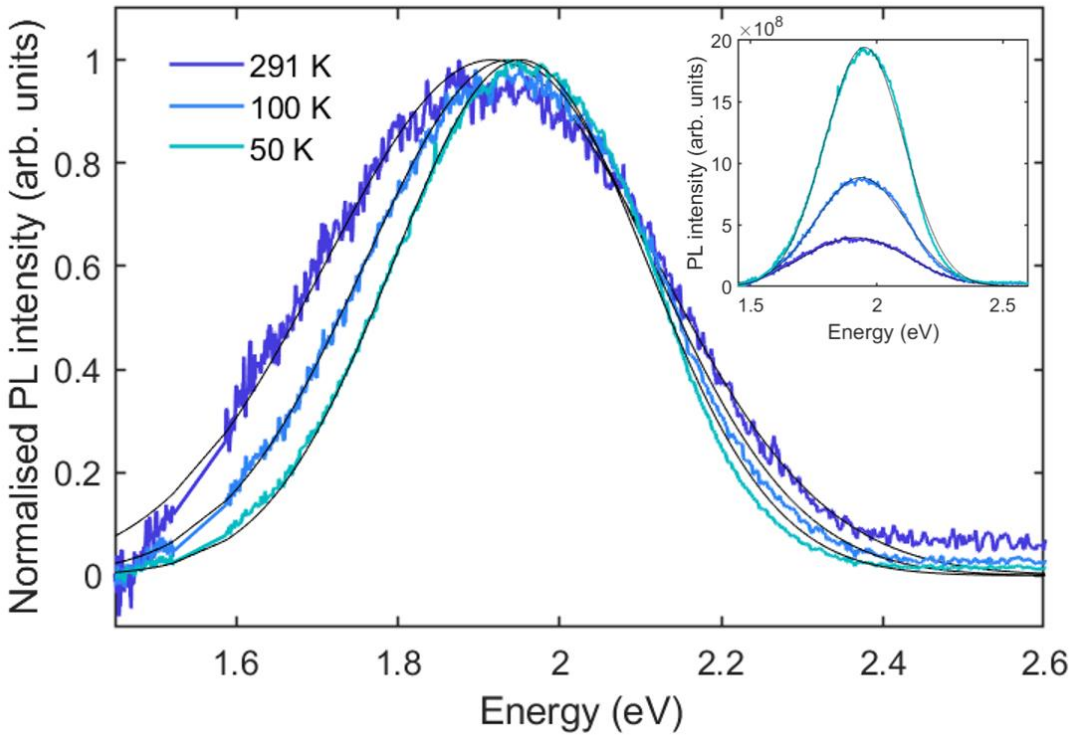

Figure 4.4 Normalised PL spectra taken at 50 K, 100 K, 291 K with Gaussian. All were pumped with 3.1 eV pulses at a fluence of 1 mJ cm^{-2}. Measurements taken together with Robert Hoye.

Table 1 Linewidths of low temperature PL spectra extracted from a Gaussian fit and by taking the FWHM of the raw data.

Method	**Linewidth at 50 K (meV)**	**Linewidth at 100 K (meV)**	**Linewidth at 291 K (meV)**
Gaussian fit	370	420	480
Raw FWHM	360	410	480

4.2.2 Lifetime of the excited state in transient absorption

Transient absorption was performed on the $Cs_2AgBiBr_6$ thin film in order to observe the non-radiatively decaying states. The long-time (>1 ns) spectra were measured by exciting with the third harmonic of an electrically delayed Nd:YVO_4 pulsed laser (3.5 eV, 1 ns pulse width) and probing with a broadband visible pulse (100 fs). The differential transmission of the probe at various times after the excitation is shown in Figure 4.5. All spectra exhibit a positive signal, or ground state bleach (GSB) at probe energies ≥2.3 eV. The GSB is caused by a blocking of transitions by the population of charge carriers which have been excited across the bandgap. We also observe a negative signal, or photoinduced absorption (PIA) at energies <2.3 eV, which becomes most prominent after 100 ns. A sub-bandgap PIA may arise due to a variety of processes which effectively create states within the gap, such as, bandgap renormalisation, localisation of carriers by distortion of the lattice (i.e. polarons or self-trapped excitons) or carriers occupying shallow trap states. In order to find the most likely origin, it is helpful to look at the time dependence and fluence dependence of each signal region. Bandgap renormalisation can already be excluded because this effect can only be observed before carriers have cooled, on <1 ns timescales.

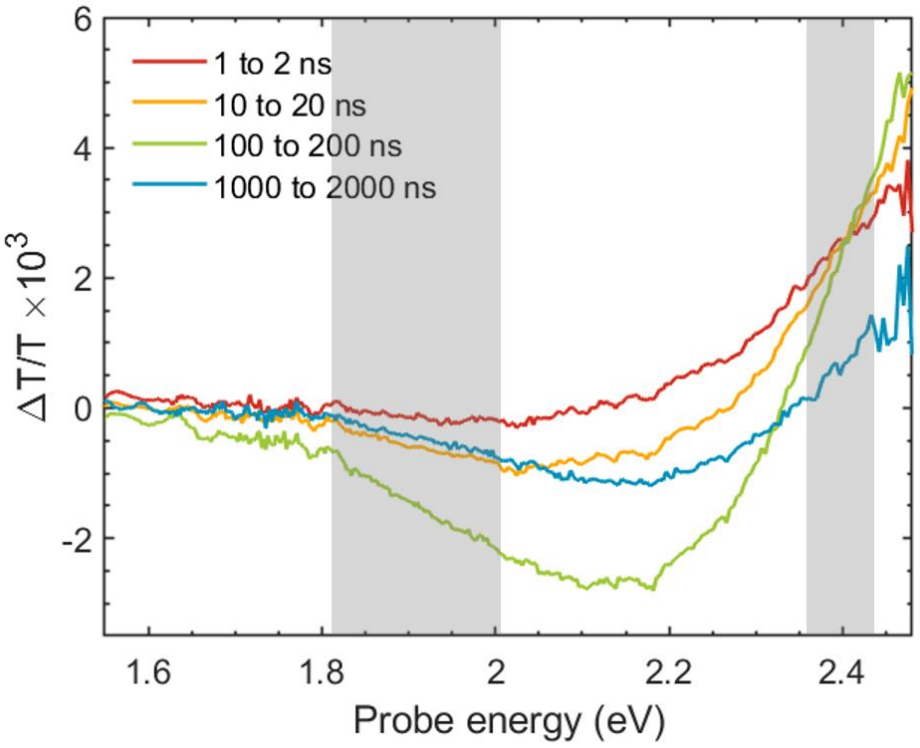

Figure 4.5 Transient absorption spectra of $Cs_2AgBiBr_6$, averaged between the time ranges given in the legend (approximately ten time points), using a 3.5 eV, nanosecond pump source. Grey shaded regions were integrated to produce the kinetics in the following figure.

The rate of decay of the ground state bleach, integrated between 2.36 eV and 2.43 eV for the long-time measurements, was found to be independent of fluence (Figure 4.6). The kinetics could be fitted with a mono-exponential function, which is indicative of Shockley-Read-Hall recombination, and a time constant of 1.4 µs was extracted. This is longer than the previously reported carrier lifetimes inferred from PL decays. The PIA (1.82–2.07 eV) also decayed monoexponentially after 1.4 µs (Figure 4.6), which further supports the slow decay of the overall charge carrier population, including the mid-gap states. Remarkably, the PIA increases in magnitude for 200 ns after excitation. Therefore, there must be a slow process generating the mid-gap states without significant loss of carriers as represented by the GSB. This was studied further by comparison to the PL lifetime.

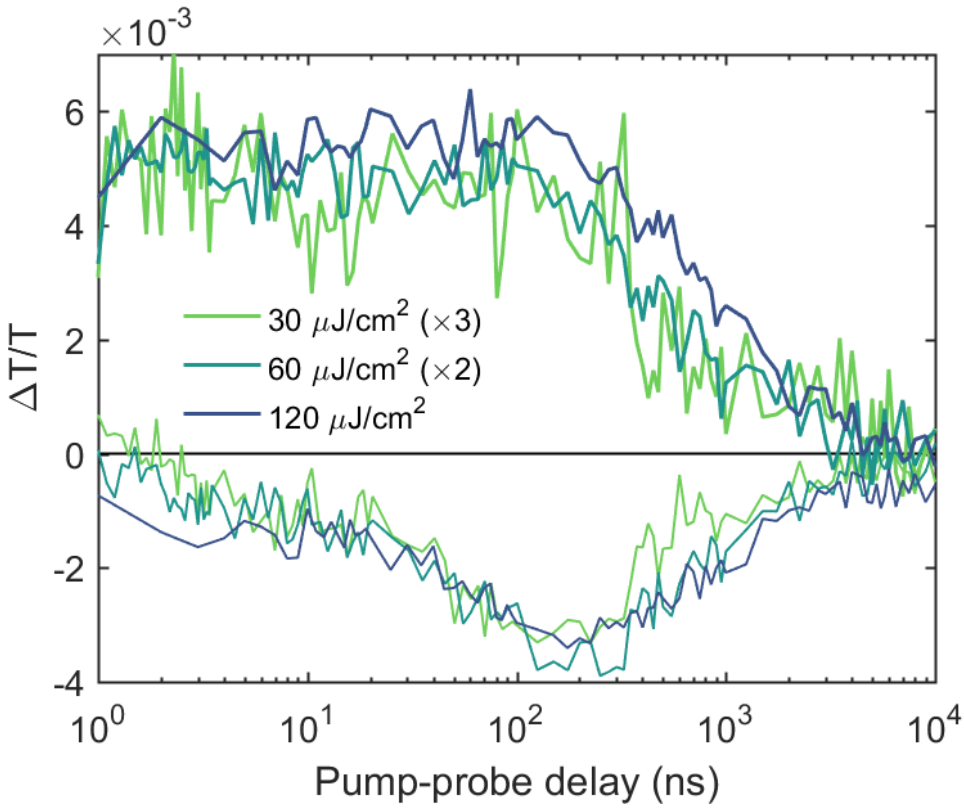

Figure 4.6 TA kinetics of the GSB (integrated positive signal at probe energies of 2.36-2.43 eV, bold lines) and PIA (integrated negative signal at 1.82–2.07 eV, fine lines) signals taken with three different pump fluences, multiplied by appropriate factors in order to compare the rise time and decays.

4.2.3 Comparison of PL decay with TA signals

We performed time-resolved PL measurements in order to compare the decay on the same timescale as the long-time transient absorption measurements. In Figure 4.7, the clear difference between the PL and GSB decays shows that the decay of the PL (shown diagrammatically in Step 3, Figure 4.9) is not caused by the same recombination pathway than that mainly responsible for the slow decay of the overall charge carrier population (Step 3_{nr} & 4_{nr}, Figure 4.9). After ~100 ns, the radiative pathway is reduced to an undetectable level, restricting the remaining charge carriers to recombine non-radiatively. Radiative recombination *via* defect states within the bandgap is supported by the large Stokes shift of the PL.

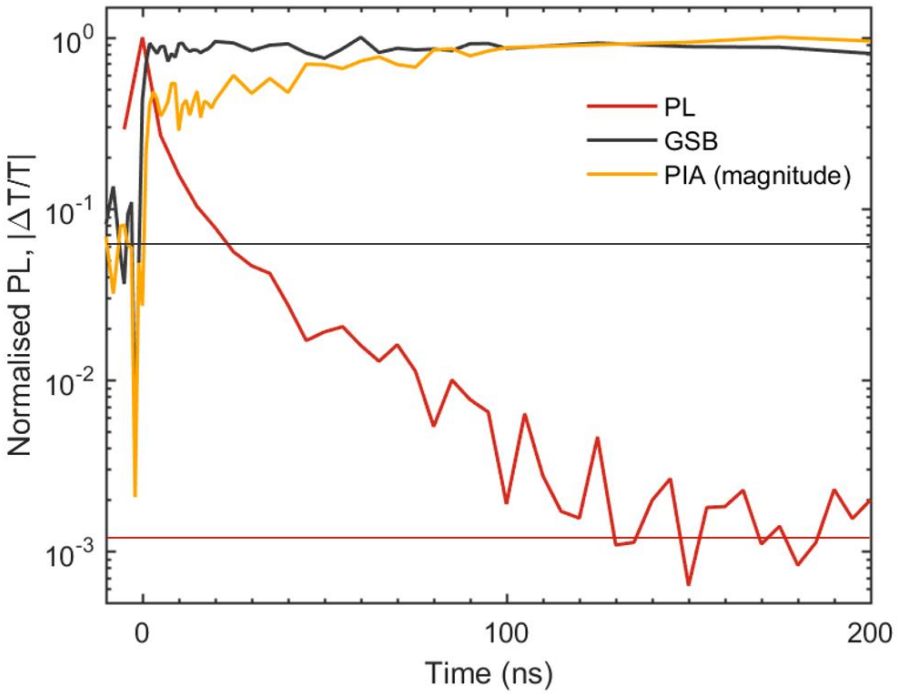

Figure 4.7 Normalised kinetics of the signals in PL and TA: (red) PL decay at 1.9 eV, measured using an iCCD by Robert Hoye, (grey) GSB between 2.36–2.43 eV, and (yellow) PIA between 1.8–2.10 eV. The horizontal lines indicate the noise floor for the TA (grey) and PL (red) measurements.

Point defects produce states which are spatially localised and therefore have a poorly-defined momentum according to the uncertainty principle [10], thereby allowing optical transitions from carriers with any momentum without the need to involve phonons. As such, I have drawn a horizontal defect level, close to the valence band because of evidence from X-ray photoemission spectra (XPS) (Figure 4.8). By fitting the density of valence band states, as calculated by McClure *et al*. [70], to the XPS data, we determined the valence band

maximum to be 0.1 eV below the Fermi level. This means that intrinsic acceptor defects are present, such as Bi_{Ag} antisites, Ag vacancies, or Cs vacancies, making the material p-type. However, the energy of the defect level responsible for non-radiative recombination is unknown.

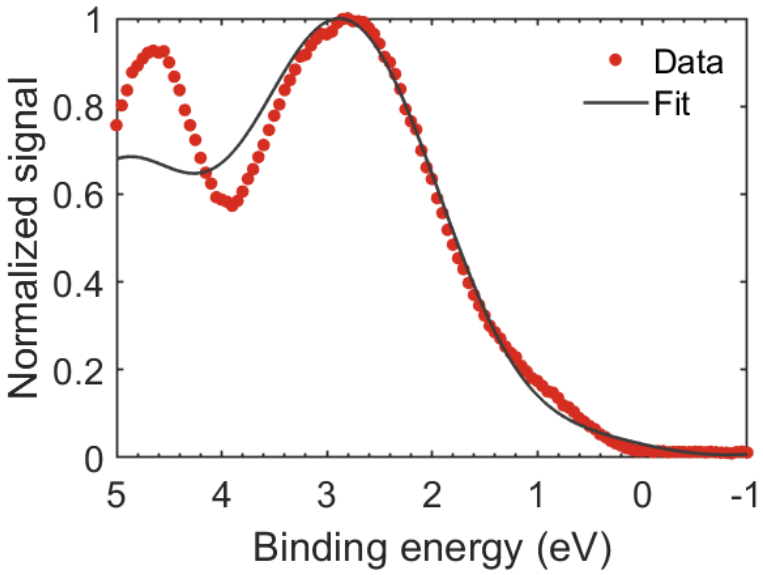

Figure 4.8 X-ray photoemission spectrum (red points) with fitted valence band density of states (black line) for thin film $Cs_2AgBiBr_6$. XPS data taken by Dr Robert Hoye and DOS from calculations in Ref. [70].

The PL decay time in the thin film also coincides with the rise in the magnitude of the PIA signal from 5 to 120 ns (Figure 4.7). This suggests that the same process is responsible for radiative recombination and for filling previously unoccupied mid-gap states, which then give rise to the photoinduced absorption (the inverse process of Step 3). Once the states become saturated they block further radiative recombination until made vacant again. At longer times, the decay of the PIA matches that of the GSB, which implies that the occupation of the defect states then decays on the same timescale as the overall carrier population (Step 4), which continues to decay non-radiatively until the ground state is restored. In theory, Step 4 should also be detectable as a slow decay in the PL, however, our instrument was not sensitive enough to measure this tail.

This has the important implication that the concentration of the acceptor defects is low enough to support significant carrier populations in the film, as the limiting recombination pathway is non-radiative, *via* a different type of defect.

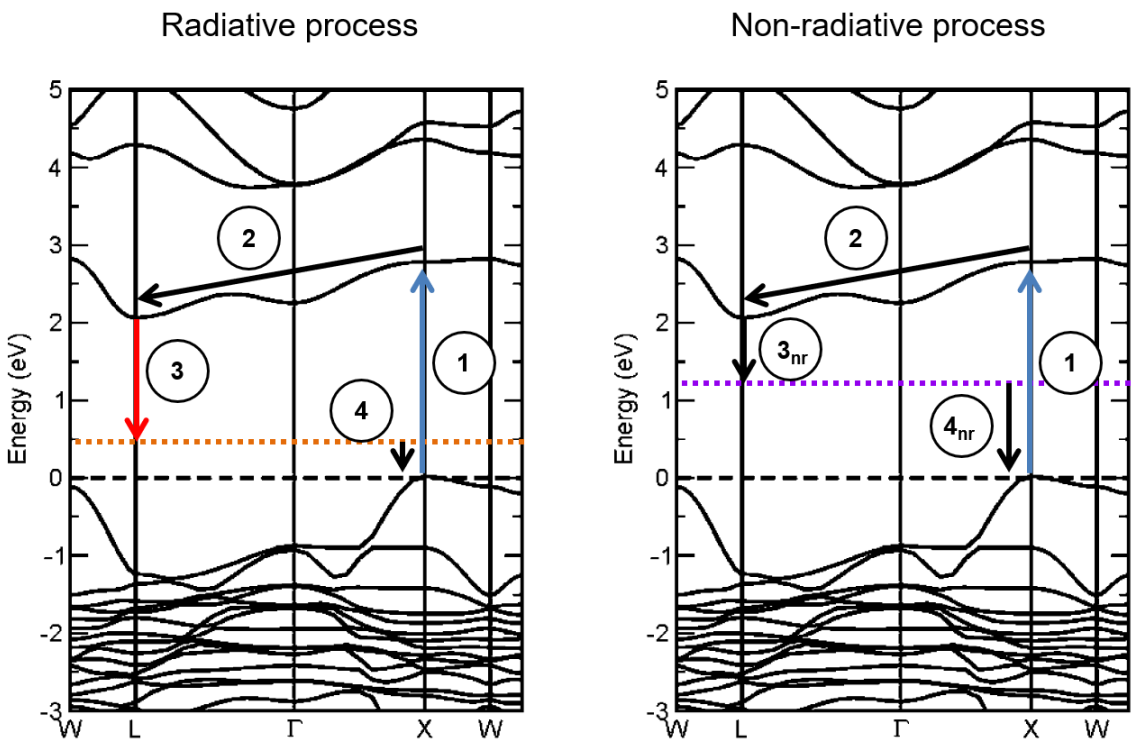

Figure 4.9 Modified from ref. [70]. Calculated band structure by McClure *et al.* with proposed radiative and non-radiative recombination schemes. On the left, the acceptor defect energy level is shown in orange close to the valence band, initially being unoccupied by an electron. On the right a different defect level is shown in purple. Step 1 is photoexcitation of electrons from the valence band to the conduction band *via* any direct transition. Step 2 is cooling to the band edges (not resolved in the measurements discussed so far). Step 3 is radiative decay of electrons into a defect state. Step 4 is recovering the ground state. On the right, Steps 3 and 4 are modified to Step 3_{nr} and Step 4_{nr}, which are not mediated by photons that we could detect using our systems.

4.3 $Cs_2AgBiBr_6$ carrier-phonon interactions

4.3.1 Charge carrier relaxation dynamics before 1 ns

Ultrafast transient absorption spectroscopy provides further insight into the early time charge carrier dynamics. Pumping the film with frequency doubled Ti:Sapphire laser pulses (3.1 eV, 500 Hz, 100 fs), and using the same probe pulses as previously, the resulting $\Delta T/T$ spectrum is plotted in Figure 4.10. On these short timescales, no PIA could be observed, only a GSB tail extending to lower energies.

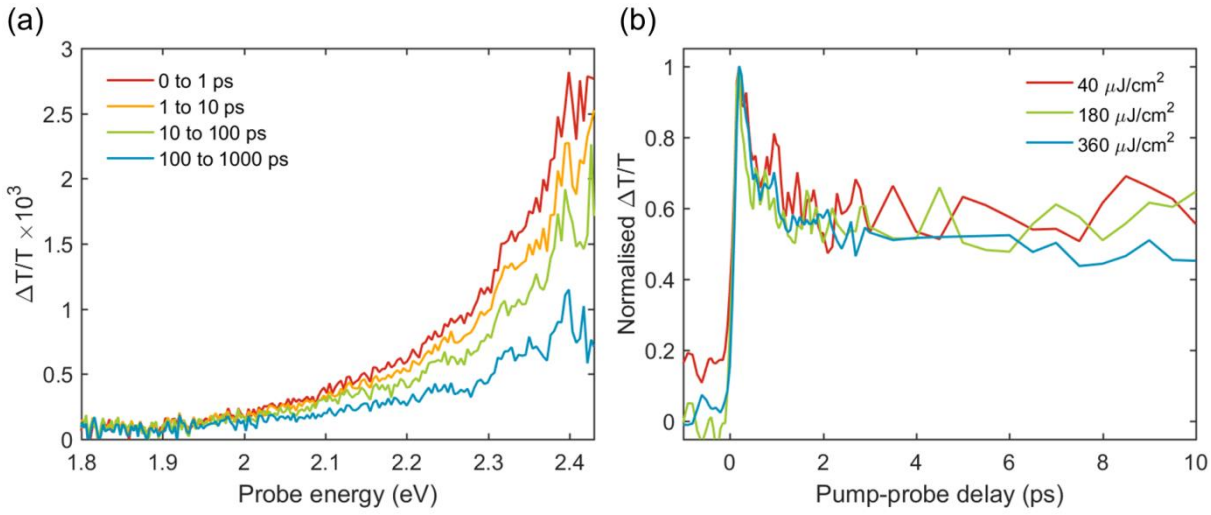

Figure 4.10 (a) Ultrafast TA spectra using a 3.1 eV pump at 180 μJ cm^{-2} (b) TA kinetics of the GSB integrated between 2.36–2.43 eV at various fluences.

During the first picosecond, the GSB signal was observed to decrease by ~50%. This was reproduced when using various fluences to pump the film. Such a loss of signal could either correspond to a loss of carrier population, for example, *via* Auger recombination, or alternatively a migration of the carriers to a part of the band with a lower joint density of states (JDOS). In an indirect bandgap material, when pumped high into the band, charge carriers would be expected to thermalize quickly to the band extrema after excitation. With holes at the X valley and electrons at the L-point, the carriers have become separated in k-space, therefore the populations of holes and electrons cannot bleach the same direct transitions simultaneously. This should not translate into loss of efficiency in a device, and is consistent with the reported EQEs of up to 60% [71], which would not be possible with a 50% loss of carriers in the first picosecond after excitation. Therefore, we can neglect non-

radiative recombination in the first picosecond, and instead observe the thermalisation of charge carriers to separate regions of *k*-space.

4.3.2 Electron-phonon coupling observed in vibrational coherence

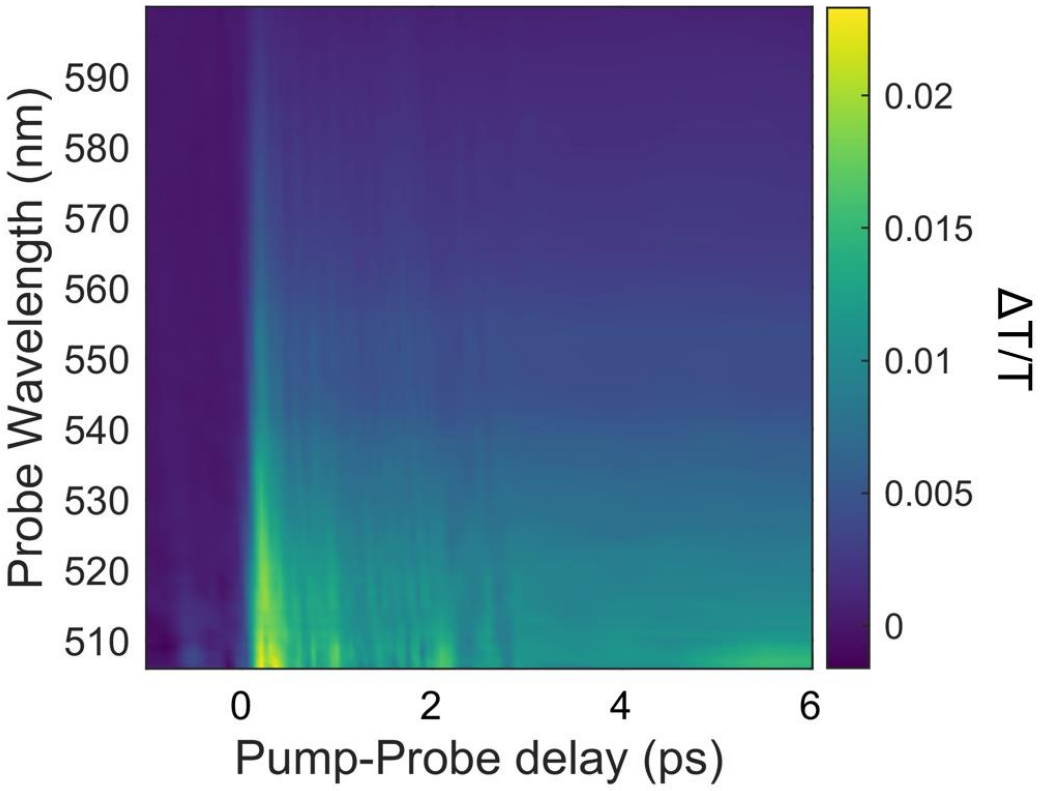

Figure 4.11 Ultrafast TA spectra using a 3.1 eV pump at 360 μJ cm^{-2} . Oscillations of the GSB with a period of ~200 fs may be observed at all energies.

The appearance of oscillations in the whole GSB signal at early times (<3 ps) indicated that the ultrafast TA data may be suitable for vibrational spectroscopy (Figure 4.11). Coherent oscillations were extracted from the early time TA kinetics, by taking the time trace at each measured value of the probe energy and subtracting the monotonically decaying component (found by fitting a triexponential decay). The residual oscillating component was then analysed with a Fourier transform (FT) and the power spectrum is shown in Figure 4.12. The frequency of the oscillations, ν, is expressed in wavenumbers, $1/\lambda$, according to the relation $1/\lambda = \nu/c$, where c is the speed of light in a vacuum. The wavenumber resolution is determined by the length of the time window that was used for the FT, which was 6 ps here.

Therefore, the minimum wavenumber that can be resolved is 5.6 cm^{-1}. The main source of noise is random fluctuations in $\Delta T/T$ signal due to shot-to-shot noise, which can only be reduced by averaging over more shots.

Two peaks can be distinguished above the noise level, at 80 cm^{-1} and 175 cm^{-1}. These are close in frequency to the Raman modes of the material, both when measured resonantly and below the bandgap, using lines at 1.96 eV and 1.58 eV, respectively (Figure 4.12). Therefore, TA should be measured with a sub-bandgap pump in order to find out whether the ground state or excited state is coupled to the phonon.

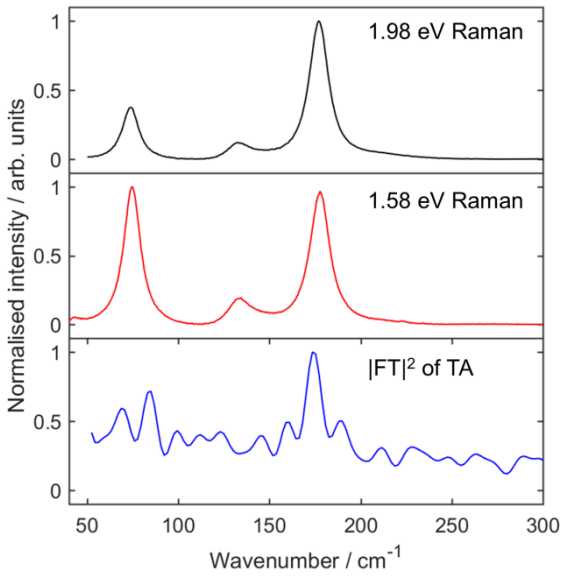

Figure 4.12 Raman spectra and Fourier transform of TA kinetics. The Raman spectra were taken using a 1.98 eV and 1.58 eV laser line to probe resonantly and non-resonantly, respectively. This data was taken together with Tudor Thomas.

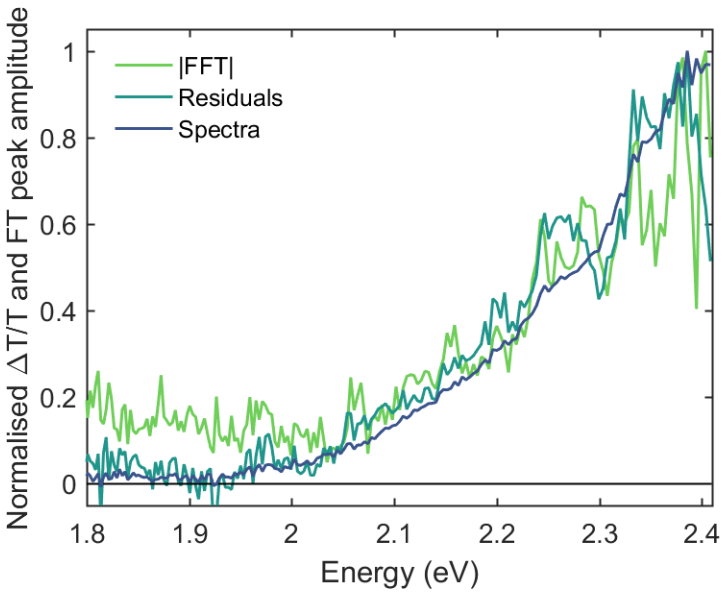

Figure 4.13 Probe energy-dependence of the FT spectrum peak amplitude at 175 cm^{-1}, compared to the amplitude of the oscillating residuals and the original $\Delta T/T$ spectrum, all integrated between 160-190 cm^{-1}.

The amplitude of the 175 cm^{-1} peak, as well as the amplitude of the residual oscillations, were found to track the magnitude of the GSB signal at each probe energy (Figure 4.13). The correlation between $\Delta T/T$, which is proportional to carrier density, and oscillation amplitude suggests that the excited carriers are strongly coupled to the phonon modes detected. This finding is consistent with observations of higher harmonics in the Raman spectra of these materials, as measured by Steele et al. [103]. A higher resolution measurement with more averaging to reduce the noise should be performed to determine whether all the Raman active modes are involved and thereby distinguish between an impulsive stimulated Raman mechanism or an impulsive absorption mechanism for the generation of the coherent phonons. Further investigation of this behaviour will be presented in following chapters.

4.4 Conclusions and further work

In summary, we have used transient absorption spectroscopy to show that the charge carrier lifetime in a spin-coated $Cs_2AgBiBr_6$ thin film is 1.4 µs — significantly longer than its PL decay. Thus, there is potential for long diffusion lengths allowing for thicker active layers of $Cs_2AgBiBr_6$ in devices. The enhanced light absorption in thicker films of this indirect bandgap material would increase current density and power conversion efficiency.

This work also helps to uncover the recombination mechanism of silver-bismuth double perovskites. The weak, red-shifted PL, which decays two orders of magnitude faster than the ground state bleach, is likely due to recombination *via* sub-gap states rather than phonon-assisted indirect band-to-band recombination. We also find that the decay in PL matches the creation of sub-gap states, visible in TA, that then live as long as the overall charge carrier population. This opens up questions on the role of defects, their interactions with carriers, and their effect on the photoexcited carrier decay rates. Further understanding of these phenomena could lead to improvements in this class of lead-free perovskites.

We also find that electron–phonon interactions occur on the picosecond timescale, both allowing carriers to migrate to the band extrema in the first picosecond after excitation, and initiating coherent phonon oscillations observed in transient absorption. The modulation of the ground state bleach indicates strong electron-phonon coupling.

Further research into this relatively new material should aim to resolve inconsistencies in the literature of such fundamental properties as the steady state absorption at room temperature — with some groups observing distinct excitonic peaks and some not [102][104][69]. This would necessitate a broad review of structural characterisation and possible defects or contaminants in materials made by different groups.

Furthermore, the degree of localisation of carriers, both spatially and in k-space, would be interesting to discover as the separation of charge carrier populations could help explain the long lifetimes we have observed. Additional investigation into the effect of carrier-phonon coupling may also yield important insights into the fundamental charge relaxation dynamics and transport properties, not only in these materials but also in a variety of perovskite systems.

More generally, double perovskites have large parameter space to explore and promise to vastly increase our understanding of fundamental interactions occurring in other related semiconductors, allowing us to tailor them to maximum advantage in devices.

Chapter 5: Relaxation pathway and lattice interactions of excitations in bismuth (III) iodide

The work in this chapter aims to investigate the photoexcited states in the most basic octahedrally-coordinated bismuth halide system — bismuth (III) iodide. Using temperature-dependent photoluminescence spectroscopy, I will study the recombination of excitons in the material. The luminescence cannot be explained purely by a simple thermally-activated quenching model, therefore I propose an additional quenching effect of certain phonon modes which couple to the exciton. Ultrafast transient reflection and absorption were used to determine the fundamental lifetime of the excited states, and measured vibrational coherences to characterise their interaction with phonons. The interpretations in this chapter have been aided by theoretical calculations by Ivona Bravić.

5.1 Introduction to bismuth (III) iodide

Bismuth iodide is one of the semiconductors experiencing a resurgence of research interest due to its solution processability into thin films. While large single crystals have been investigated for use in gamma ray, X-ray and alpha radiation detectors [105][75], solution processed thin films have been identified as a possible candidate for photovoltaic applications, because of bismuth iodide's indirect band gap of ~1.7 eV, high absorption coefficient of $>10^5$ cm^{-1} above 2 eV [72] and photoluminescence lifetimes on the order of nanoseconds [73]. In 2016, Hamdeh *et al*. fabricated solar cells from solution processed thin films with a champion power conversion efficiency (PCE) of 1.0 % [74]. Further device studies have not yielded significant increases in PCE but have shown stability over 660 days [106]. Limitations to device performance include low carrier mobilities, especially for holes [105]. Furthermore, recent calculations and atomic-resolution imaging studies have predicted

the existence of mid-gap states caused by bismuth vacancy defects which may provide a stumbling block to achieving high efficiencies in 'messy' solution processed devices [107].

The crystal structure of BiI_3 is rhombohedral, space group $R\bar{3}$, and consists of layers of I-Bi-I atomic planes, held together by van der Waals interactions (Figure 5.1). This structure gives rise to highly anisotropic optical properties, when measured perpendicular or parallel to the planes [108]. From normal reflection spectra along the c-axis, direct excitons with a binding energy of 161–180 meV were observed in absorption, corresponding to a Bohr radius (6.1 Å) smaller than one layer of bismuth iodide octahedra (6.9 Å) [109]. Such tightly bound excitons will not readily dissociate at room temperature, leading to losses during charge separation in devices. The band gap shifts to higher energies as the temperature is decreased from 305 K to 77 K and, at 4 K, a series of sub-gap excitons appear, which were assigned to stacking faults (Figure 5.2) [109].

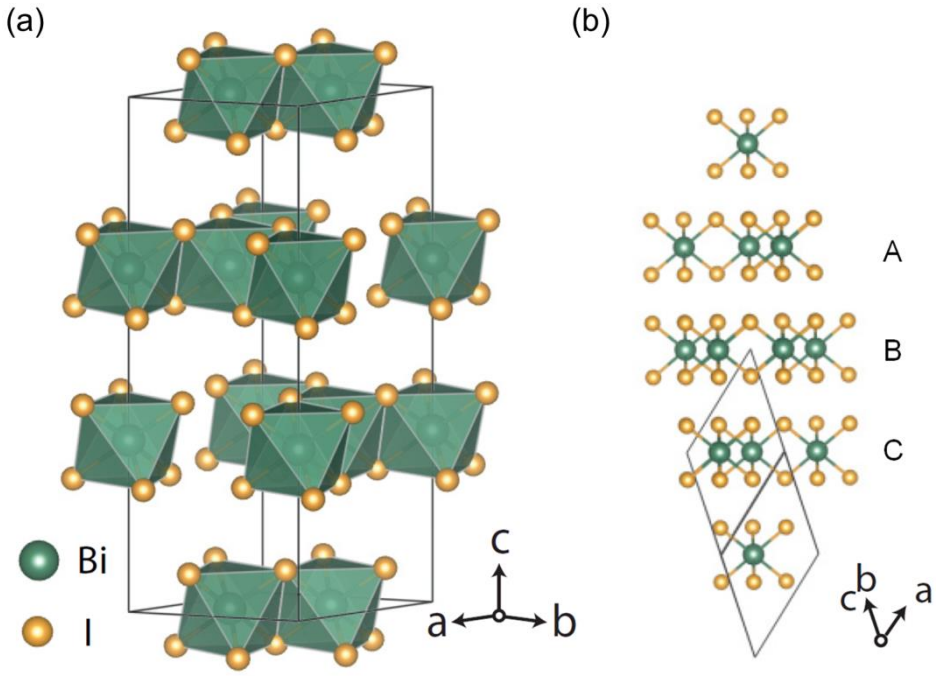

Figure 5.1 Modified from ref [107]. (a) Crystal structure of BiI_3 showing the octahedrally coordinated Bi sites and conventional unit cell spanning 3 layers. (b) 2 x 2 x 2 primitive cells showing the ABC stacking of the layers.

Phonons have been identified to have a profound effect on the optoelectronic properties of BiI_3, not only by allowing indirect optical transitions [109] but also by coherently modulating the excitonic signal in ultrafast transient absorption [110]. This allowed time-domain vibrational spectroscopy to be performed in a simple TA geometry, although the TA study on

BiI_3 by Scholz *et al*. was limited in terms of excitation energy and fluence. Therefore, the degree of exciton-phonon coupling and effect on device performance remains unclear. This work aims to determine the effect of different phonon modes on the electronic states which are relevant for photovoltaic devices, mainly the direct exciton.

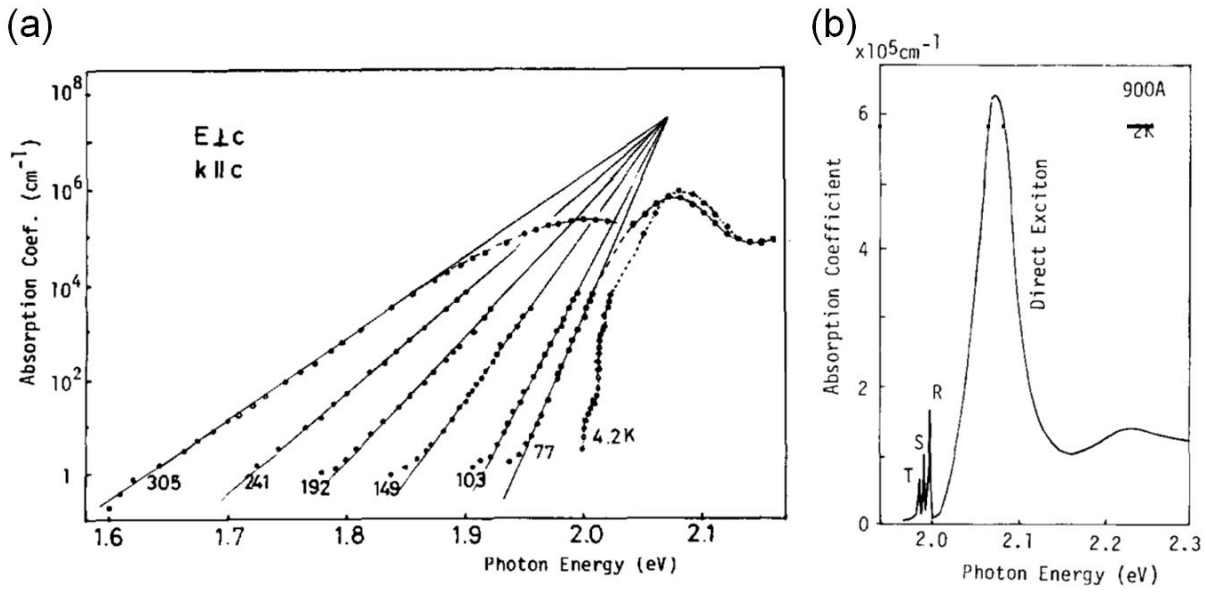

Figure 5.2 Modified from ref [109]. (a) Absorption spectra of single crystal BiI_3 at various temperatures. (b) Absorption of 90 nm thick single crystal at 2 K showing stacking fault excitons R, S, and T.

5.2 Structural characterisation and electronic band structure

5.2.1 Structural characterisation of BiI_3 powder at low temperature

The crystal structure of bismuth iodide has been already extensively studied, however, there is an absence of literature data for cryogenic temperatures. Therefore, BiI_3 powder was placed in a cryogenic sample stage and the X-ray diffraction (XRD) patterns were measured at various temperatures between 12 K and 280 K. The resulting patterns are shown in Figure 5.3. No new peaks appeared over the whole temperature range and the patterns were fitted using Rietveld refinement (as detailed in Section 3.2) to show that the phase stayed constant, in the rhombohedral $R\bar{3}$ structure. This confirms that the low-temperature spectroscopic measurements which follow provide information about the room-temperature phase of the material, which is relevant to room-temperature applications in optoelectronic devices.

On increasing the temperature, the peaks shifted due to thermal expansion, especially from 96 K to 280 K. There were also some changes peak height and increase in full width half

maximum at higher temperatures, which can be attributed to phonons creating more disorder in the system and broadening the peaks.

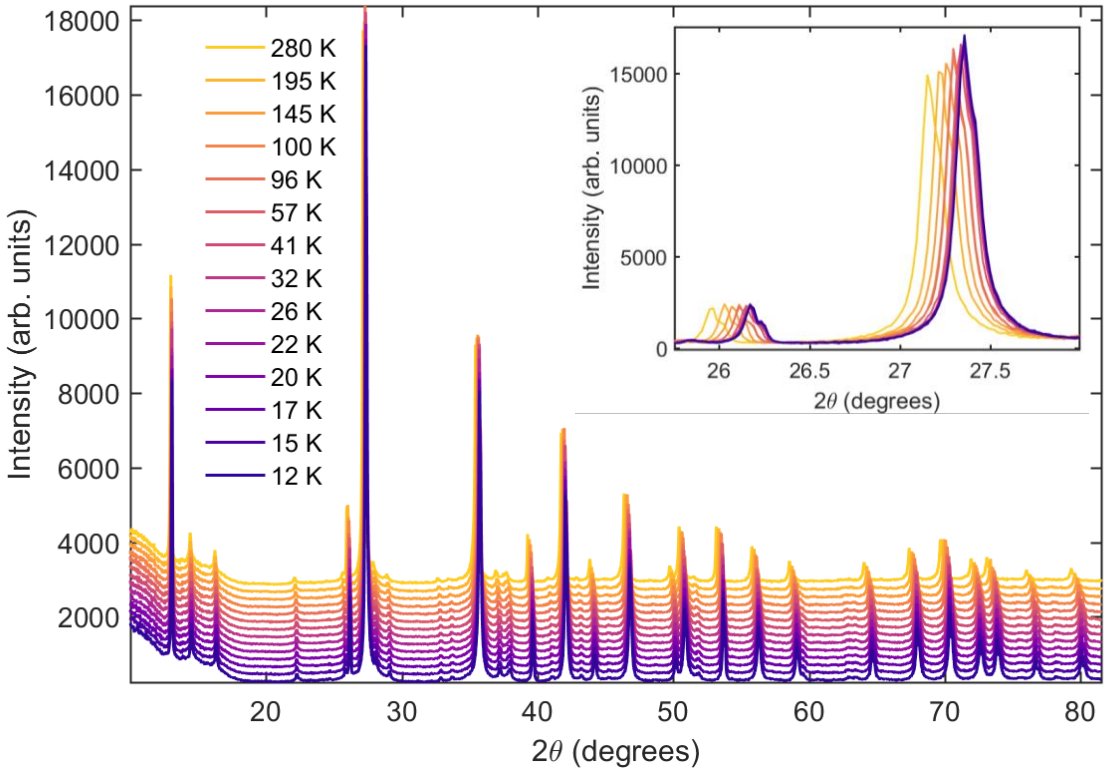

Figure 5.3 Powder XRD patterns for BiI_3 at various temperatures between 12 K and 280 K. Each pattern is vertically offset for clarity. The inset shows the temperature evolution of the most intense peak around 27.3°, where all peaks are plotted on the same scale. These data were taken by Tim van de Goor.

5.2.2 Band structure calculations of BiI_3

Due to inconsistencies in the previously reported band structures of BiI_3, and in order to aid our interpretation of the spectra which follow, the band structure was calculated using DFT. The VASP package was used with the PBEsol functional in combination with the Tkatchenko-Schaeffler dispersion correction method. Geometry optimisations were conducted with an energy cutoff of 550 eV and an 8x8x8 Brillouin zone grid. The band structure was calculated with the PBEsol functional with spin-orbit effects included via the second-variational method using an energy cutoff of 350 meV and an 8x8x8 Brillouin zone grid. The PBEsol functional was used because it was found to capture the 0 K lattice parameters most accurately, through a comparison of different functionals. The comparison also revealed a high sensitivity of the band edge positions on the lattice parameters, which

suggests that the band edge may show a strong temperature dependence. However, the general form of the band structure was consistent with most reported calculations.

The calculated band structure exhibits a very flat valence band edge with the valence band maximum (VBM) occurring between the Γ and F high symmetry points. The band gap was found to be indirect, with the conduction band minimum (CBM) lying between Γ and T. However, the flatness of the valence band means that only low energy phonons would be needed to enable optical transitions or scatter holes to other parts of the valence band.

Remarkably, the conduction band has a small gap in the density of states at around 2 eV, about 500 meV above the band gap, which is consistent with previous calculated band structures. The bands at the conduction band edge have contributions from both Bi and I p-orbitals, which would suggest that any change in the bonding character of neighbouring bismuth and iodide ions would have the strongest effect on the conduction band.

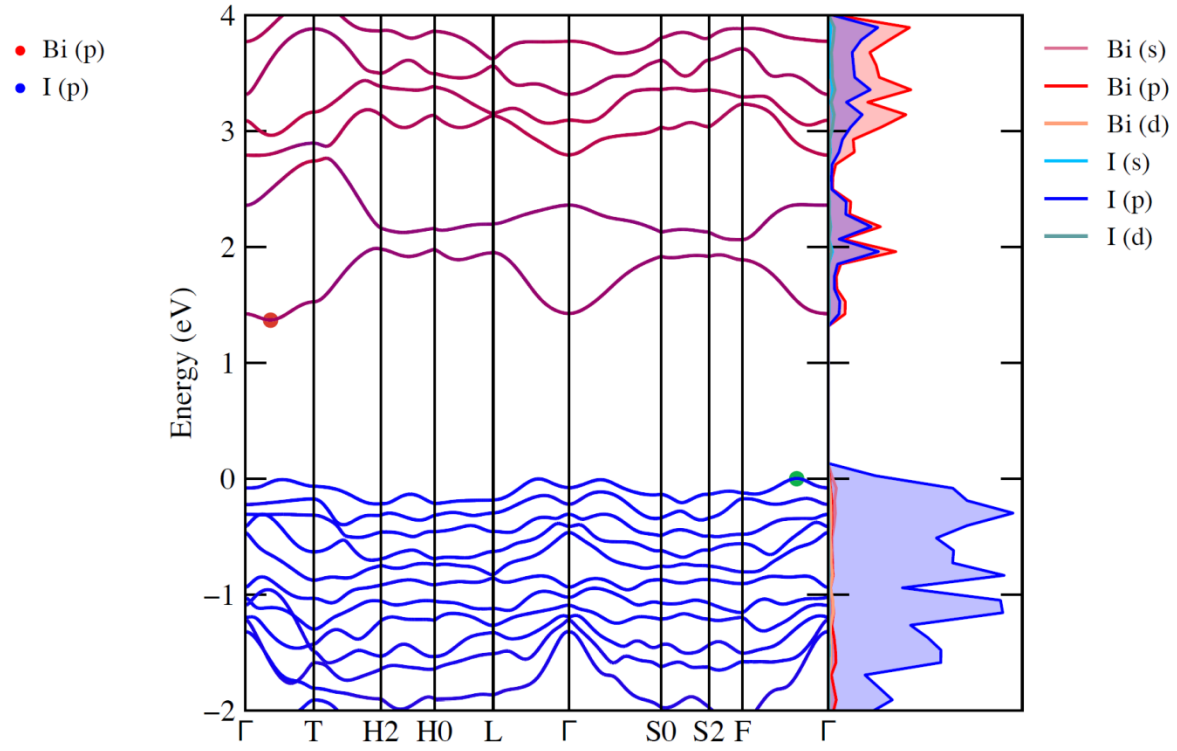

Figure 5.4 Calculated band structure using DFT with the PBEsol functional and spin-orbit effects included, together with the DOS on the right. Orbital contributions from the p-orbitals of Bi and I are shown in red and blue, respectively, and the VBM and CBM highlighted. These calculations were performed by Ivona Bravić.

5.3 Characterisation of excited states in BiI_3

5.3.1 Characterisation of electronic states in single crystal BiI_3

Single crystals of BiI_3 were grown by Robert Jagt using a physical vapour transport method. The crystals measured took the form of flat flakes, approximately 0.5 mm thick and 5 × 5 mm wide, where the largest area facet was assumed to be the (001) face of the crystal. The crystals were characterised by steady state reflectivity and photoluminescence measurements. The reflectivity measurements were performed on a single crystal using a Shimadzu UV-visible spectrophotometer with an integrating sphere. The absorbance was calculated from the reflectivity, R, with the relation $\log(1/R)$. The absorption onset implies a band gap of approximately 1.6 eV and, at higher energies, the absorption is not monotonically increasing, consistent with previous reports [72]. This could be due to contributions from excitonic transitions giving rise to peaks near the band gap and, considering that the calculated DOS has a small gap ~500 meV above the conduction band edge, this would be expected to give rise to a reduced absorption at higher energies.

The PL spectrum was taken by exciting the (001) face of the crystal at normal incidence with a pulsed laser source (3.1 eV, at a fluence of 700 μJ cm^{-2}). Emitted light was collected by a 150 mm focal length, 2 inch diameter lens and, after dispersion in a spectrometer, detected using an intensified charge coupled device (iCCD).

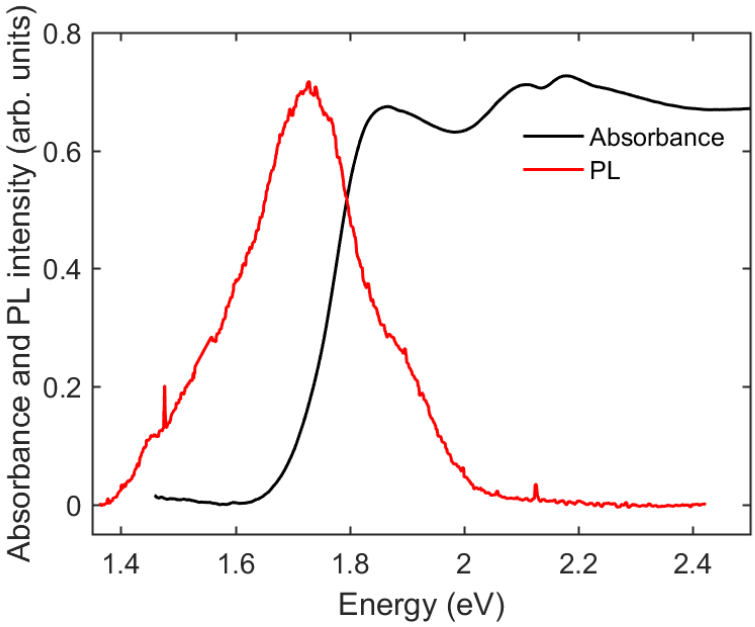

Figure 5.5 Absorption spectrum and PL spectrum at room temperature. Excitation of PL was at 3.1 eV and detected with an iCCD. Reflectivity data were taken by Sascha Feldmann.

The collected PL was spectrally broad but peaked close to the band edge at 1.7 eV (Figure 5.5). A shoulder can be seen approximately 100 meV higher in energy than the main peak, suggesting that there are isolated populations of excitations which cannot transfer energy or charge carriers between them. The time dependence of the spectrum could not be determined as the PL decayed within the 4 ns resolution of the instrument.

5.3.2 Electronic states in single crystal BiI_3 at low temperature

To discover the origin of the broadening of the PL spectrum, I performed a temperature series of PL measurements under the same conditions (Figure 5.6 & Figure 5.7). As the temperature decreases from room temperature to 145 K, the PL increases in intensity, shifts to higher energies, and remains broad. From 96 to 15 K, the peaks narrow and continue to increase in intensity, but no longer shift in energy. The increase in intensity suggests that the emission is not phonon-assisted, indirect, band-to-band recombination but more likely to be from the direct exciton (the excitonic nature will be discussed further in Section 5.3.4). The peak energy has the same temperature dependence as the reported band gap shift, which suggests that the direct exciton maintains a constant binding energy. The high temperature quenching and broadening will be explored in Sections 5.3.3 and 5.3.5.

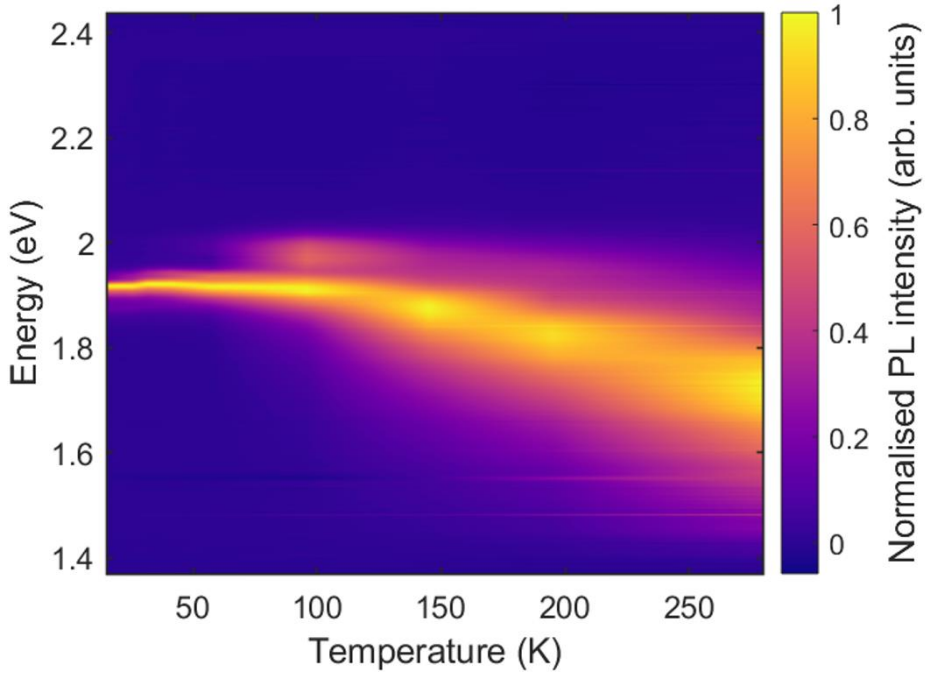

Figure 5.6 Normalised PL spectra of BiI_3 single crystal at a series of temperatures between 15 K and room temperature. All were excited using 3.1 eV pulses at a fluence of 700 μJ cm^{-2}.

At low temperatures, the PL spectrum includes three distinguishable peaks. The emission intensity is highest from the second lowest energy peak, rather than the lowest, which could indicate that the lowest energy states have a lower density, are less occupied or have a smaller oscillator strength. It should also be considered that the PL collection efficiency could be lower for certain transitions, as the crystal is anisotropic and was measured from a fixed angle. The stacking fault excitons observed by Kaifu at 4 K were lower in energy and less intense than the direct exciton [109]. Therefore, stacking fault excitons may explain the low energy shoulder at low temperatures.

For all spectra, as before, the PL decay was within the 4 ns instrument response time, which means the change in lifetime of the emissive species cannot be resolved. However, the overall excited state lifetime will be resolved using transient reflection in Section 5.4.1.

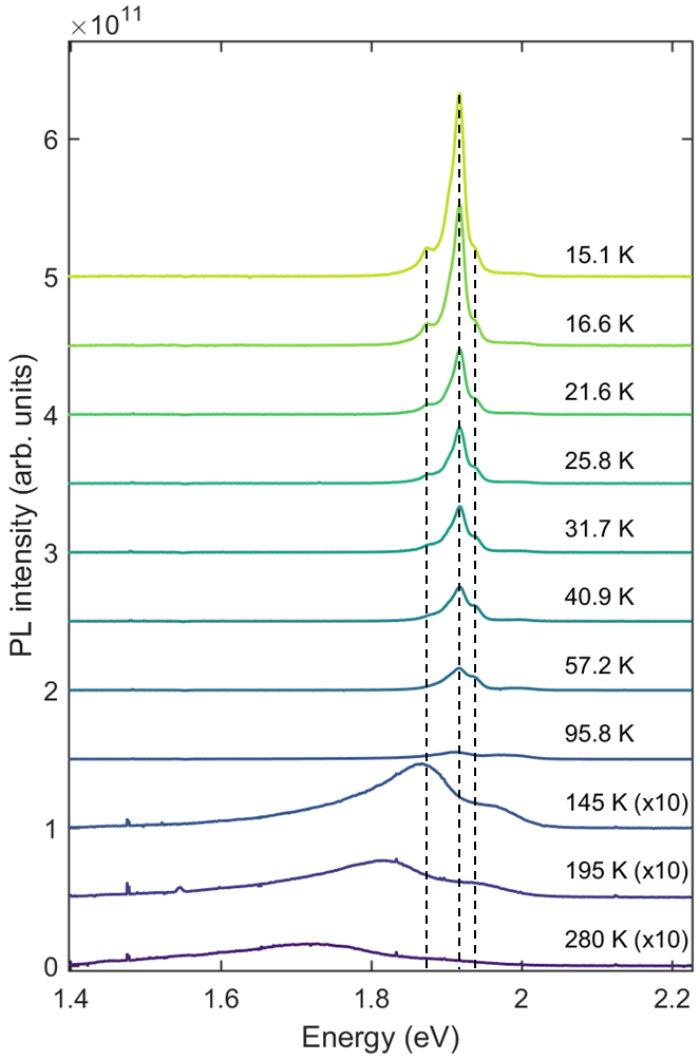

Figure 5.7 Series of PL spectra of BiI_3 single crystal at various temperatures between 15 K and room temperature. Spectra are vertically offset for clarity and the 145 K, 195 K, 280 K spectra are enlarged by a factor of 10. All were excited using 3.1 eV pulses at a fluence of 700 μJ cm^{-2}.

5.3.3 Phonon-assisted quenching of excitons in single crystal BiI_3

A simple phonon-mediated quenching model can be used to analyse the temperature-dependence of the direct exciton intensity. Phonons cause quenching of an exciton by scattering it into a non-radiative state, such as an indirect band edge state or at a defect acting as a recombination centre. The population of thermally excited phonons can be directly measured in Raman spectroscopy through the ratio of anti-Stokes to Stokes Raman scattering. If the rate of non-radiative decay, k_{nr}, depends of the density of phonons N_{ph} as $k_{nr} = k_{nr,0}N_{ph}$, and assuming a fixed radiative rate, k_r, then the PLQE becomes,

$$PLQE = \frac{k_r}{k_r + k_{nr}} = \frac{1}{1 + \frac{k_{nr,0}}{k_r}N_{ph}}.$$

Therefore, the temperature dependence of the emitted intensity, I, is,

$$\frac{I(T)}{I_0} = \frac{1}{1 + \frac{k_{nr,0}}{k_r}N_{ph}(T)},$$

where I_0 is the PL intensity at 0 K and can be estimated by extrapolation. Taking T as an implicit variable, a plot of I_0/I against N_{ph} should show a linear relationship if the population of phonons is responsible for quenching the PL.

Raman spectra covering both Stokes and anti-Stokes sides of the laser line were taken using a 785 nm (1.56 eV) CW laser, for a single crystal sample in a cold finger cryostat at temperatures between 4 K and 140 K (Figure 5.8). The ratio of anti-Stokes to Stokes intensity was then calculated for each mode at each temperature, and related to the PL peak intensity in Figure 5.9.

The relationship is linear from 22 – 57 K with similar gradients but outside of this range, the nonlinearity varies depending on the phonon mode. This could suggest that at high temperatures, the 115 cm^{-1} mode has a greater impact on the loss of PL intensity than can be modelled by increased non-radiative recombination rates. I hypothesise a corresponding decrease in oscillator strength which decreases the radiative rate. This will be discussed further in Section 5.4.1.

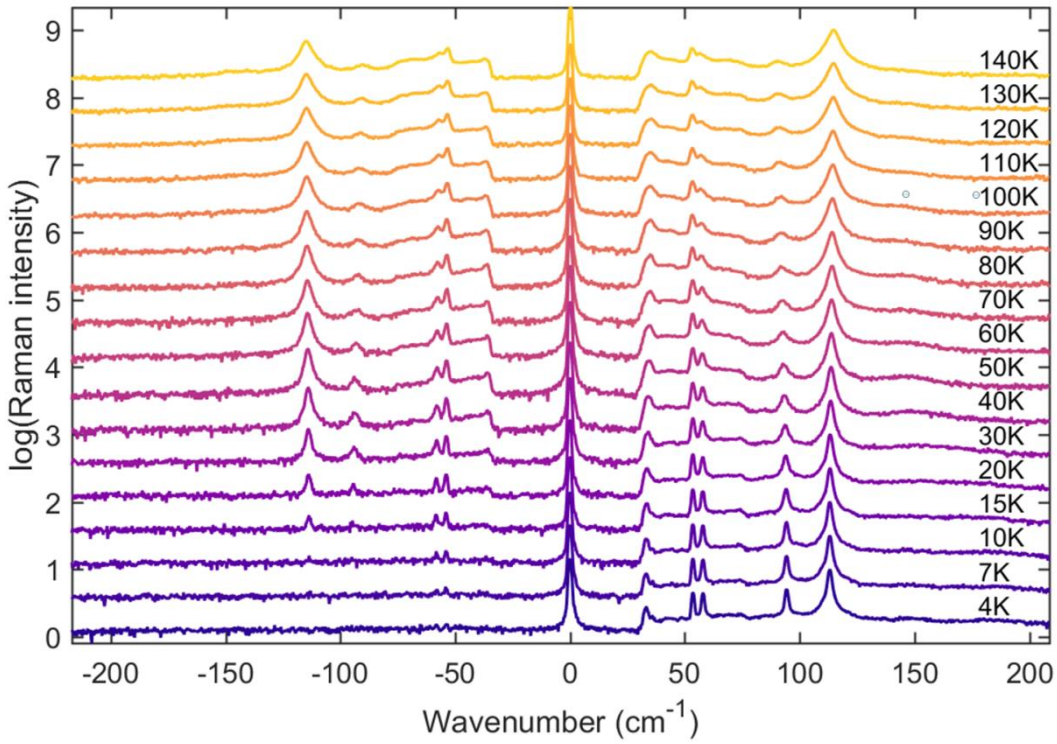

Figure 5.8 Raman spectra of a BiI_3 single crystal at various temperatures between 4 K and 140 K, vertically offset for clarity. These data were taken by Prof. Richard Phillips.

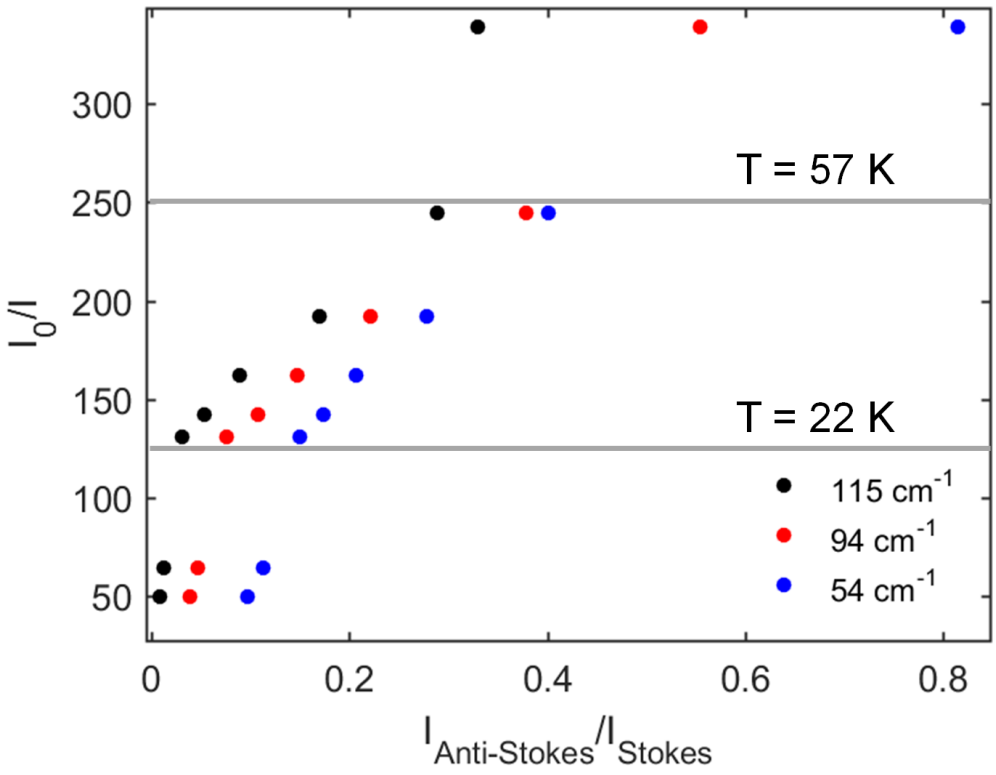

Figure 5.9 Dependence of the direct exciton PL peak intensity on the population of phonons for three modes observed in Raman.

5.3.4 Excitonic emission

PL experiments with a series of pump fluences were performed at 17 K to investigate character of the emissive species. The normalised spectra are shown in Figure 5.11. All the spectra show a main peak near 1.92 eV and a smaller peak at 1.87 eV but with increasing excitation density, the spectrum broadens on the low energy side of the main peak, rising into a shoulder upon excitation with higher fluences. This could be due to exciton-exciton interactions broadening the transition or the formation of biexcitons. There are also sharp peaks at 1.865 eV and 1.91 eV, which are likely due to stacking fault excitons as shown by Kaifu [109].

To confirm the excitonic nature of the main peaks, the fluence dependent intensity of each was analysed separately. The rate of radiative decay has a different power law dependence on the excitation density for different species, i.e. $\Gamma \propto n^x$. For geminate recombination of excitons, $x = 1$, and for free carriers or excitons undergoing bimolecular recombination, $x = 2$. A log-lot plot of the intensity of each peak at various fluences is shown in Figure 5.11. The gradient for the peaks at 1.92 and 1.87 eV was close to 1 which is consistent with emission from excitonic states. The shoulder at 1.90 eV, has a superlinear dependence on the fluence which would support contributions from biexciton emission.

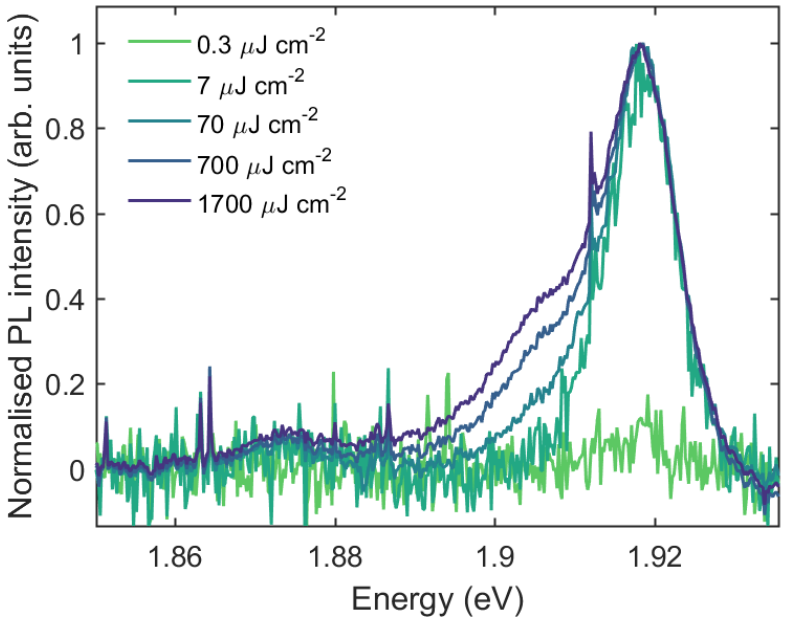

Figure 5.10 PL spectra at 17 K, exciting with various fluences, normalised to the peak at 1.92 eV.

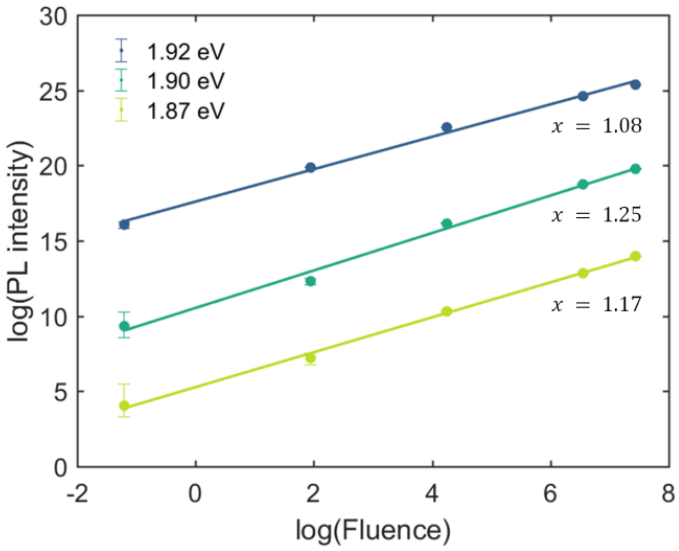

Figure 5.11 Log-log plot of the fluence dependence of each PL peak with fitted gradients, vertically offset for clarity.

5.3.5 Summary

Considering the whole temperature series, we have shown that the direct excitons at 1.92 eV become the dominant recombination pathway at temperatures below 57 K. This could be due to a lack of available phonons to aid non-radiative recombination processes, as explored in the quenching model. Another explanation involves dark excitons, which were predicted by introducing electron-electron interactions into the DFT calculations shown earlier. The binding energies of the dark excitons were in the same order of magnitude but their spatial extent was calculated to be smaller than the bright exciton. The delocalised bright electron is shown in Figure 5.12, where the wavefunction of the electron is plotted, assuming a fixed hole at an iodine site.

At temperatures below 15 K, the only phonons that will be thermally excited are acoustic phonons. However, once interlayer phonons are available, the delocalised direct exciton may be scattered into the more localised, dark excitonic states, which is responsible for the decrease in intensity of the direct peak up to 81 K. Above 115 K (10 meV), the high energy, intralayer phonons are thermally excited and the energy of the transition decreases due to the redistribution of charge along Bi-I bonds. This also drives the reduction in band gap energy at higher temperatures due to electron-phonon coupling. The effect of intralayer phonons on the direct exciton will be explored further in section 5.5.

5.3.5 Summary

Time-resolved PL measurements with a better resolution than 4 ns would allow the radiative recombination rate to be explicitly measured. However, this would require lower gain to be used on the iCCD or another technique such as time correlated single photon counting (TCSPC). In our TCSPC setup, the signal is too low to detect at the available excitation fluences, therefore transient reflection provided a better measure of the recombination timescales of the excitons in this system. The results of the transient reflection measurements will be discussed in the next section.

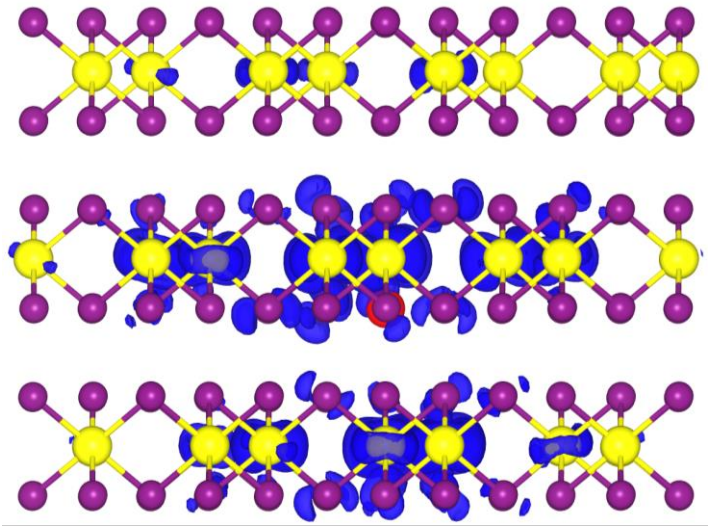

Figure 5.12 Spatial extent of the electron wavefunction for the first bright exciton at 2.05 eV. Hole position is marked in red, electron probability density in blue, bismuth in yellow and iodine in purple. Calculations were done by Ivona Bravić.

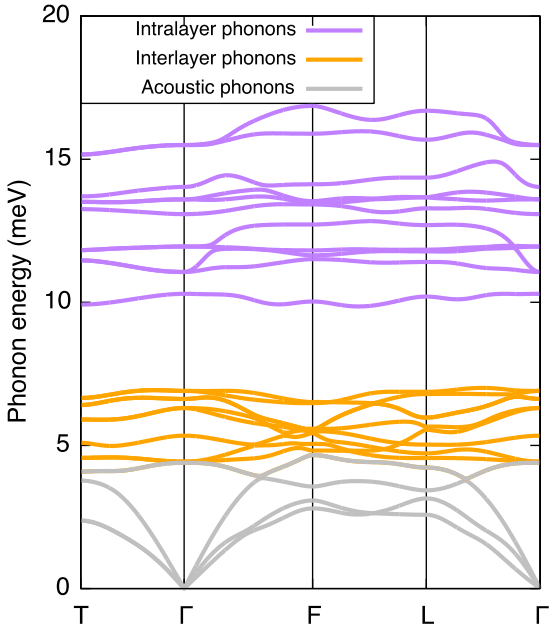

Figure 5.13 Calculated phonon dispersion curve showing the relative energies of acoustic, interlayer and intralayer modes, by Ivona Bravić.

5.4 Excited state dynamics in BiI_3

5.4.1 Ultrafast transient reflection at ambient and low temperature

Transient reflection (TR) was used to measure the excited state dynamics in the single crystals. Ultrafast TR spectra were taken by pumping the single crystal with 2.25 eV, 100 fs laser pulses and probing with broadband visible (100 fs) pulses in reflection, at close to normal incidence (~10°) to the (001) face of a single crystal of BiI_3. The TR spectrum of a single crystal of BiI_3 exhibits a Gaussian derivative feature with a peak at 2 eV (Figure 5.14). This is characteristic of an excitonic transition which broadens and shifts to higher energy upon excitation. The 4K spectrum shows similar features, except that the peak is narrower and the negative signal is greater on the high energy side.

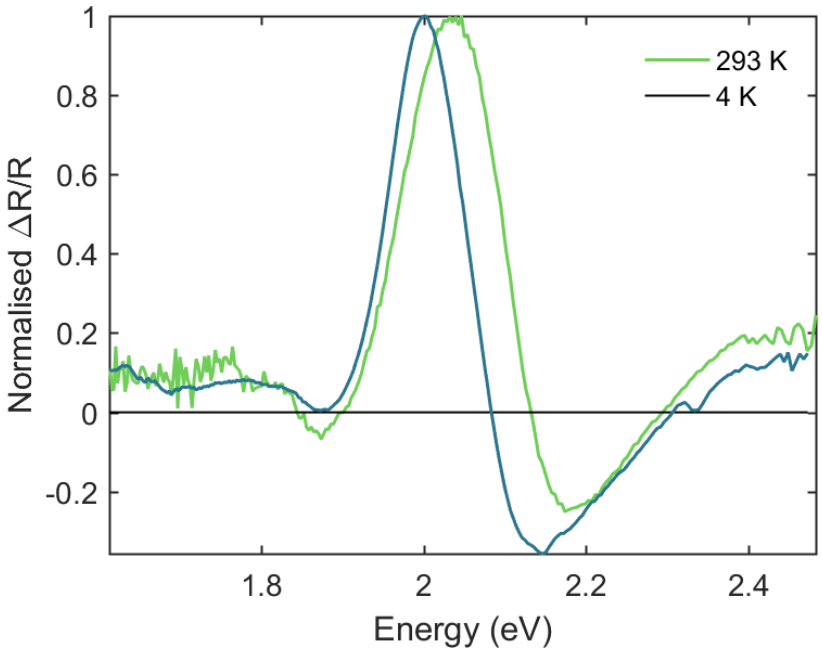

Figure 5.14 TR spectra at a pump-probe delay of 1 - 10 ps measured at room temperature and 4 K. Pump energy was 2.25 eV and fluence 32 μJ cm^{-2}.

The decay of the population of excitations can be tracked by the overall decay of signal, therefore, the peak at 2 eV was integrated for each time delay and plotted in Figure 5.15. The normalised traces show the same time evolution to within experimental noise which shows that the temperature of the crystal does not have a significant impact on the overall recombination dynamics before 1 ns. Therefore, any phonon-mediated increase in non-radiative recombination at high temperatures must be counterbalanced by a decreased

radiative rate. This provides further evidence to support the proposed loss of oscillator strength which contributes to the drop in PL intensity at high temperature (Section 5.3.5).

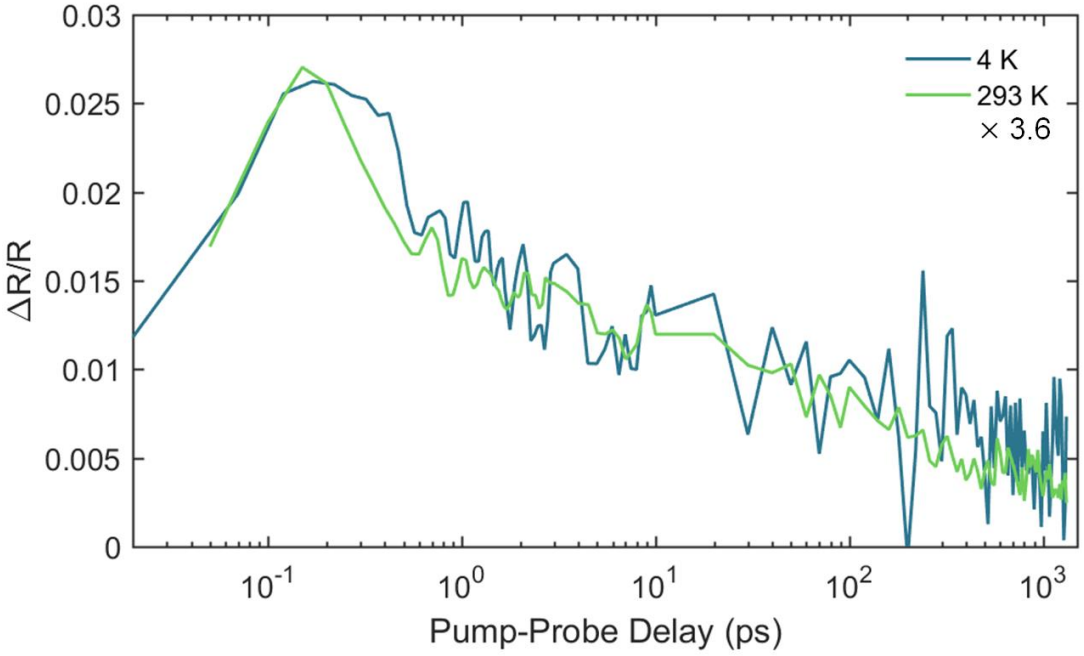

Figure 5.15 Short time TR kinetics of the large GSB signal integrated between 1.95 - 2.07 eV for both the room temperature and 4 K measurements. The room temperature data were scaled up by an arbitrary factor of 3.6 for ease of comparison.

5.4.2 Excited state lifetime in long time transient reflection

The total carrier lifetime at room temperature has so far only been extrapolated from short time transient absorption (4.6 ns) [110] or fitted from very weak and short-lived PL signals in TCSPC (1.31 ns) [73]. Therefore, I measured the recombination processes happening on the nanosecond timescale in TR by pumping with 2.33 eV, 1 ns pulses and probing as before.

The spectrum again shows a peak at 2 eV, but now has the form of a Gaussian peak second derivative (Figure 5.16). The population of excitations can still be tracked by the decay of signal (Figure 5.17). The lifetime stays constant when the fluence was varied by an order of magnitude. Therefore, the recombination regime is monomolecular, which is indicative of either Shockley-Read-Hall (SRH) recombination or radiative, geminate recombination of the excitons. Given that the PL has entirely decayed by 4 ns, SRH is the more likely recombination mechanism. From a monoexponential fit, the lifetime was found to be 72 ± 12 ns, which is longer than either of the previous values.

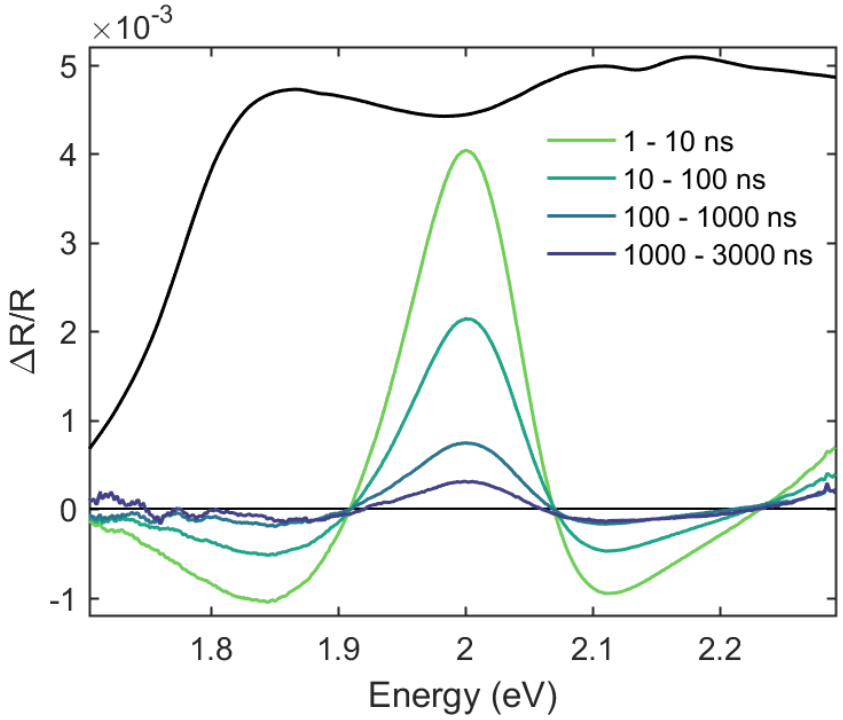

Figure 5.16 Long time TR spectra pumping at 2.33 eV and a fluence of 54 μJ cm^{-2}. Black line is a scaled linear absorption spectrum for reference.

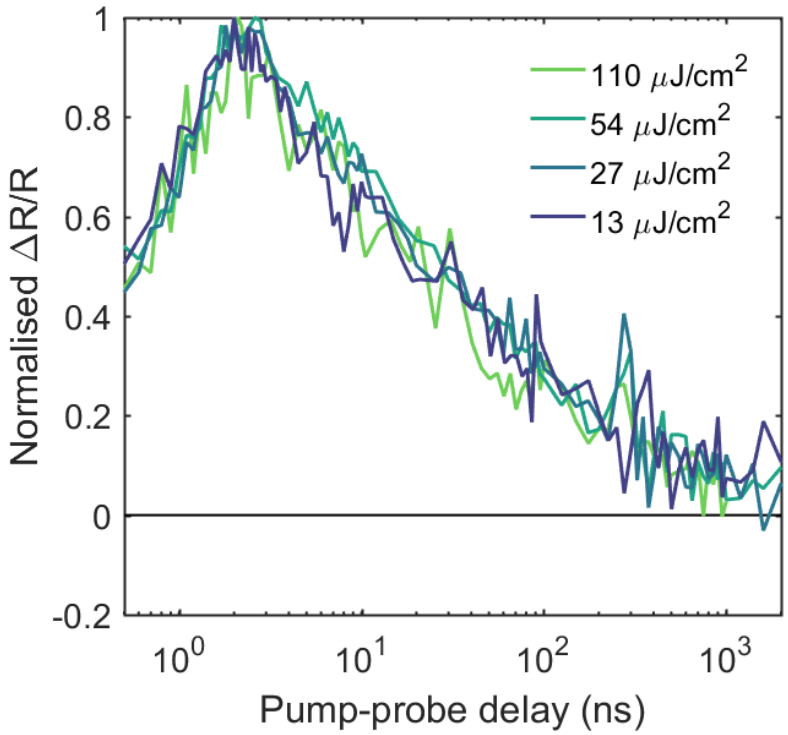

Figure 5.17 Normalised TR kinetics of the peak integrated between 1.94 eV and 2.07 eV at various fluences.

5.5 Phonon coherences in thin films and single crystals

To further explore the role of phonons and their interaction with excitons in BiI_3, vibrational spectroscopy was performed using ultrafast transient absorption (TA) measurements of a thin film. Thin films are required to allow enough probe light to pass through the sample, such that the assumption that the change in transmission is a small proportion of the total transmitted intensity still holds for photon energies above the bandgap. Solution processed thin film samples were made by Robert Hoye as reported by Brandt et al. [73]. The sample was pumped with 2.48 eV, 100 fs pulses and probed with broadband, visible, 100 fs pulses in transmission at room temperature.

Coherent oscillations in the magnitude of the differential transmission, $\Delta T/T$, were observed at delay times up to 3 ps (Figure 5.18). In order to compare the frequency of these oscillations, a multiexponential decay curve was subtracted from each wavelength, leaving an oscillating residual centred on $\Delta T/T = 0$. This residual was then Fourier transformed to give the power spectrum of oscillating frequencies. The frequency, ν, is expressed in wavenumbers, $1/\lambda$, according to the relation $1/\lambda = \nu/c$, where c is the speed of light in a vacuum. These are compared with room temperature Raman scattering measurements in Figure 5.19.

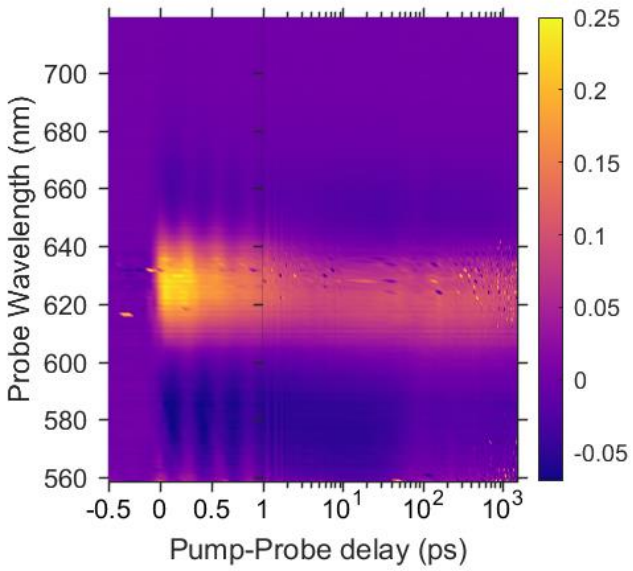

Figure 5.18 TA spectra of a BiI_3 thin film, pumped at 2.48 eV, at a fluence of 200 μJ cm^{-2}. The colour scale is $\Delta T/T$ value.

The main peak at ~115 cm^{-1} is seen in all spectra, which has A_g symmetry [109], but the resonant Raman (using 2.33 eV excitation) has an additional peak at 160 cm^{-1}, which does not contribute to the resonant TA oscillations. This peak has previously been assigned to PL in low-temperature resonance Raman [111], however, our PL measurements showed that the direct exciton emission is significantly broadened and centred at 1.7 eV at room temperature, with no PL intensity detected near 2.33 eV. Therefore, the peak at 160 cm^{-1} must be a Raman mode associated with the excited state. This confirms that not all Raman active modes contribute the coherent oscillations.

My measurements contradict the impulsive stimulated Raman interpretation proposed Scholz et al. [110]. They claim to observe two coherent phonon modes: of 95 cm^{-1} (E_g symmetry) as well as the 114 cm^{-1} A_g mode in their TA data and therefore explained the generation of coherent phonons with impulsive stimulated Raman. However, in their spectrum, the weaker 95 cm^{-1} mode lies within the wings of the intense 114 cm^{-1} mode, could not be resolved as a distinct peak, and is not significantly more intense than the noise level.

I therefore suggest that the coherent phonons are generated by an impulsive absorption mechanism, where the charge distribution of the exciton wavefunction increases screening between neighbouring ions, initiating coherent vibrations of modes associated with a Bi-I bond stretch [112].

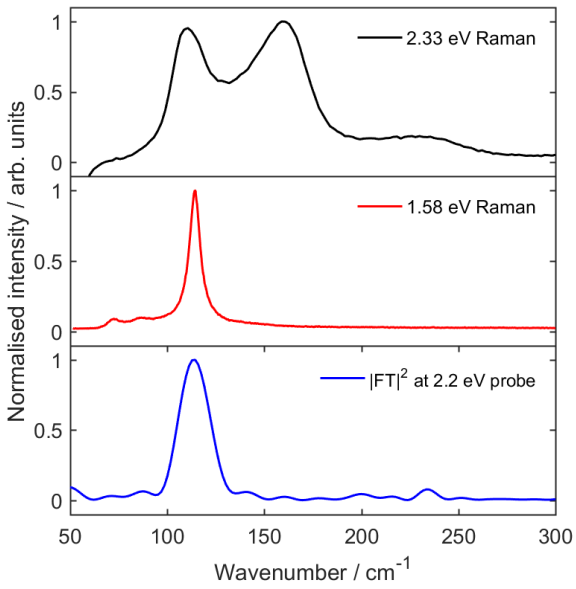

Figure 5.19 Raman spectra (black and red) and Fourier transform of oscillations in the TA signal (blue), all at room temperature. A probe energy of 2.2 eV (565 nm) was selected for the FT power spectrum, which is representative of the other probe energies. The Raman spectra were taken using a 2.33 eV and 1.58 eV laser line to excite resonantly and non-resonantly, respectively. Raman experiments were performed with assistance from Dr. Tudor Thomas.

5.6 Conclusions and further work

In summary, I have shown that in BiI_3, the direct exciton has a strongly temperature-dependent PL emission, from being weak and spectrally broad at room temperature to various bright excitonic peaks at 15 K. Two regimes were identified as the temperature increased: a decrease in peak intensities followed by a red shift and broadening of the main peaks. In the absence of a phase transition from low-temperature powder XRD, a phonon-mediated quenching model was applied. At low temperatures, the trend in PL intensity could be explained by interlayer phonons scattering delocalised direct excitons into dark excitonic states. At high temperatures, the decrease in PL intensity could not be accounted for purely by the phonon population increasing the non-radiative recombination rate. As the overall excited state decay does not change significantly, according to TR measurements, the radiative rate must therefore decrease with increasing temperature. Together this evidence points to a decrease in the oscillator strength of the exciton with increasing temperature above 57 K.

The lifetime of the excited state in single crystal BiI_3 was directly measured at room temperature using nanosecond TR and found to be 72 ± 12 ns — longer than previously reported by time-resolved PL measurements and ultrafast TA. This indicates that thin films can be viable for PV, if their defect states can be passivated or eliminated through better processing. However, on comparison with the double perovskite material in the previous chapter, this material has a fundamentally shorter charge carrier lifetime and is less robust to defects. Therefore, better options currently exist for non-toxic solution processable semiconductors for PV.

Coherent phonons observed in TA measurements of thin films showed that there are phonon modes with an energy of 14 meV which couple strongly to the electronic states. My results suggest that these phonons are generated by impulsive absorption rather than impulsive stimulated Raman scattering.

Future avenues for exploration would involve linking the impulsive absorption to PL; ultrafast time-resolved PL would show if this mode is responsible for changing the oscillator strength of or broadening the direct exciton. In addition, temperature-dependent PL excitation (PLE) scans would provide more information about the sub-gap luminescence and any phonon-mediated absorption or emission processes. Further theoretical calculations could

help to show what the spatial distribution of the electron and hole wavefunctions are and the possible lattice distortions they could cause.

Another obvious route for this material would be to explore how nanostructuring affects all these properties, and research is currently ongoing to isolate single triatomic layers reliably enough to do spectroscopy on them. If the fabrication is improved, BiI_3 could be studied for applications as a 2D semiconductor.

Chapter 6: Origin of energetic disorder in bismuth oxyiodide

The aim of this chapter is to understand energetic disorder in bismuth oxyiodide, BiOI. I observe heavily Stokes-shifted and broad low temperature PL from radiative recombination of self-trapped excitons or trap states. The transient absorption signature is also broad but at higher energies, due to charge carriers at the non-dispersive band edges. I use ultrafast transient absorption to establish the overall carrier lifetime, which is shorter than any of the previous materials, and perform a more in-depth study of the coherent phonon modes generated with different pump energies.

6.1 Introduction

Bismuth oxyhalides, BiOX (X = Cl, Br, I) are semiconductors which have been previously studied for photocatalysis applications [113][114], as well as pigments in cosmetics [115] and gas sensors [116]. Bismuth oxyiodide, BiOI, having the lowest bandgap of the series (~1.9 eV [76]), has also been identified as a non-toxic alternative to perovskites for photovoltaic absorbers [77]. Following defect calculations predicting few deep trap states intrinsic to the material, polycrystalline thin films grown using chemical vapour transport have been used as the absorber layer in solar cell devices with PCEs of 1.8% [78].

The crystal structure is tetragonal, with the matlockite structure, and consists of layers of I-Bi-O-Bi-I atomic planes held together by van der Waals interactions (Figure 6.1(a)) [114]. The calculated band structure has an indirect band gap, but with a very flat valence band edge (Figure 6.1(b)) [76]. The conduction band is dispersive in some directions around the minimum but flat along Γ to Z, which in real space is the direction perpendicular to the layers. This means that transport of electrons is effectively restricted to the in-plane directions within a layer.

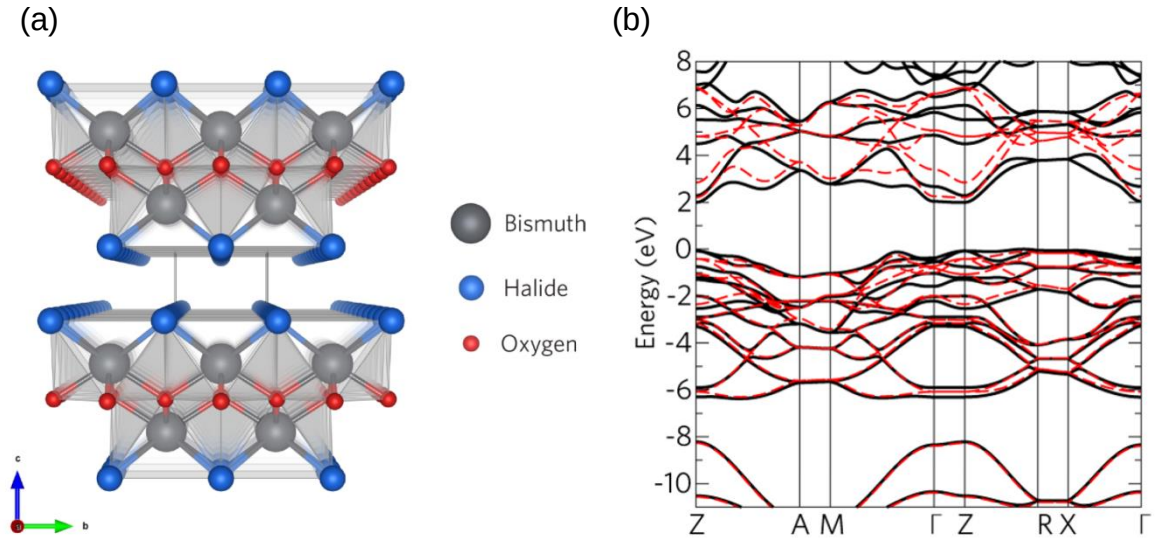

Figure 6.1 Taken from ref [76]. (a) Crystal structure of bismuth oxyhalides, BiOX. (b) Band structure of BiOI accounting for relativistic and orbital effects.

The $[Bi_2O_2]^{2+}$ regions and widely spaced I^- planes in the crystal structure may also have the effect of creating an internal electric field, which some researchers have suggested facilitates charge separation after photoexcitation, enabling the high levels of photocatalytic activity [117]. This proposed spatial separation of electron and hole may cause the low levels of photoluminescence observed from BiOI. Weak PL signals have presented some challenges towards studying its optoelectronic properties, however a charge carrier lifetime of 2.7 ns was measured in a thin film using TCSPC [78]. This was deemed long enough to merit further study but is in need of improvement if the material is to compete with the lead-free double perovskite absorbers.

In this chapter, I will use temperature dependent PL and transient absorption spectroscopy to provide further information on the behaviour of photoexcited carriers in BiOI, in order to establish the fundamental limits to its performance in photovoltaic devices.

6.2 Characterisation of BiOI thin film

6.2.1 Sample morphology and crystal structure

Thin films of BiOI were grown by a chemical vapour transport method onto a substrate of glass and a deposited layer of nickel oxide, NiO_x. All measurements in Section 6.2 were taken of the same sample fabricated by Dr Lana Lee (Department of Materials Science and

Metallurgy, University of Cambridge) using a temperature of 400°C. When viewed under a scanning electron microscope (SEM), the film has lenticular grains, approximately 400 nm in size, with the van der Waals layers perpendicular to the substrate (Figure 6.2). From analysis of this micrograph, the area fraction covered by BiOI was found to be 8.9%.

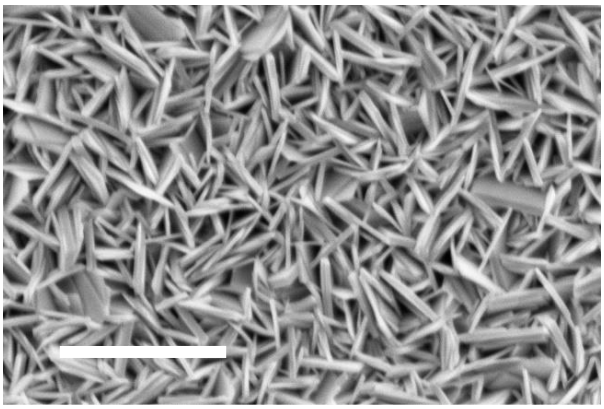

Figure 6.2 SEM micrograph of a thin film of BiOI. Scale bar is 2 μm. This image was taken by Dr Lana Lee.

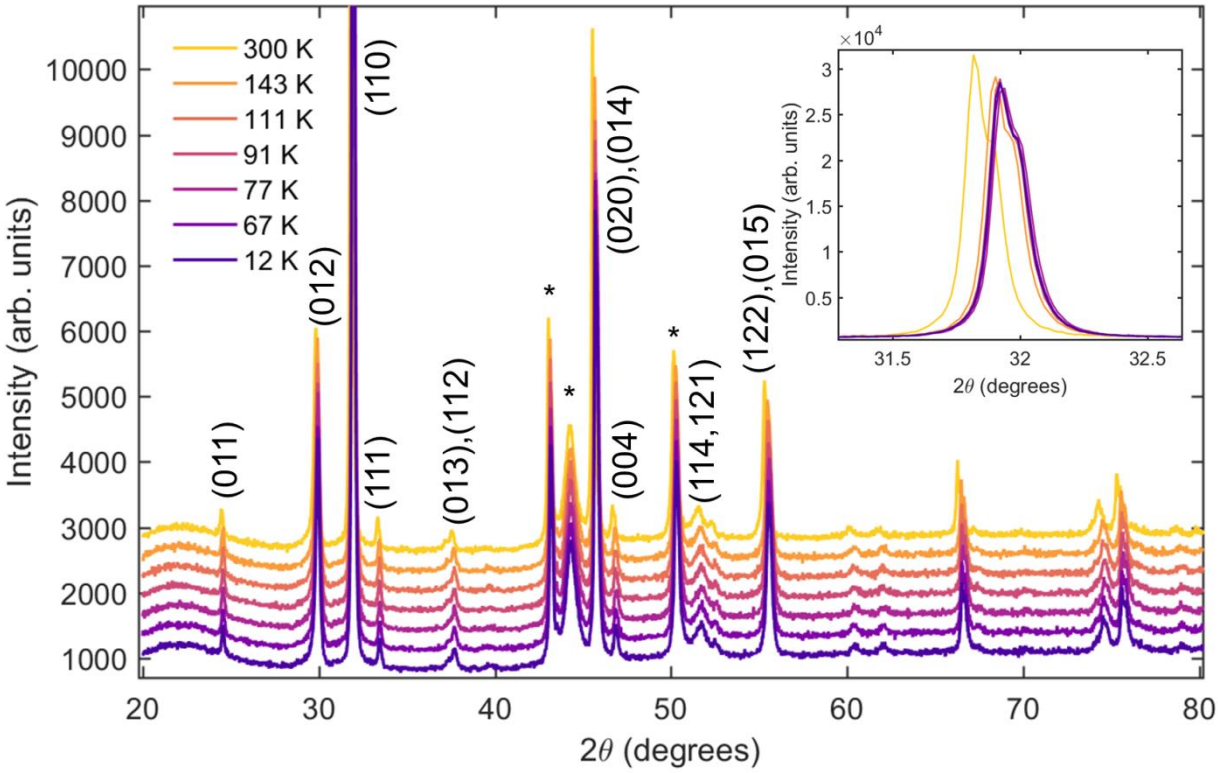

Figure 6.3 Low temperature XRD patterns taken of a thin film. Patterns are vertically offset for clarity. Highlighted peaks (*) are from the sample holder. Inset shows the shift of the peak at 31.9°.

The films were found to be phase pure using powder XRD, although the volume of material was low, giving rise to additional peaks from the chromium and copper phases in the sample holder (Figure 6.3). As the low temperature phase of the material is unreported, the film was also characterised by XRD at various temperatures between 12 K and 300 K. At low temperatures, the phase did not change, but the peaks shifted due to thermal contraction. This confirms that low temperature spectroscopy measurements can provide information about the room temperature phase of the material.

6.2.2 Characterisation of electronic states

The optical transmission and diffuse reflection of the film was measured inside an integrating sphere, as these BiOI films are strongly scattering. The data was analysed using Kubelka-Munk theory (as described in Section 3.3.1), which gave an absorption onset at 1.9 eV (Figure 6.4). PL measurements were done by exciting with a pulsed 3.1 eV laser source and detecting the emission with an iCCD. The resulting PL spectrum in Figure 6.4 is an inhomogeneously broadened peak at 1.75 eV, which is Stokes shifted by 150 meV from the band edge at 1.9 eV. Although the iCCD offers time-resolved capabilities, the decay lifetime was shorter than the instrument response of ~4 ns. The emission was so weak that the PLQE was below the detection limit of our integrating sphere setup, <0.01%.

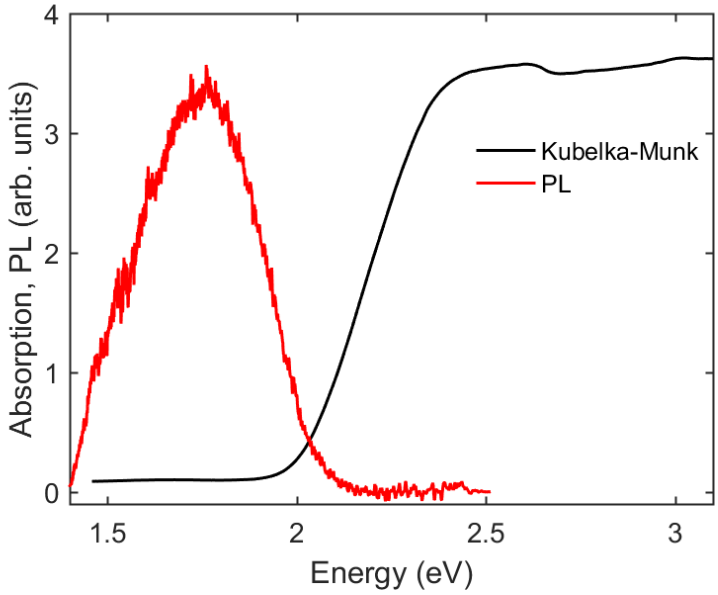

Figure 6.4 Absorption and PL spectrum of BiOI thin film. The absorption was calculated from diffuse reflectance using Kubelka-Munk theory. The PL was measured with 3.1 eV pulsed excitation (2 mJ cm^{-2}) and iCCD detection.

6.2.2 Characterisation of electronic states

In order to understand the origin of the PL, I investigated the temperature dependence of the emission. The PL spectrum was measured as before, but with the sample in a cryostat under helium gas atmosphere at various temperatures between 67 K and room temperature (Figure 6.5). For all spectra, two Gaussian peaks provided the best fit to the data, with each component broadened to a FWHM of at least 225 meV.

On decreasing the temperature, the intensity increased, especially of the low energy peak. Unfortunately, the iCCD is not sensitive to photons below 1.46 eV so the full extent of the low energy peak could not be measured. The increase in intensity confirms that the low energy emission does not come from a phonon-assisted indirect transition, rather, that the non-radiative recombination pathway is thermally activated. The line shape shows that the broadening is due to the energetic distribution of the emissive states, or very low energy phonons (<6 meV). This distribution could either originate from defect states, where carriers become trapped at different energy levels before emitting, or self-trapping of carriers by deformation of the lattice. In this case, self-trapping at two different lattice sites would better explain the two peaks observed. The shift of both peaks with temperature indicates a possible shift of the band gap, or a change in the deformation energy of the lattice which affects the self-trapping energy. The XRD measurements showed that there was no significant deformation of the lattice in the ground state at any of these temperatures, therefore, in order to distinguish between these two scenarios, low temperature absorption measurements would need to be performed with an integrating sphere.

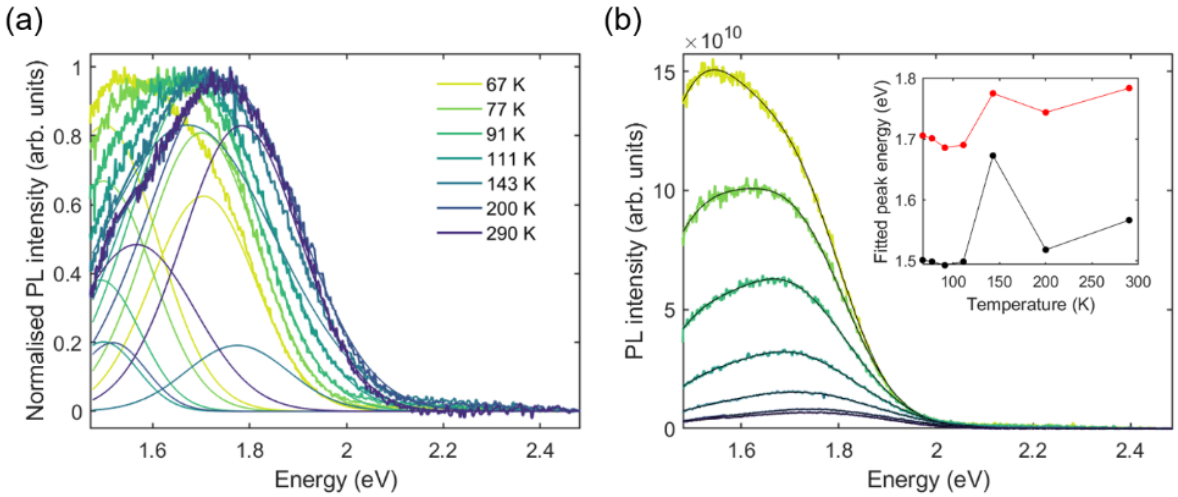

Figure 6.5 Low temperature PL spectra using 3.1 eV excitation and iCCD detection. (a) Normalised spectra (bold lines) with two fitted Gaussian components each (fine lines). (b) Absolute intensity of the PL (colour) with the result of the fit (black). Inset shows the temperature dependence of the centre energy of each Gaussian component. The abrupt change at 143 K is an anomaly introduced by the fitting.

A simple thermal activation model was used to find the activation energy, E_A of the non-radiative channel. For a similar phonon mediated quenching process to that described in Section 5.3.3, the following relationship is proposed between the PL intensity, I and the temperature, T,

$$\log\left(\frac{I_0}{I} - 1\right) = \frac{-E_A}{k_B T} + c \ ,$$

where I_0 is set to a value which approximates the PL intensity at $T = 0$ K, k_B is the Boltzmann constant and c is a constant. After fitting the data as shown in Figure 6.6, a linear relationship was found over the whole temperature range and the activation energy of the non-radiative channel was found to be 25.4 meV.

Again, the time dependence could not be resolved for any of the emission, which had decayed before 4 ns, therefore dynamic information must be gained through ultrafast transient absorption.

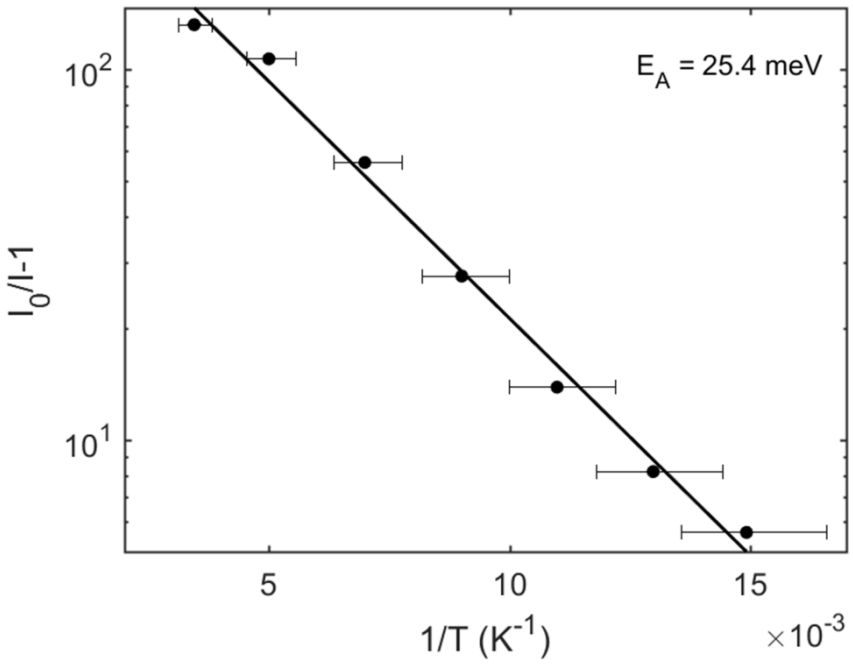

Figure 6.6 Relationship between temperature and total integrated PL intensity and linear fit to show the thermally activated quenching of the total emission.

6.3 Charge carrier lifetime

Ultrafast transient absorption experiments were performed at room temperature in order to resolve the evolution of the excited charge carrier population in time. The film was pumped with 3.1 eV, 100 fs pulses, and probed with white light pulses generated from a CaF_2 crystal. Due to the scattering nature of the surface of the film, it was necessary to pass the pulses through the substrate before overlapping on the film, but the band gap of NiO_x is 3.6 eV so there should have been no absorption of the pump or probe. The transient absorption spectrum of the film consists of a broad ground state bleach (GSB) signal centred around 1.9 eV, due to the occupation of the bands by photoexcited charge carriers (Figure 6.7(a)). The persistence of the broad feature could mean that carriers lie at energies more than 100 meV above the band edge for their entire lifetime. Alternatively, many different optical transitions could be blocked by the carriers lying close to the band edge, due to the flatness of the dispersion relation — allowing them to occupy a range of states in momentum space which are involved in a range of vertical transitions with different energies.

I investigated how the band fills with an increasing density of carriers by observing the shape of the initial GSB spectrum over an order of magnitude change in pump fluence (Figure 6.7). The expected response would be an increase in signal at higher energies relative to the low energies, however, in this case there is no significant change in the high energy side of the peak. This would support the case that the carriers are occupying band edge states but bleaching higher energy transitions due to the flat bands.

The area under the GSB from 1.88 to 1.94 eV was integrated to indicate evolution of the charge carrier population with time after excitation (Figure 6.8). The resulting kinetics are fluence dependent, with the low carrier densities following a monoexponential regime and the high fluence kinetic exhibiting a faster decay overall and a deviation from the monoexponential regime due to bimolecular and possibly Auger recombination at early times. Bimolecular, radiative recombination is almost negligible in these films due to their low PLQEs; therefore, Auger recombination is likely to contribute to the decay at carrier densities near 10^{18} cm^{-3}, which has also been reported at similar excitation fluences in BiOBr [118].

The decay after using the lowest pump fluence was fitted with a single exponentially decaying function in order to extract the lifetime of carriers undergoing monomolecular recombination. The fitted lifetime of 47 ps is the shortest of all the lifetimes reported so far.

Lifetimes of this order of magnitude were reproduced in TA measurements of other batches of films grown with the same method. The PL lifetimes of 2 ns found by Hoye et al. were measured using a much lower excitation fluence and may have been from a long-lived tail that our TA was not sensitive enough to detect.

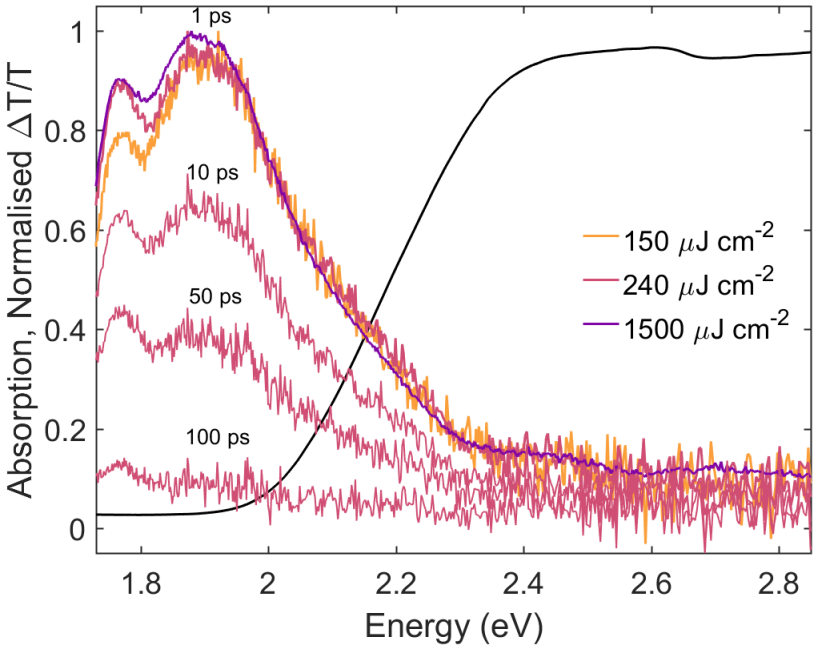

Figure 6.7 (black) Normalised steady state absorption spectrum, for reference, (colour) TA spectra at 1 ps after the 3.1 eV pump, comparing three fluences, and (pink) TA spectra at various times after excitation, using a 240 μJ cm^{-2} pump.

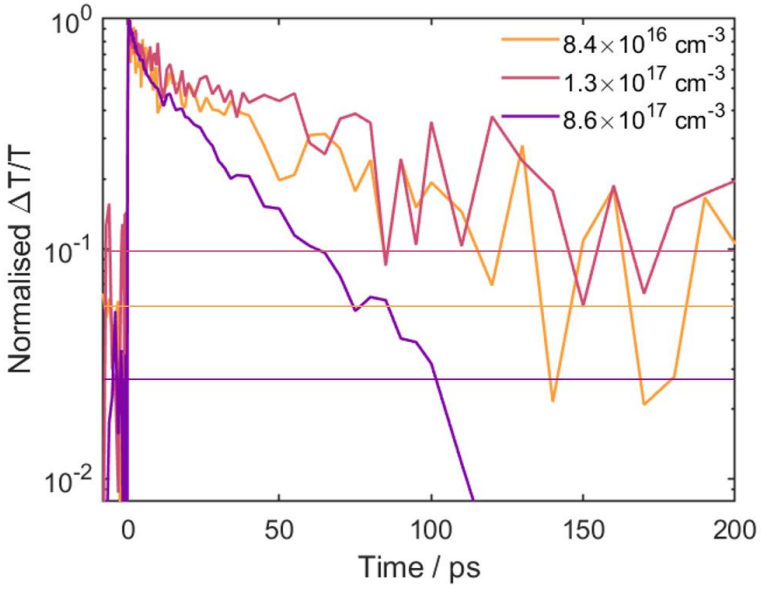

Figure 6.8 Decay of the integrated GSB signal between 1.88–1.94 eV with pump-probe time delay (bold lines) and the noise floor of each measurement (fine, horizontal lines). Decay curves are normalised to the maximum value in order to compare the relative kinetics.

6.4 Carrier-phonon coupling

6.4.1 Excess energy and coherent vibrations in BiOI

As seen in $Cs_2AgBiBr_6$ and BiI_3, there are clear oscillations in the signal at early times. In order to study these with good time resolution, a BiOI film was grown on a 170 μm glass coverslip to avoid dispersion of the pulses when passing through the substrate. This sample was excited with 2.64 eV pulses and showed a similarly broad GSB peak centred at 2.07 eV. The kinetics of the GSB at two pump fluences are shown in Figure 6.9(a). The modulation amplitude scaled with the signal magnitude. This is one indication that the oscillations are caused by the presence of photoexcited carriers.

After performing a Fourier transformation on the oscillating component, as described before in Section 5.5, two modes were found to contribute to the coherent oscillations – an 85 cm^{-1} (11 meV) mode and a 150 cm^{-1} (19 meV) mode (Figure 6.9(b)). On comparison with steady state Raman spectra, there is good agreement between the frequencies of these modes and the peaks in both Raman spectra, where the 85 cm^{-1} mode was previously assigned to the A_{1g} internal Bi-I stretching mode and the 150 cm^{-1} mode was assigned to the E_{1g} internal Bi-I stretching mode by Davies [119]. These phonons are therefore responsible for modulating the signal.

However, the 50 cm^{-1} Raman mode does not appear at all in the FT of the TA. The visibility of the Raman mode was not limited by the experiment as the lowest frequency we could expect to resolve is determined by the extent of our measurement time window, in this case 9 ps, corresponding to 3.7 cm^{-1}. Any peaks with an intensity on the same order of magnitude as the other Raman peaks would be visible above the noise floor of the FT spectrum. In the literature study, the 50 cm^{-1} mode was also not observed, although Davies suggested there could be further A_{1g} and E_{1g} bands below 50 cm^{-1}. The lack of this mode in the TA oscillations excludes the theory of impulsive stimulated Raman as a mechanism for producing the oscillations.

The ratio of peak heights is more similar to the resonant Raman than the non-resonant Raman, which also shows that the excited state is coupled to the phonons. Furthermore, when a sub-bandgap pump was used for TA at 1 mJ cm^{-2} (chosen to be a high fluence below the threshold for two-photon absorption), no oscillations were observed in the probe

transmission. Together with the previous observations, this points towards an impulsive absorption mechanism for generating the coherent phonons.

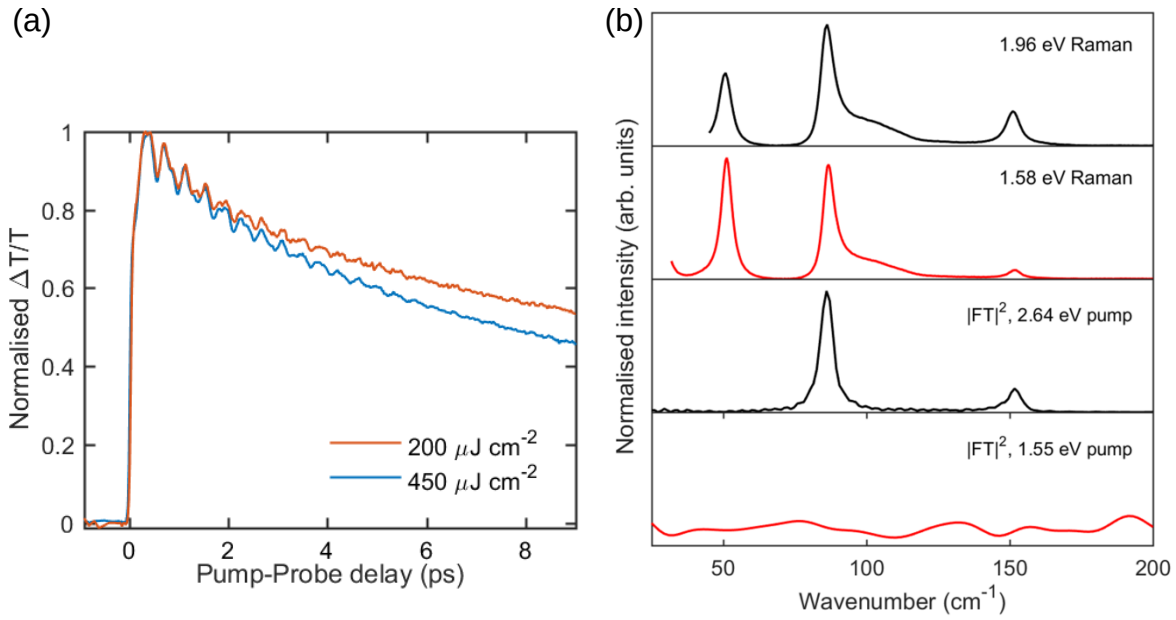

Figure 6.9 (a) GSB kinetics using a 2.64 eV pump, comparing two fluences. Probe energy was 2.07 eV. (b) Normalised resonant and non-resonant Raman spectra and Fourier transformed TA signal using an above bandgap pump (2.64 eV, 450 uJ cm^{-2}) and below-bandgap pump (1.55 eV, 1 mJ cm^{-2}). Probe energy for both TA plots was 2.08 eV. All spectra were normalised to the peak at 85 cm^{-1} except the below-bandgap pump TA, which was normalised to the peak at 0 cm^{-1}. The Raman data were taken together with Tudor Thomas.

To study the effect of excess energy on the generation of coherent phonons, a pump energy series was performed on the same spot of the film. The GSB spectrum shifts to lower energies as the pump energy decreases (Figure 6.10), while, at the lowest energies of 1.85 and 1.98 eV, a significant amount of the bleach appears above the pump energy. This supports the proposal that a population of carriers at the band edge can bleach multiple, higher energy transitions.

The spectrum of coherent oscillations shows no significant shift of the frequencies with pump energy and the peak amplitudes do not show a strong trend, when normalised to the peak $\Delta T/T$ value (Figure 6.11). However, at pump energies lower than 2.25 eV, the 150 cm^{-1} (19 meV) peak cannot be distinguished and at pump energies lower than 1.98 eV, neither peak could be resolved. Therefore, the excess energy of photoexcited carriers directly affects which modes are produced by impulsive absorption.

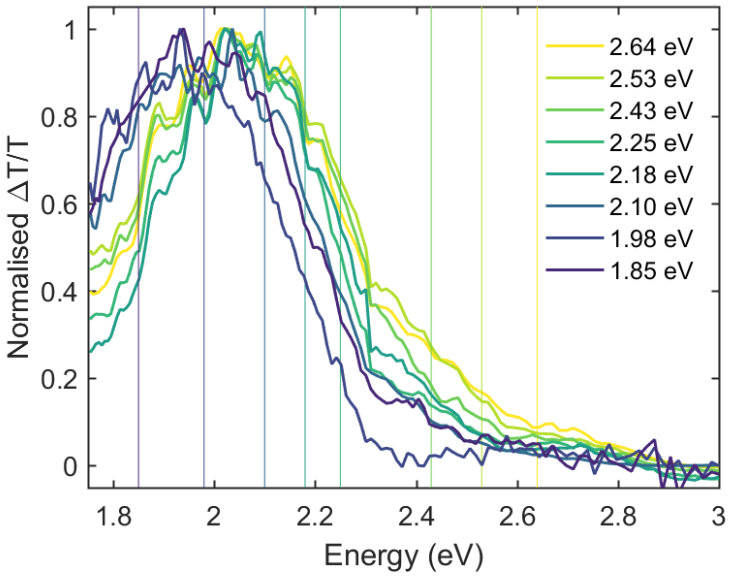

Figure 6.10 Normalised TA spectra at 5 ps delay using various excitation energies.

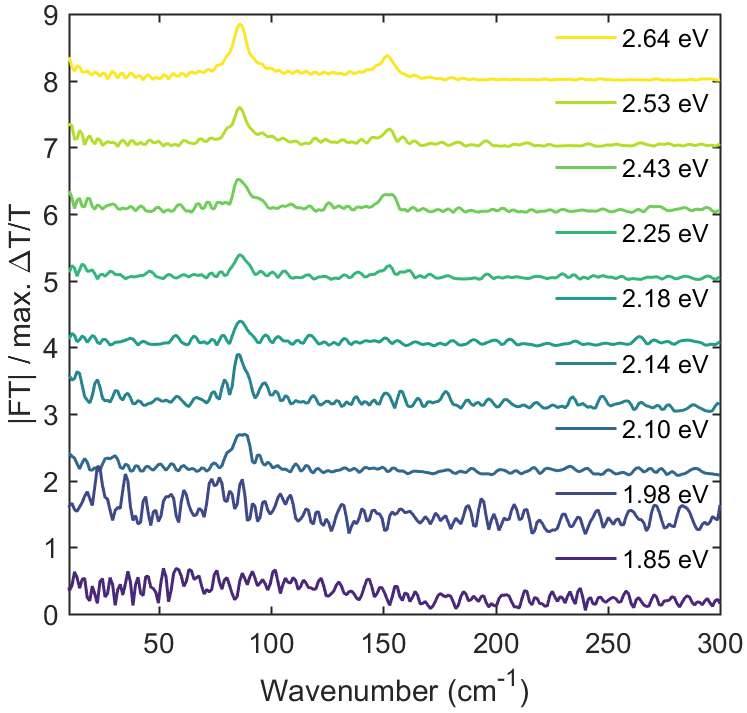

Figure 6.11 Fourier transform spectra of the oscillations at probe energy 2.08 eV. Each spectrum is normalised to the maximum value of $\Delta T/T$ for this probe energy.

6.4.2 Comparison of vibrations in $Cs_2AgBiBr_6$, BiI_3 and BiOI

The coherent vibrations observed in the TA signal at room temperature are a common feature to all the bismuth halide based compounds studied here, as well as others reported in the literature [120]. I will now briefly summarise and compare their behaviour.

The phonon modes involved are not always of the A_{1g} symmetry, with E_g modes also contributing in $Cs_2AgBiBr_6$ and BiOI. This would exclude a symmetry-breaking mechanism such as the theory of displacive excitation of coherent phonons observed in elemental bismuth [32]. Furthermore, the modes are always associated with a stretching of the Bi–X bonds (X = Br, I). It may not be surprising that such modes couple strongly to the electronic states near the band edge as, in each of these materials, these states are dominated by contributions from Bi p-orbitals and X p-orbitals. It should be noted that octahedral coordination of the bismuth and halide ions is not necessary, as observed in BiOI.

No evidence was found of phonons coupling to the ground state: sub-bandgap, high fluence pump pulses failed to produce any impulsive stimulated Raman effects in any of the materials. Instead, pump energies above resonance produced modulations of the TA signal, the amplitudes of which were directly proportional to the signal strength at that probe energy.

In BiOI it was also found that exciting carriers with an excess energy of approximately 250 meV was required to observe oscillations of the 85 cm^{-1} A_{1g} mode, correspondingly, 400 meV was needed for the 150 cm^{-1} E_g mode. This shows that the cooling process of carriers, when incoherent phonons are emitted, does not cause faster decoherence of the impulsively excited vibrations. Rather, hotter carriers may cause a greater distortion of the lattice upon excitation, allowing higher energy modes to be excited. An alternative explanation would be that the higher energy states bleached by these carriers may be more affected, i.e. change their oscillator strength more, as a result of the lattice movement. In the future, the excited carrier densities could be matched for all spectra, which would enable quantitative comparison of the amplitudes at each probe wavelength, as the band occupation should be the same after cooling.

There is more to be done to understand the various effects of this behaviour on device performance. In general, the high degree of coupling between phonons and the excited states in these materials would be expected to strengthen the screening and localisation of carriers, and therefore reduce their mobilities at increasing temperatures, which could be tested. It may also contribute to slow non-radiative recombination to deep defects, as proposed for lead-

halide perovskites [59], which may help to prolong lifetimes where this is a limiting loss mechanism.

6.5 Conclusions and further work

In summary, the excited states of BiOI thin films were shown to be intrinsically disordered, with broad PL signatures persisting down to 67 K. Together with a large Stokes shift, this showed that the PL is be either from self-trapping of excitons or radiative recombination to defects. A thermally activated quenching model was used to find the activation energy of the non-radiative recombination pathway, which was 24 meV.

A broad ground state bleach in TA is also indicative of a spread of energetic states occupied by the carriers, however, no evidence of band filling was observed in the fluence dependence. This, combined with the presence of a bleach above the pump energy for a resonant pump, indicated that carriers at the band edge can bleach multiple transitions, consistent with the predicted flatness of the bands in this material.

The excited state lifetime was found to be 47 ps, which would not allow BiOI to compete against $Cs_2AgBiBr_6$ unless this lifetime can be improved by some processing to remove or passivate defects. This would also suggest that the defect tolerance of BiOI was overestimated, likely by not considering extrinsic defects caused by common contaminants or surface states.

As for all the materials studied, coherent oscillations in the TA showed that phonon modes associated with a stretch of the Bi–I bond couple strongly to the excited state. An impulsive absorption mechanism for the generation of these phonons was inferred. Furthermore, charge carriers with different amounts of excess energy were required to generate or observe different phonon modes coherently.

Further research must be carried out to pin down the exact cause of the energetic disorder I have observed; one route is to grow single crystals or films with increasing grain size to vary the density of interfaces and look for changes in the absorption, PL linewidth and quantum efficiency. Low temperature absorption would help to verify the expected shift of the band edge as observed in our PL temperature series.

Alternatively, room temperature spectroscopy on thin films using confocal PL mapping or near-field PL microscopy could resolve spatial inhomogeneities and localised emissive sites. A PL excitation scan would also provide insight into the relaxation of the excited species. A sensitive method of ultrafast time-resolved PL would be interesting both to detect funnelling of emissive states down to lower energies over time and also to resolve the effect of the coherent phonons on the radiative transition.

However, the PL only provides limited information about states which decay non-radiatively, which is a large proportion of them. It may be more fruitful to perform temperature-dependent transport measurements to extract the phonon scattering rate of carriers. In principle, time-resolved microwave or THz conductivity could also give this information.

Additionally, as for BiI_3, the layered structure of BiOI lends itself to study as a 2D material, and methods to grow monolayers have already been developed for photocatalysis applications. Going to the nanoscale may provide more opportunities for exploiting this material, as its short charge carrier lifetime could be long enough to travel the small distances involved in a nanoscale device.

Chapter 7: Conclusions and outlook

7.1 Conclusions

In this thesis, I have characterised three different semiconductors in terms of their fundamental suitability for use as absorbers in photovoltaics. They all form part of a class of semiconductors which has been posited as a non-toxic substitute for lead-halide perovskites — in which the bismuth halide content dominates the electronic states near the band gap. A general conclusion is that these materials are fundamentally different from the lead halides, due to their indirect band gaps, low photoluminescence efficiencies, and higher band gap energies.

In Chapter 4, I determined that the charge carrier lifetime is 1.4 μs in $Cs_2AgBiBr_6$ thin films, which is longer than had been previously reported from PL lifetimes, by using transient absorption to detect the non-radiatively decaying carriers. I also found that there are sub-gap states created on the same timescale as the PL that then live as long as the overall charge carrier population. Together with the low temperature broadening and the large Stokes shift of the PL, this supports the hypothesis that radiative recombination occurs via sub-bandgap defect states rather than phonon-assisted band-to-band recombination. The main significance of these findings is to show that devices made from these films can be efficient, making them a contender for development as top cells in silicon based tandem solar cells.

Chapter 5 focused on the properties of excitons in BiI_3. The temperature dependence of the PL showed that phonons do not only increase the non-radiative recombination rate, but also decrease the radiative rate of the direct exciton. I measured an excited state lifetime of 72 ns in a single crystal at room temperature, suggesting that this material could in principle be used for PV applications. While the band gap of BiI_3 is closer to the ideal for a single junction solar cell, the large binding energy of the excitonic states and shorter lifetimes would lead to unavoidable losses in devices.

In chapter 6, I showed that the excited states of BiOI thin films are intrinsically disordered, with broad PL either from self-trapping of excitons or radiative recombination to defects. TA

spectra also showed broad signatures, with the high energy broadening being explained by a multiply degenerate ground state. The lifetime from ultrafast measurements was 47 ps, an unprecedentedly low value, which suggests that BiOI thin films are not a viable absorber for PV in their current state. If the non-radiative recombination can be reduced by the passivation of defects, there may be some hope for BiOI either as a thin film or a 2D semiconductor.

Finally, despite the differences between the compounds presented here, they have all shown strong coupling between their electronic excited states and phonons, more precisely, the phonons associated with a bismuth-halide bond stretch. These phonons have energies on the order of ~10 meV and can be generated coherently by impulsive absorption of a short, above-bandgap pulse. The net effect of this coupling for device efficiency remains to be established as it may prolong carrier lifetimes through increased screening and localisation of carriers, while potentially hindering charge transport and causing loss of energy through self-trapping.

7.2 Future work

In the field of lead-free perovskites, it is common to attempt to reproduce the research already done on the lead halides to boost efficiencies and relate fundamental discoveries back to our understanding of metal-halide perovskites in general. However, I think a more constructive approach for the bismuth halide semiconductors is first to understand their unique properties in order to more faithfully match them to applications and more effectively optimise them.

The silver-bismuth halide double perovskites are an important class of materials to develop for PV but more needs to be done to improve the reproducibility of fabrication. More understanding of the role of defects and localisation of the charge carriers would be useful, and this could be done using scanning probe imaging and spectroscopy techniques as well as using deep level transient spectroscopy. Also, exploring the compositional parameter space for more double perovskites with lower bandgaps and improved transport properties is a potentially fruitful avenue. Further applications that also exploit the high atomic number of the bismuth content, such as radiation detection, could also be investigated.

Although the same vein of work could be undertaken for BiI_3 and BiOI, I think the most interesting route would be to enter “flat land” and explore how decreased dimensionality affects their optoelectronic properties. Although mechanical exfoliation of these materials has not had the same success as for graphene and transition metal dichalcogenides, if vapour

deposition of monolayers can be optimised, this would allow spectroscopic studies of these materials in two dimensions and potential incorporation into nanoscale devices. Combined with other 2D materials into van der Waals heterostructures, this could accelerate the miniaturisation of electronics or yield new opportunities for fundamental studies of, for example, exciton-exciton interactions. While quoting Feynman is tempting here, I shall abstain from ending on a cliché and leave the possibilities of the nanoscale to the reader's imagination.

References

[1] IEA, “SDG7: Data and Projections,” 2019. https://www.iea.org/reports/sdg7-data-and-projections.

[2] UN, *World Population Prospects 2019*. 2019.

[3] IPCC *et al.*, “Global Warming of 1.5°C. An IPCC Special Report on the impacts of global warming of 1.5°C above pre-industrial levels and related global greenhouse gas emission pathways, in the context of strengthening the global response to the threat of climate change,” 2018.

[4] S. Philipps and W. Warmuth, “Photovoltaics Report 2019. Fraunhofer Institute for Solar Energy Systems, ISE with support of PSE GmbH,” no. November, 2019, [Online]. Available: https://www.ise.fraunhofer.de/content/dam/ise/de/documents/publications/studies/Photovoltaics-Report.pdf.

[5] M. Pagliaro, R. Ciriminna, and G. Palmisano, “Flexible solar cells.,” *ChemSusChem*, vol. 1, no. 11, pp. 880–891, 2008, doi: 10.1002/cssc.200800127.

[6] D. A. Neamen, *Semiconductor Physics and Devices: Basic Principles*, 4th ed. McGraw-Hill, 2012.

[7] NREL, “Best research cell efficiency chart,” 2019. https://www.nrel.gov/pv/assets/pdfs/best-research-cell-efficiencies.20191106.pdf.

[8] L. K. Ono, Y. Qi, and S. (Frank) Liu, “Progress toward Stable Lead Halide Perovskite Solar Cells,” *Joule*, vol. 2, no. 10, pp. 1961–1990, 2018, doi: 10.1016/j.joule.2018.07.007.

[9] L. C. Lee, T. N. Huq, J. L. Macmanus-Driscoll, and R. L. Z. Hoye, “Research Update: Bismuth-based perovskite-inspired photovoltaic materials,” *APL Mater.*, vol. 6, no. 8, 2018, doi: 10.1063/1.5029484.

[10] P. Y. Yu and M. Cardona, *Fundamentals of Semiconductors*, 3rd, Corre ed. Springer Berlin Heidelberg New York, 2005.

[11] N. W. Ashcroft and N. D. Mermin, *Solid State Physics*. New York: Brooks Cole/Thomson Learning, 1976.

[12] B. K. Ridley, *Quantum Processes in Semiconductors*, 5th ed. OUP, 2013.

[13] S. Lany and A. Zunger, "Assessment of correction methods for the band-gap problem and for finite-size effects in supercell defect calculations: Case studies for ZnO and GaAs," *Phys. Rev. B*, vol. 78, no. 23, p. 235104, Dec. 2008, doi: 10.1103/PhysRevB.78.235104.

[14] H. Peng, D. O. Scanlon, V. Stevanovic, J. Vidal, G. W. Watson, and S. Lany, "Convergence of density and hybrid functional defect calculations for compound semiconductors," *Phys. Rev. B*, vol. 88, no. 11, p. 115201, Sep. 2013, doi: 10.1103/PhysRevB.88.115201.

[15] M. Fox, *Optical Properties of Solids*, 3rd ed. Oxford: Oxford UP, 2006.

[16] J. Nelson, *The Physics of Solar Cells*. London: Imperial College, 2003, 2003.

[17] T. S. Moss, "The Interpretation of the Properties of Indium Antimonide," *Proc. Phys. Soc. Sect. B*, vol. 67, no. 10, pp. 775–782, Oct. 1954, doi: 10.1088/0370-1301/67/10/306.

[18] M. B. Price *et al.*, "Hot-carrier cooling and photoinduced refractive index changes in organic–inorganic lead halide perovskites," *Nat. Commun.*, vol. 6, no. May, p. 8420, 2015, doi: 10.1038/ncomms9420.

[19] G. D. Cody, "Urbach edge of crystalline and amorphous silicon: a personal review," *Journal of Non-Crystalline Solids*, vol. 141, no. C. pp. 3–15, Jan. 1992, doi: 10.1016/S0022-3093(05)80513-7.

[20] C. W. Greeff and H. R. Glyde, "Anomalous Urbach tail in GaAs," *Phys. Rev. B*, vol. 51, no. 3, pp. 1778–1783, Jan. 1995, doi: 10.1103/PhysRevB.51.1778.

[21] W. Y. Liang, "Excitons," *Phys. Educ.*, vol. 5, no. 4, pp. 226–228, Jul. 1970, doi: 10.1088/0031-9120/5/4/003.

[22] G. Tränkle, H. Leier, A. Forchel, H. Haug, C. Ell, and G. Weimann, "Dimensionality dependence of the band-gap renormalization in two- and three-dimensional electron-hole plasmas in GaAs," *Phys. Rev. Lett.*, vol. 58, no. 4, pp. 419–422, Jan. 1987, doi:

10.1103/PhysRevLett.58.419.

[23] P. E. Schmid, “Optical absorption in heavily doped silicon,” *Phys. Rev. B*, vol. 23, no. 10, pp. 5531–5536, May 1981, doi: 10.1103/PhysRevB.23.5531.

[24] J. Shah, *Ultrafast Spectroscopy of Semiconductors and Semiconductor Nanostructures*, 2nd ed., vol. 115. Berlin, Heidelberg: Springer Berlin Heidelberg, 1999.

[25] I. G. Austin and N. F. Mott, “Polarons in crystalline and non-crystalline materials,” *Adv. Phys.*, vol. 18, no. 71, pp. 41–102, Jan. 1969, doi: 10.1080/00018736900101267.

[26] R. T. Williams and K. S. Song, “The self-trapped exciton,” *J. Phys. Chem. Solids*, vol. 51, no. 7, pp. 679–716, 1990, doi: 10.1016/0022-3697(90)90144-5.

[27] M. D. Smith, A. Jaffe, E. R. Dohner, A. M. Lindenberg, and H. I. Karunadasa, “Structural origins of broadband emission from layered Pb-Br hybrid perovskites,” *Chem. Sci.*, vol. 8, no. 6, pp. 4497–4504, 2017, doi: 10.1039/c7sc01590a.

[28] K. M. McCall, C. C. Stoumpos, S. S. Kostina, M. G. Kanatzidis, and B. W. Wessels, “Strong Electron–Phonon Coupling and Self-Trapped Excitons in the Defect Halide Perovskites $A_3M_2I_9$ (A = Cs, Rb; M = Bi, Sb),” *Chem. Mater.*, vol. 9, p. acs.chemmater.7b01184, 2017, doi: 10.1021/acs.chemmater.7b01184.

[29] L. Dhar, J. A. Rogers, and K. A. Nelson, “Time-resolved vibrational spectroscopy in the impulsive limit,” *Chem. Rev.*, vol. 94, no. 1, pp. 157–193, Jan. 1994, doi: 10.1021/cr00025a006.

[30] M. Liebel, C. Schnedermann, T. Wende, and P. Kukura, “Principles and Applications of Broadband Impulsive Vibrational Spectroscopy,” *J. Phys. Chem. A*, vol. 119, no. 36, pp. 9506–9517, 2015, doi: 10.1021/acs.jpca.5b05948.

[31] F. Thouin *et al.*, “Phonon coherences reveal the polaronic character of excitons in two-dimensional lead-halide perovskites,” 2019, doi: 10.1038/s41563-018-0262-7.

[32] H. J. Zeiger, J. Vidal, T. K. Cheng, E. P. Ippen, G. Dresselhaus, and M. S. Dresselhaus, “Theory for displacive excitation of coherent phonons,” *Phys. Rev. B*, vol. 45, no. 2, pp. 768–778, Jan. 1992, doi: 10.1103/PhysRevB.45.768.

[33] L. Dhar, J. A. Rogers, K. A. Nelson, and V. I. I. Acknowledgments, “Time-Resolved Vibrational Spectroscopy in the Impulsive Limit,” pp. 157–193, 1994, doi:

10.1021/cr00025a006.

[34] B. Di Bartolo and C. Beckwith, Eds., *Optical Properties of Excited States in Solids*, vol. 301. Boston, MA: Springer US, 1992.

[35] W. Shockley and W. T. Read, "Statistics of the Recombination of Holes and Electrons," *Phys. Rev.*, vol. 87, no. 46, pp. 835–842, 1952, doi: dx.doi.org/10.1103/PhysRev.87.835.

[36] C. J. Foot, *Atomic Physics*. Oxford University Press, 2005.

[37] C. H. Wallace, Ed., *Organic Solar Cells*. London: Springer-Verlag, 2013.

[38] A. R. Beattie and P. T. Landsberg, "Auger effect in semiconductors," *Proc. R. Soc.*, vol. 249, no. 1256, pp. 16–29, 1958, doi: 10.1098/rspa.1959.0003.

[39] C. Wehrenfennig, G. E. Eperon, M. B. Johnston, H. J. Snaith, and L. M. Herz, "High Charge Carrier Mobilities and Lifetimes in Organolead Trihalide Perovskites," pp. 1584–1589, 2014, doi: 10.1002/adma.201305172.

[40] D. M. Chapin, C. S. Fuller, and G. L. Pearson, "A New Silicon p-n Junction Photocell for Converting Solar Radiation into Electrical Power," *J. Appl. Phys.*, vol. 25, no. 5, pp. 676–677, May 1954, doi: 10.1063/1.1721711.

[41] P. K. Nayak, S. Mahesh, H. J. Snaith, and D. Cahen, "Photovoltaic solar cell technologies: analysing the state of the art," *Nat. Rev. Mater.*, vol. 4, no. 4, pp. 269–285, 2019, doi: 10.1038/s41578-019-0097-0.

[42] K. K. Ng and S. M. Sze, *Physics of Semiconductor Devices*, 3rd ed. John Wiley & Sons, Inc., 2007.

[43] G. P. Willeke and E. R. Weber, *Advances in Photovoltaics, Part 2*. Elsevier, 2013.

[44] A. J. Nozik, B. Matthew C, and G. Conibeer, *Advanced Concepts in Photovoltaics*. Cambridge: Royal Society of Chemistry, 2014.

[45] W. Shockley and H. J. Queisser, "Detailed Balance Limit of Efficiency of p-n Junction Solar Cells," *J. Appl. Phys.*, vol. 32, no. 3, pp. 510–519, Mar. 1961, doi: 10.1063/1.1736034.

[46] M. A. Green, *Third Generation Photovoltaics*. 2006.

[47] A. De Vos, “Detailed balance limit of the efficiency of tandem solar cells,” *J. Phys. D. Appl. Phys.*, vol. 13, no. 5, pp. 839–846, 1980, doi: 10.1088/0022-3727/13/5/018.

[48] H. Zhang *et al.*, “Over 14% Efficiency in Organic Solar Cells Enabled by Chlorinated Nonfullerene Small-Molecule Acceptors,” *Adv. Mater.*, vol. 30, no. 28, p. 1800613, Jul. 2018, doi: 10.1002/adma.201800613.

[49] D. B. Mitzi, “Synthesis, Structure, and Properties of Organic-Inorganic Perovskites and Related Materials,” 2007, pp. 1–121.

[50] K. Momma and F. Izumi, “VESTA 3 for three-dimensional visualization of crystal, volumetric and morphology data.” J. Appl. Crystallogr., 44, pp. 1272–1276, 2011.

[51] D. Weber, “CH 3 NH 3 PbX 3 , ein Pb(II)-System mit kubischer Perowskitstruktur,” *Z. Naturforsch., B J. Chem. Sci.*, vol. 1445, no. August, pp. 1443–1445, 1978.

[52] M. A. Green, A. Ho-Baillie, and H. J. Snaith, “The emergence of perovskite solar cells,” *Nat. Photonics*, vol. 8, no. 7, pp. 506–514, 2014, doi: 10.1038/nphoton.2014.134.

[53] W. S. Yang *et al.*, “High-performance photovoltaic perovskite layers fabricated through intramolecular exchange,” *Science (80-.).*, vol. 348, no. 6240, pp. 1234–1237, 2015, doi: 10.1126/science.aaa9272.

[54] W. Li, Z. Wang, F. Deschler, S. Gao, R. H. Friend, and A. K. Cheetham, “Chemically diverse and multifunctional hybrid organic-inorganic perovskites,” *Nat. Rev. Mater.*, vol. 2, no. 3, 2017, doi: 10.1038/natrevmats.2016.99.

[55] L. M. Pazos-Outón, T. P. Xiao, and E. Yablonovitch, “Fundamental Efficiency Limit of Lead Iodide Perovskite Solar Cells,” *J. Phys. Chem. Lett.*, vol. 9, no. 7, pp. 1703–1711, 2018, doi: 10.1021/acs.jpclett.7b03054.

[56] J. Li *et al.*, “Biological impact of lead from halide perovskites reveals the risk of introducing a safe threshold,” *Nat. Commun.*, vol. 11, no. 1, pp. 1–5, 2020, doi: 10.1038/s41467-019-13910-y.

[57] L. M. Pazos-Outon *et al.*, “Photon recycling in lead iodide perovskite solar cells,” *Science (80-.).*, vol. 351, no. 6280, pp. 1430–1433, 2016, doi: 10.1126/science.aaf1168.

[58] H. Jin *et al.*, “It’s a trap! On the nature of localised states and charge trapping in lead halide perovskites,” *Mater. Horizons*, vol. 7, no. 2, pp. 397–410, 2020, doi: 10.1039/C9MH00500E.

[59] T. Kirchartz, T. Markvart, U. Rau, and D. A. Egger, “Impact of Small Phonon Energies on the Charge-Carrier Lifetimes in Metal-Halide Perovskites,” *J. Phys. Chem. Lett.*, vol. 9, no. 5, pp. 939–946, 2018, doi: 10.1021/acs.jpclett.7b03414.

[60] E. Cinquanta *et al.*, “Ultrafast THz Probe of Photoinduced Polarons in Lead-Halide Perovskites,” *Phys. Rev. Lett.*, vol. 122, no. 16, p. 166601, 2019, doi: 10.1103/PhysRevLett.122.166601.

[61] I. B. Koutselas, L. Ducasse, and G. C. Papavassiliou, “Electronic properties of three- and low-dimensional semiconducting materials with Pb halide and Sn halide units,” *J. Phys. Condens. Matter*, vol. 8, no. 9, pp. 1217–1227, Feb. 1996, doi: 10.1088/0953-8984/8/9/012.

[62] N. K. Noel *et al.*, “Lead-free organic-inorganic tin halide perovskites for photovoltaic applications,” *Energy Environ. Sci.*, vol. 7, no. 9, pp. 3061–3068, 2014, doi: 10.1039/c4ee01076k.

[63] W. F. Yang, F. Igbari, Y. H. Lou, Z. K. Wang, and L. S. Liao, “Tin Halide Perovskites: Progress and Challenges,” *Adv. Energy Mater.*, vol. 1902584, pp. 1–30, 2019, doi: 10.1002/aenm.201902584.

[64] Z. Zhang *et al.*, “High-Quality (CH 3 NH 3) 3 Bi 2 I 9 Film-Based Solar Cells: Pushing Efficiency up to 1.64%,” *J. Phys. Chem. Lett.*, vol. 8, no. 17, pp. 4300–4307, Sep. 2017, doi: 10.1021/acs.jpclett.7b01952.

[65] R. L. Z. Hoye *et al.*, “Methylammonium Bismuth Iodide as a Lead-Free, Stable Hybrid Organic-Inorganic Solar Absorber,” *Chem. - A Eur. J.*, vol. 22, no. 8, pp. 2605–2610, 2016, doi: 10.1002/chem.201505055.

[66] Z. Xiao, W. Meng, J. Wang, D. B. Mitzi, and Y. Yan, “Searching for Promising New Perovskite-Based Photovoltaic Absorbers: The Importance of Electronic Dimensionality,” *Mater. Horiz.*, vol. 4, no. 2, pp. 206–216, 2016, doi: 10.1039/C6MH00519E.

[67] W. Meng, X. Wang, Z. Xiao, J. Wang, D. B. Mitzi, and Y. Yan, “Parity-Forbidden

Transitions and Their Impact on the Optical Absorption Properties of Lead-Free Metal Halide Perovskites and Double Perovskites," *J. Phys. Chem. Lett.*, vol. 8, no. 13, pp. 2999–3007, 2017, doi: 10.1021/acs.jpclett.7b01042.

[68] F. Wei *et al.*, "Synthesis and Properties of a Lead-Free Hybrid Double Perovskite: (CH3NH3)2AgBiBr6," *Chem. Mater.*, vol. 29, no. 3, pp. 1089–1094, 2017, doi: 10.1021/acs.chemmater.6b03944.

[69] A. H. Slavney, T. Hu, A. M. Lindenberg, and H. I. Karunadasa, "A Bismuth-Halide Double Perovskite with Long Carrier Recombination Lifetime for Photovoltaic Applications," vol. 3, pp. 3–6, 2016, doi: 10.1021/jacs.5b13294.

[70] E. T. McClure, M. R. Ball, W. Windl, and P. M. Woodward, "Cs2AgBiX6(X = Br, Cl): New Visible Light Absorbing, Lead-Free Halide Perovskite Semiconductors," *Chem. Mater.*, vol. 28, no. 5, pp. 1348–1354, 2016, doi: 10.1021/acs.chemmater.5b04231.

[71] E. Greul, M. L. Petrus, A. Binek, P. Docampo, and T. Bein, "Highly stable, phase pure Cs 2 AgBiBr 6 double perovskite thin films for optoelectronic applications," *J. Mater. Chem. A*, vol. 5, no. 37, pp. 19972–19981, 2017, doi: 10.1039/C7TA06816F.

[72] N. J. Podraza *et al.*, "Band gap and structure of single crystal BiI3: Resolving discrepancies in literature," *J. Appl. Phys.*, vol. 114, no. 3, 2013, doi: 10.1063/1.4813486.

[73] R. E. Brandt *et al.*, "Investigation of Bismuth Triiodide (BiI3) for Photovoltaic Applications," *J. Phys. Chem. Lett.*, vol. 6, no. 21, pp. 4297–4302, 2015, doi: 10.1021/acs.jpclett.5b02022.

[74] U. H. Hamdeh, R. D. Nelson, B. J. Ryan, U. Bhattacharjee, J. W. Petrich, and M. G. Panthani, "Solution-processed BiI3 thin films for photovoltaic applications: Improved carrier collection via solvent annealing," *Chem. Mater.*, vol. 28, no. 18, pp. 6567–6574, 2016, doi: 10.1021/acs.chemmater.6b02347.

[75] Y. N. Dmitriyev, P. R. Bennett, L. J. Cirignano, M. B. Klugerman, and K. S. Shah, "Bismuth iodide crystals as a detector material: some optical and electrical properties," *Hard X-Ray, Gamma-Ray, Neutron Detect. Phys.*, vol. 3768, no. October 1999, p. 521, 1999, doi: 10.1117/12.366625.

[76] A. M. Ganose, M. Cuff, K. T. Butler, A. Walsh, and D. O. Scanlon, “Interplay of Orbital and Relativistic Effects in Bismuth Oxyhalides: BiOF, BiOCl, BiOBr, and BiOI,” *Chem. Mater.*, vol. 28, no. 7, pp. 1980–1984, 2016, doi: 10.1021/acs.chemmater.6b00349.

[77] A. M. Ganose, C. N. Savory, and D. O. Scanlon, “Beyond methylammonium lead iodide: prospects for the emergent field of ns2 containing solar absorbers,” *Chem. Commun.*, vol. 53, no. 1, pp. 20–44, 2017, doi: 10.1039/c6cc06475b.

[78] R. L. Z. Hoye *et al.*, “Strongly Enhanced Photovoltaic Performance and Defect Physics of Air-Stable Bismuth Oxyiodide (BiOI),” *Adv. Mater.*, vol. 29, no. 36, p. 1702176, Sep. 2017, doi: 10.1002/adma.201702176.

[79] P. Kubelka and F. Munk, “An Article on Optics of Paint Layers,” *Z. Tech. Phys.*, vol. 593, no. 12, 1931.

[80] H. G. Hecht, “The interpretation of diffuse reflectance spectra,” *J. Res. Natl. Bur. Stand. Sect. A Phys. Chem.*, vol. 80A, no. 4, p. 567, Jul. 1976, doi: 10.6028/jres.080A.056.

[81] “iStar CCD series Intensified CCDs for Time-resolved Spectroscopy,” *Andor Oxford Instruments*, p. 11, 2015, [Online]. Available: https://andor.oxinst.com/products/intensified-camera-series.

[82] J. C. de Mello, H. F. Wittmannn, and R. H. Friend, “An Improved Experimental Determination of External Photoluminescence Quantum Efficiency**,” *Adv. Mater.*, vol. 9, no. 3, p. 230, 1997, doi: 10.1002/adma.200903328.

[83] G. Cerullo and S. De Silvestri, “Ultrafast optical parametric amplifiers,” *Rev. Sci. Instrum.*, vol. 74, no. 1, pp. 1–18, Jan. 2003, doi: 10.1063/1.1523642.

[84] C. Manzoni and G. Cerullo, “Design criteria for ultrafast optical parametric amplifiers,” *J. Opt.*, vol. 18, no. 10, pp. 1–33, 2016, doi: 10.1088/2040-8978/18/10/103501.

[85] H. E. Lessing and A. Von Jena, “Separation of rotational diffusion and level kinetics in transient absorption spectroscopy,” *Chem. Phys. Lett.*, vol. 42, no. 2, pp. 213–217, Sep. 1976, doi: 10.1016/0009-2614(76)80349-1.

[86] R. L. Z. Hoye *et al.*, “Perovskite-Inspired Photovoltaic Materials: Toward Best

Practices in Materials Characterization and Calculations," *Chem. Mater.*, vol. 29, no. 5, pp. 1964–1988, 2017, doi: 10.1021/acs.chemmater.6b03852.

[87] D. Shi *et al.*, "Low trap-state density and long carrier diffusion in organolead trihalide perovskite single crystals," vol. 347, no. 6221, 2015.

[88] C. Wehrenfennig, G. E. Eperon, M. B. Johnston, H. J. Snaith, and L. M. Herz, "High charge carrier mobilities and lifetimes in organolead trihalide perovskites," *Adv. Mater.*, vol. 26, no. 10, pp. 1584–1589, 2014, doi: 10.1002/adma.201305172.

[89] S. De Wolf *et al.*, "Organometallic halide perovskites: Sharp optical absorption edge and its relation to photovoltaic performance," *J. Phys. Chem. Lett.*, vol. 5, no. 6, pp. 1035–1039, 2014, doi: 10.1021/jz500279b.

[90] J. M. Richter *et al.*, "Enhancing photoluminescence yields in lead halide perovskites by photon recycling and light out-coupling," *Nat. Commun.*, vol. 7, 2016, doi: 10.1038/ncomms13941.

[91] K. Lin *et al.*, "Perovskite light-emitting diodes with external quantum efficiency exceeding 20 per cent," *Nature*, vol. 562, no. 7726, pp. 245–248, 2018, doi: 10.1038/s41586-018-0575-3.

[92] C. N. Savory, A. Walsh, and D. O. Scanlon, "Can Pb-Free Halide Double Perovskites Support High-Efficiency Solar Cells?," *ACS Energy Lett.*, vol. 1, no. 5, pp. 949–955, 2016, doi: 10.1021/acsenergylett.6b00471.

[93] K. Z. Du, W. Meng, X. Wang, Y. Yan, and D. B. Mitzi, "Bandgap Engineering of Lead-Free Double Perovskite Cs2AgBiBr6 through Trivalent Metal Alloying," *Angew. Chemie - Int. Ed.*, vol. 56, no. 28, pp. 8158–8162, 2017, doi: 10.1002/anie.201703970.

[94] R. Jaramillo *et al.*, "Transient terahertz photoconductivity measurements of minority-carrier lifetime in tin sulfide thin films: Advanced metrology for an early stage photovoltaic material," *J. Appl. Phys.*, vol. 119, no. 3, 2016, doi: 10.1063/1.4940157.

[95] R. E. Brandt *et al.*, "Searching for 'defect-Tolerant' Photovoltaic Materials: Combined Theoretical and Experimental Screening," *Chem. Mater.*, vol. 29, no. 11, pp. 4667–4674, 2017, doi: 10.1021/acs.chemmater.6b05496.

[96] G. Volonakis *et al.*, "Lead-Free Halide Double Perovskites via Heterovalent Substitution of Noble Metals," *J. Phys. Chem. Lett.*, vol. 7, no. 7, pp. 1254–1259,

2016, doi: 10.1021/acs.jpclett.6b00376.

[97] W. Pan *et al.*, “Cs2AgBiBr6 single-crystal X-ray detectors with a low detection limit,” *Nat. Photonics*, vol. 11, no. 11, pp. 726–732, Nov. 2017, doi: 10.1038/s41566-017-0012-4.

[98] D. Bartesaghi *et al.*, “Charge Carrier Dynamics in Cs2AgBiBr6Double Perovskite,” *J. Phys. Chem. C*, vol. 122, no. 9, pp. 4809–4816, 2018, doi: 10.1021/acs.jpcc.8b00572.

[99] J. Lim *et al.*, “Elucidating the long-range charge carrier mobility in metal halide perovskite thin films † Broader context,” *Energy Environ. Sci*, vol. 12, p. 169, 2019, doi: 10.1039/c8ee03395a.

[100] J. Tauc, “Optical properties and electronic structure of amorphous Ge and Si,” *Mater. Res. Bull.*, vol. 3, no. 1, pp. 37–46, Jan. 1968, doi: 10.1016/0025-5408(68)90023-8.

[101] Z. Xiao, W. Meng, J. Wang, and Y. Yan, “Thermodynamic Stability and Defect Chemistry of Bismuth-Based Lead-Free Double Perovskites,” *ChemSusChem*, vol. 9, no. 18, pp. 2628–2633, 2016, doi: 10.1002/cssc.201600771.

[102] M. R. Filip, S. Hillman, A. A. Haghighirad, H. J. Snaith, and F. Giustino, “Band Gaps of the Lead-Free Halide Double Perovskites Cs2BiAgCl6 and Cs2BiAgBr6 from Theory and Experiment,” *J. Phys. Chem. Lett.*, vol. 7, no. 13, pp. 2579–2585, 2016, doi: 10.1021/acs.jpclett.6b01041.

[103] J. A. Steele *et al.*, “Giant Electron–Phonon Coupling and Deep Conduction Band Resonance in Metal Halide Double Perovskite,” *ACS Nano*, p. acsnano.8b02936, 2018, doi: 10.1021/acsnano.8b02936.

[104] L. Schade *et al.*, “Structural and optical properties of Cs2AgBiBr6 Double Perovskite,” *ACS Energy Lett.*, p. (in review), 2019, doi: 10.1021/acsenergylett.8b02090.

[105] A. T. Lintereur, W. Qiu, J. C. Nino, and J. Baciak, “Characterization of bismuth tri-iodide single crystals for wide band-gap semiconductor radiation detectors,” *Nucl. Instruments Methods Phys. Res. Sect. A Accel. Spectrometers, Detect. Assoc. Equip.*, vol. 652, no. 1, pp. 166–169, 2011, doi: 10.1016/j.nima.2010.12.013.

[106] S. Ma *et al.*, “Vertically Oriented BiI3 Template Featured BiI3/Polymer Heterojunction for High Photocurrent and Long-Term Stable Solar Cells,” *ACS Appl.*

Mater. Interfaces, vol. 11, no. 35, pp. 32509–32516, 2019, doi: 10.1021/acsami.9b10266.

[107] S. B. Cho, J. Gazquez, X. Huang, Y. Myung, P. Banerjee, and R. Mishra, "Intrinsic point defects and intergrowths in layered bismuth triiodide," *Phys. Rev. Mater.*, vol. 2, no. 6, p. 064602, Jun. 2018, doi: 10.1103/PhysRevMaterials.2.064602.

[108] G. E. Jellison Jr., J. O. Ramey, and L. A. Boatner, "Optical functions of BiI3 as measured by generalized ellipsometry," *Phys. Rev. B - Condens. Matter Mater. Phys.*, vol. 59, no. 15, pp. 9718–9721, 1999.

[109] Y. Kaifu, "Excitons in layered BiI3 single crystals," *J. Lumin.*, vol. 42, no. 2, pp. 61–81, Aug. 1988, doi: 10.1016/0022-2313(88)90045-2.

[110] M. Scholz, K. Oum, and T. Lenzer, "Pronounced exciton and coherent phonon dynamics in BiI3," *Phys. Chem. Chem. Phys.*, vol. 20, no. 16, pp. 10677–10685, 2018, doi: 10.1039/c7cp07729g.

[111] Y. Petroff, P. Y. Yu, and Y. R. Shen, "Absorption, Photoluminescence, and Resonant Raman Scattering in Bil3," *Phys. Status Solidi*, vol. 61, no. 2, pp. 419–427, 1974, doi: 10.1002/pssb.2220610206.

[112] R. Merlin, "Generating coherent THz phonons with light pulses," *Solid State Commun.*, vol. 102, no. 2–3, pp. 207–220, Apr. 1997, doi: 10.1016/S0038-1098(96)00721-1.

[113] H. AN, Y. DU, T. WANG, C. WANG, W. HAO, and J. ZHANG, "Photocatalytic properties of BiOX (X = Cl, Br, and I)," *Rare Met.*, vol. 27, no. 3, pp. 243–250, Jun. 2008, doi: 10.1016/S1001-0521(08)60123-0.

[114] D. S. Bhachu *et al.*, "Bismuth oxyhalides: synthesis, structure and photoelectrochemical activity," *Chem. Sci.*, vol. 7, no. 8, pp. 4832–4841, 2016, doi: 10.1039/C6SC00389C.

[115] B. Auer, G.; Griebler, W.; Jahn, *Industrial Inorganic Pigments*. 2008.

[116] C. R. Michel, N. L. L. Contreras, and A. H. Martínez-Preciado, "Gas sensing properties of nanostructured bismuth oxychloride," *Sensors Actuators, B Chem.*, 2011, doi: 10.1016/j.snb.2011.07.047.

[117] Y. Mi, M. Zhou, L. Wen, H. Zhao, and Y. Lei, “A highly efficient visible-light driven photocatalyst: Two dimensional square-like bismuth oxyiodine nanosheets,” *Dalt. Trans.*, vol. 43, no. 25, pp. 9549–9556, 2014, doi: 10.1039/c4dt00798k.

[118] M. E. Kazyrevich *et al.*, “Crystal stacking: A route to control photoelectrochemical behavior of BiOBr films,” *Electrochim. Acta*, vol. 290, pp. 63–71, Nov. 2018, doi: 10.1016/j.electacta.2018.09.019.

[119] J. E. D. Davies, “Solid state vibrational spectroscopy-III[1] The infrared and raman spectra of the bismuth(III) oxide halides,” *J. Inorg. Nucl. Chem.*, vol. 35, no. 5, pp. 1531–1534, May 1973, doi: 10.1016/0022-1902(73)80242-8.

[120] M. Scholz, M. Morgenroth, K. Oum, and T. Lenzer, “Exciton and Coherent Phonon Dynamics in the Metal-Deficient Defect Perovskite (CH3NH3)3Sb2I9,” *J. Phys. Chem. C*, vol. 122, no. 11, pp. 5854–5863, 2018, doi: 10.1021/acs.jpcc.7b09609.